Doctoral School

PhD program in Molecular Medicine

XXXV cycle

# Syngeneic Mouse Models of Gastric Cancer with Microsatellite Instability

A dissertation submitted by

Daniela Conticelli

Supervised by

Professor Silvia Giordano

2023

*This thesis is dedicated to my mum,*

*who loves and supports me*

*and from whom I inherited all my stubbornness and perseverance.*

**TABLE OF CONTENTS**

**ABSTRACT**

Gastric cancer (GC) ranks among the most prevalent and lethal malignancies globally, accounting for over one million new cases and 700,000 deaths annually. Over the last decade, two independent molecular classifications have reported the existence of a GC subgroup characterized by microsatellite instability (MSI), including around 22-23% of GC cases. MSI is a hypermutability condition caused by the impairment of the DNA mismatch repair (MMR) system. In sporadic cancer, MMR deficiency usually occurs either by hypermethylation of the *MLH1* promoter or by loss-of-function mutations in the main MMR genes (such as *MLH1, MSH2, MSH6, PMS2*).

MSI has been described across multiple malignancies, most commonly in gynaecologic and gastrointestinal (GI) cancers. In several cases, MSI detection has become crucial for prognosis, surveillance, and therapeutic decisions. The clinical relevance of the MSI status is mostly due to its role as a strong predictor of response to immunotherapy. Nevertheless, some GI MSI tumours are refractory to immunotherapeutic regimens, probably due to both intrinsic and acquired resistance mechanisms.

GC inter and intra-tumoral heterogeneity represents a significant challenge for precise patient stratification and treatment. MSI status in GC has been associated with a good prognosis. However, some reports have indicated the existence of a subpopulation of MSI GC patients displaying a worse outcome. Furthermore, while clinical trials testing ICIs in GC have shown effectiveness in MSI patients across all treatment lines, the outcomes were not as remarkable as those observed in other cancer types. From the analysis of MSI GC patients enrolled in phase II and III clinical trials testing anti-PD1 monotherapy, it emerged that nearly half of the tumours are intrinsically resistant and complete and long-lasting responses are achieved in very few cases.

The main goal of my PhD project was the generation of syngeneic GC MSI models mimicking the key known features of MSI tumours and potentially useful for better understanding the molecular complexity and predicting the clinical behaviour of this cancer subgroup.

We successfully generated MMR-deficient (MMRd) gastric organoid cultures, inactivating either *Mlh1* or *Msh2* genes in non-transformed BALB/c mouse gastric epithelial cells through CRISPR/Cas9-based gene editing. MMRd models, but not WT controls, exhibited microsatellite instability and increased their mutation rate over time. Notably, when cultured in more stringent culture conditions, only the MMRd cells could generate tumour masses upon subcutaneous injection in immunodeficient NOD SCID mice. Following the optimisation of the gene editing protocol, we also generated clonal models without a persistent Cas9 expression, making them suitable for injection into immunocompetent BALB/c mice.

The MSI GC mouse models we developed represent a valuable resource as they could enable the comprehensive investigation of tumour development, progression and responses to immunotherapy in the presence of a fully active immune system.

## MAIN ABBREVIATIONS

GC: gastric cancer

GEA: Gastro-Esophageal Annotated platform

ICI: immune checkpoint inhibitor

KO: knockout

MLH1/Mlh1: MutL homolog 1

MMR: DNA mismatch repair

MMRd: MMR-deficient

MSH2/Msh2: MutS homolog 2

MSH3/Msh3: MutS homolog 3

MSH6/Msh6: MutS homolog 6

MSI: microsatellite instability

MSS: microsatellite stability/microsatellite stable

PD-1: programmed cell death-1

PD-L1: programmed cell death-ligand 1

PMS2/Pms2: Postmeiotic Segregation Increased 2

TCGA: The Cancer Genome Atlas

TMB: tumour mutational burden

WRN: Werner RECQL helicase

WT: wildtype

**INTRODUCTION**

**Epidemiology of Gastric Cancer.**

Gastric cancer (GC) represents a major health problem. According to GLOBOCAN estimates, there were over one million new cases (5.6% of all cancer diagnoses) and 769,000 deaths in 2020 (7.7% of all deaths from cancer), thus ranking GC as the fifth malignancy for incidence and fourth for mortality globally. GC burden varies concerning geographical distribution and sex. The highest GC incidence rates are registered in Eastern Asia, Eastern Europe and Central and South America, whereas Australia and New Zealand, Northern America and Northern Europe as well as all African regions are low-risk areas (1). In all countries, GC incidence rates increase with age and most patients are diagnosed between 55 and 80 years. Men are two-fold more susceptible than women and GC is the first leading cause of cancer-related death in the male population in several South-Central Asian countries, including Iran, Afghanistan, Turkmenistan, and Kyrgyzstan (1,2).

Gastric cancer is a complex disease with multiple risk factors. Certain inherited genetic alterations can increase GC risk. Mutations in *CDH1* and *CTNNA1* have been associated with hereditary diffuse gastric cancer (3,4), while patients with syndromes like Li-Fraumeni, Lynch and Peutz-Jeghers display an increased risk of developing various malignancies, including gastric cancer (5,6). Moreover, *BRCA1* and *BRCA2* germline mutations, well-known for their association with breast and ovarian cancers, have been also correlated with GC susceptibility (7).

Despite these genetic predispositions, the geographic variability in GC incidence and mortality is mainly explained by environmental factors. Persistent *Helicobacter pylori* infection is considered the main risk factor for non-cardia GC and the occurrence of the infection aligns

with GC incidence when viewed geographically (8,9). Beyond *H. pylori*, established risk factors for non-cardia gastric cancer include tobacco smoking and dietary factors, such as alcohol consumption, insufficient intake of fruits and vegetables and high intake of salt-preserved foods and smoked meats. Cardia GC has a different aetiology, generally not associated with *H. pylori* infection; excess body weight and chronic acid reflux are listed among the prominent cardia GC risk factors, thus mirroring the physiopathogenesis of oesophageal cancer (1).

**Current Gastric Cancer Treatment.**

Gastric cancer prognosis and standard of care vary depending on the stage at diagnosis. Despite the high incidence, most patients are diagnosed at advanced stages, due to subtle symptoms in early disease and lack of systematic screening programs in most countries (10).

Localized GC (stage 0/I) is endowed with a relatively good prognosis, with a 5-year survival rate of over 70%, while locally advanced (stage II/III) and metastatic (stage IV) cases are characterized by a poor outcome (7-35% 5-year survival) (11,12).

Surgical resection remains the most effective treatment for resectable GC. However, perioperative chemotherapy has become the standard of care for localized GC as it improves patients' outcome compared to surgery alone (13). Recently, the FLOT regimen (5-fluorouracil, leucovorin, oxaliplatin, and docetaxel) has become the new standard perioperative treatment as the FLOT4 phase II/III clinical trial suggested that it improves overall survival rates (50 months versus 35 months) in comparison with the previous standard ECF/ECX (epirubicin, cisplatin, and 5-fluorouracil/capecitabine) regimen (14,15).

Adjuvant chemotherapy is recommended for stage II/III patients undergoing primary surgery. Phase III trials demonstrated the efficacy of several cytotoxic regimens, including S-1

monotherapy (a biochemical modulation of 5-fluorouracil), CAPOX (capecitabine and oxaliplatin), SOX (S-1 and oxaliplatin), and DS (docetaxel and S-1) (16–18). The selection of the adjuvant treatment depends on the stage and the patient's performance status. S-1 monotherapy is usually chosen for stage II disease or in case of suboptimal performance status, while combination therapies are favoured in case of stage III disease (10).

Chemotherapy is still the standard of care for unresectable and metastatic GC. The backbone of first-line treatment is usually the combination of a fluoropyrimidine (5-fluorouracil, capecitabine or S-1) with a platinum, while paclitaxel, docetaxel, and irinotecan are generally administered in the second line (10).

Although chemotherapy remains a cornerstone in GC treatment, recent years have witnessed substantial advancements in alternative systemic approaches, including targeted therapies and immunotherapy, leading to an improvement in survival rates.

Molecular targeted therapies are vital treatment options for patients with advanced GC. Targeted therapies, including anti-HER2, anti-angiogenetic, and other biomarker-directed therapies, have exhibited promising efficacy in GC treatment, with significant benefits observed in patients with specific biomarker profiles.

Trastuzumab (Herceptin®) is a humanized anti-HER2 monoclonal antibody. Based on the promising results from the ToGA trial (19), it has been approved by both the U.S. Food and Drug Administration (FDA) and the European Medicines Agency (EMA) as the standard first-line setting, in combination with chemotherapy (cisplatin and either capecitabine or 5-fluorouracil), for patients with HER2-positive metastatic GC (10). Trastuzumab is also available in the form of antibody-drug conjugates: trastuzumab emtansine (T-DM1, Kadcyla®) and trastuzumab deruxtecan (T-DXd, Enhertu®), both formed by the anti-HER2 monoclonal antibody trastuzumab linked to a cytotoxic payload (20,21). T-DXd's payload is a

topoisomerase I inhibitor connected via a cleavable tetrapeptide-based linker. In this way, the drug is specifically delivered and selectively cleaved in HER2-expressing cancer cells, thus exhibiting an antitumour bystander effect on nearby cells, including HER2-negative cells, while limiting off-target toxic effects (21). Encouraging results from the Asian phase II DESTINY-Gastric01 trial supported FDA and EMA indications of T-DXd for the treatment of patients with locally advanced or metastatic HER2-positive GC who underwent prior treatment with a trastuzumab-based regimen. Interestingly, in the DESTINY-Gastric01 trial, T-DXd was also administered in exploratory cohorts of patients with pretreated HER2-low GC, resulting in a benefit in overall survival (22). Another phase II trial (DESTINY-Gastric02) confirmed T-DXd second-line efficacy in western GC HER2-positive patients (23). Further clinical trials testing T-DXd monotherapy and combinations with standard chemotherapy are in progress (phase III DESTINY-Gastric04 NCT04704934 and phase Ib/II DESTINY-Gastric03 NCT04379596).

Blocking angiogenesis is another key strategy in GC therapy. Ramucirumab (Cyramza®) is an anti-VEGFR2 humanized monoclonal antibody, preventing the receptor from binding its ligand VEGF. Ramucirumab is approved for the treatment of advanced GC refractory to first-line chemotherapy and it can be administered either as a single agent or associated with paclitaxel (10). The REGARD trial demonstrated the efficacy of ramucirumab monotherapy in patients with advanced GC progressing after first-line chemotherapy (24), while in the RAINBOW trial, the addition of ramucirumab to paclitaxel led to a notable extension in overall survival compared to paclitaxel alone (25).

Anti-HER2 and anti-VEGF therapies have been established as standard treatments for advanced GC in the first- and second-line setting, respectively. Nevertheless, the advantage of targeted therapy application in the perioperative or adjuvant context remains unclear and is currently under investigation (10).

Immune checkpoint inhibitors (ICIs), administered alone or in combination with other treatments, have demonstrated potent antitumour activity in various solid cancers, including gastrointestinal tumours. Several phase III clinical trials led to the approval of PD-1 inhibitors for first- and third-line treatment of unresectable or metastatic GC in various countries. Pembrolizumab (Keytruda®) is a monoclonal antibody that blocks the interaction between PD-1 and its ligands PD-L1 and PD-L2. Based on positive results from the KEYNOTE-059 single-arm phase II study (26), the FDA granted accelerated approval to pembrolizumab as monotherapy for GC patients whose tumours express PD-L1 and who have progressed on two or more prior lines of chemotherapy (10). Furthermore, following the promising results from the phase III KEYNOTE-811 trial (27), in 2021, the FDA approved pembrolizumab combined with trastuzumab and chemotherapy as the first-line treatment for advanced HER2-positive GC (10). This year, the same treatment combination has been approved as first-line treatment by EMA, but the indication is limited to those patients whose tumour expresses both HER2 and PD-L1 (combined positive score ≥ 1) (28).

Another ICI targeting the PD-1/PD-L1 axis has been recently approved by both the FDA and the EMA. In the phase III CheckMate-649 trial, nivolumab (Opdivo®), an anti-PD-1 monoclonal antibody, was tested in combination with ipilimumab (a CTLA4-inhibitor) or in combination with chemotherapy versus chemotherapy alone in metastatic HER2-negative GC patients. The chemo-free regimen involving nivolumab and ipilimumab did not demonstrate improvements in overall survival compared to chemotherapy alone. However, the addition of nivolumab to chemotherapy improved both overall and progression-free survival (29). These findings led to the inclusion of nivolumab and chemotherapy combination as one of the recommended first-line treatments for advanced GC. Further research is currently exploring the potential use of immunotherapeutic regimens in the perioperative setting (10).

All the targeted agents and ICIs approved for GC treatment are depicted in *Figure 1*. Despite the multiple therapeutic options, recurrence of GC remains a common issue, underscoring the need for further investigation of resistance mechanisms and identification of novel therapeutic targets. GC is a complex disease, and intratumoral, intrapatient, and interpatient heterogeneity pose a major barrier to the development of effective systemic treatments.
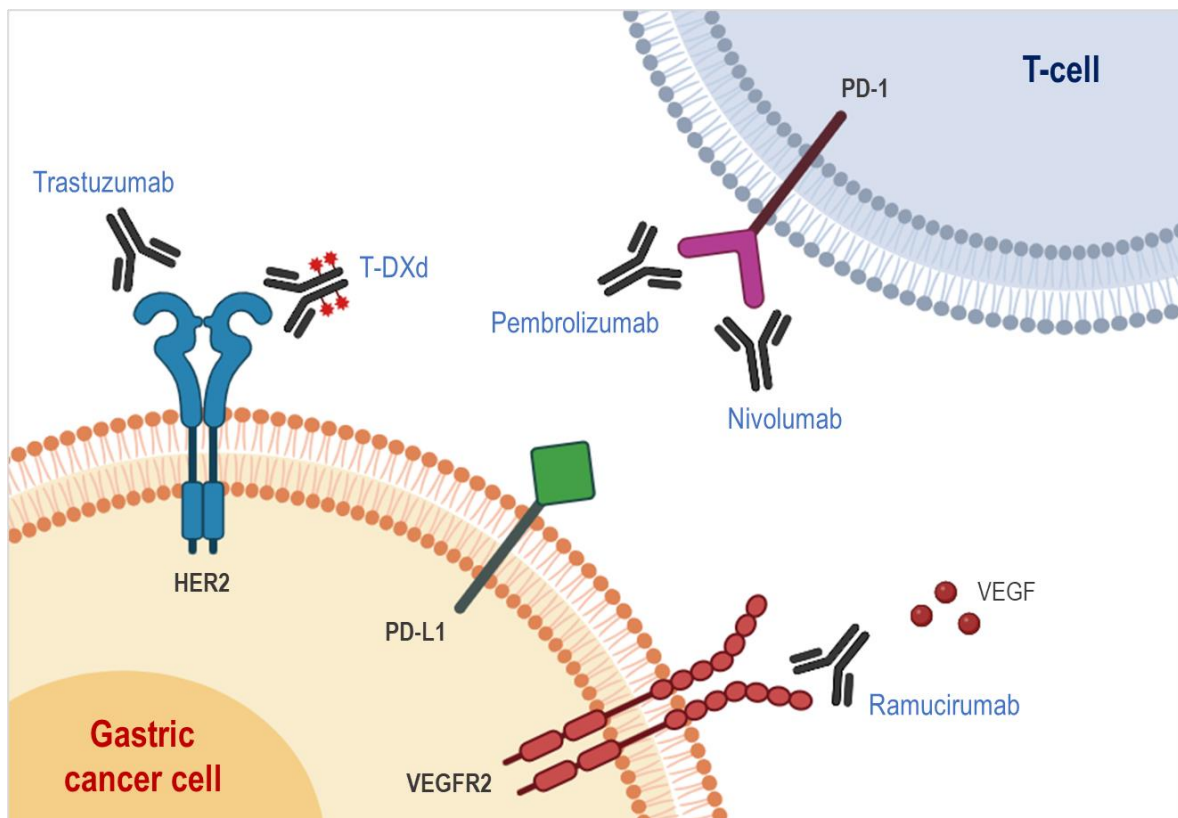
**Figure 1.**



*Figure 1. **Currently FDA/EMA-approved targeted therapies for gastric cancer treatment**. Created using BioRender.com. T-Dxd = trastuzumab deruxtecan.*

**From Histological to Molecular Classification.**

The definition of "gastric cancer" includes any malignant neoplasm arising in the region between the gastroesophageal junction and the pylorus. The vast majority of stomach tumours (~95%) are epithelial in origin and designated as adenocarcinoma. Other rarer histological

types include adenosquamous, squamous, undifferentiated carcinomas and gastrointestinal stromal tumours (GISTs) (30).

Two main pathologic classifications are used to define gastric adenocarcinomas: the Lauren classification and the more recent World Health Organization (WHO) classification.

The Lauren classification distinguishes: intestinal subtype (i), harbouring well-differentiated tumour cells which form gland tubular or papillary structures, typically arising in the distal part of the stomach; diffuse subtype (ii), characterized by scattered cells with minimal gland formation, extensively infiltrating the gastric wall; and mixed subtype (iii), displaying features of both intestinal and diffuse types (>25% of either component) (31).

The WHO classification recognizes four major histologic patterns: tubular subtype (i), resembling normal gastric epithelium, predominantly composed of well-defined glandular structures; papillary subtype (ii), exhibiting elongated finger-like projections formed by well-differentiated tumour cells; mucinous subtype (iii), presenting abundant extracellular mucin spaces with scattered clusters of poorly differentiated tumour cells; and poorly cohesive subtype (iv), including signet ring cell carcinoma, characterized by cells with abundant intracytoplasmic mucin pushing the nucleus to the periphery (32).

Histological GC classifications have been widely applied in clinical practice, even if their prognostic value is still controversial. In two studies, diffuse adenocarcinoma was correlated with a worse outcome (33,34), but this association has not been confirmed in other tested cohorts (35–37). Similarly, some reports based on the WHO classification found that poorly cohesive and mucinous adenocarcinomas have a worse prognosis compared to the papillary and tubular subtypes (38–40). However, there is no general agreement about the prognostic value of the WHO classification. Some other studies have indeed proposed that signet ring cell carcinoma, which falls under the poorly cohesive subtype, may not exhibit a significantly

different prognosis compared to other GC subtypes (41). Nevertheless, neither of these two systems was demonstrated to be adequate to properly guide patient management (42).

To satisfy this need, in the last decade, The Cancer Genome Atlas (TCGA) and the Asian Cancer Research Group (ACRG) proposed two different classifications, based on molecular profiling data.

Through an integrated high-throughput evaluation of 295 primary gastric adenocarcinomas, the TGCA identified four molecularly distinct subtypes: Epstein-Barr virus-positive (EBV$^+$) tumours (i), exhibiting recurrent *PIK3CA* mutations, extensive DNA hypermethylation, and gene amplification of *JAK2*, *PD-L1* and *PD-L2*; tumours with microsatellite instability (MSI) (ii), showing high mutation rates and mutations in known targetable genes, as *PIK3CA*, *EGFR*, *ERBB2*, *ERBB3*; genomically stable (GS) tumours (iii), displaying alterations in cell adhesion and cell migration pathways, such as *CDH1* and *RHOA* mutations and *CLDN18-ARHGAP* fusions; and tumours with chromosomal instability (CIN) (iv), characterized by significant aneuploidy and focal amplification of receptor tyrosine kinases (43).

The ACRG, profiling a similar number of patients of Asian origin, distinguished four subtypes as well: MSI tumours (i), harbouring hypermutations in the PI3K pathway and *KRAS*, *ALK* and *ARID1A* genes; microsatellite stable tumours with epithelial-to-mesenchymal transition features (MSS/EMT) (ii), showing the loss of epithelial markers; MSS/TP53 mutant (MSS/TP53$^+$) tumours (iii), frequently positive for EBV; and MSS/TP53 wild type (MSS/TP53$^-$) tumours (iv), displaying frequent amplifications in genes including *MYC*, *ERBB2* and *EGFR* (44).

While only the ACRG classification could predict prognosis, both systems may provide fundamental help in the development of personalized treatment strategies. Each subtype is

indeed associated with specific molecular alterations and thus with different putative

pharmacological targets (42,45) (Figure 2).
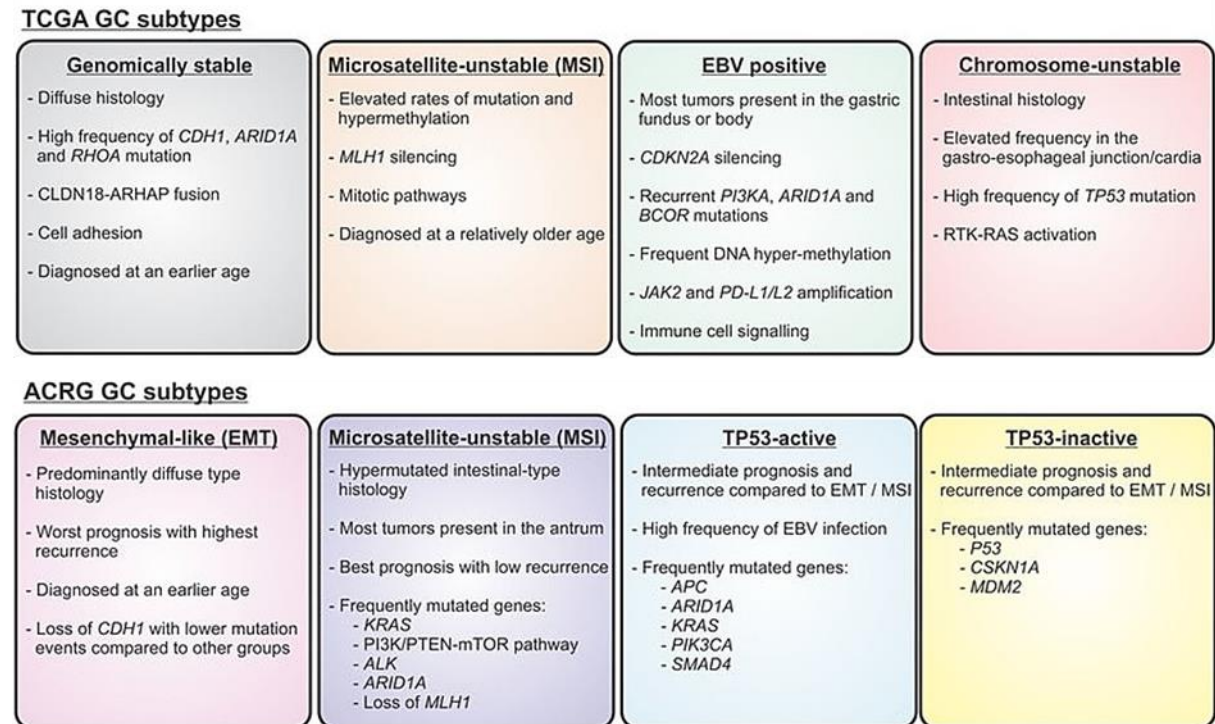
**Figure 2.**

**TCGA GC subtypes**

| Genomically stable | Microsatellite-unstable (MSI) | EBV positive | Chromosome-unstable |
|---|---|---|---|
| - Diffuse histology | - Elevated rates of mutation and hypermethylation | - Most tumors present in the gastric fundus or body | - Intestinal histology |
| - High frequency of CDH1, ARID1A and RHOA mutation | - MLH1 silencing | - CDKN2A silencing | - Elevated frequency in the gastro-esophageal junction/cardia |
| - CLDN18-ARHAP fusion | - Mitotic pathways | - Recurrent PI3KA, ARID1A and BCOR mutations | - High frequency of TP53 mutation |
| - Cell adhesion | - Diagnosed at a relatively older age | - Frequent DNA hyper-methylation | - RTK-RAS activation |
| - Diagnosed at an earlier age | | - JAK2 and PD-L1/L2 amplification | |
| | | - Immune cell signalling | |

**ACRG GC subtypes**

| Mesenchymal-like (EMT) | Microsatellite-unstable (MSI) | TP53-active | TP53-inactive |
|---|---|---|---|
| - Predominantly diffuse type histology | - Hypermutated intestinal-type histology | - Intermediate prognosis and recurrence compared to EMT / MSI | - Intermediate prognosis and recurrence compared to EMT / MSI |
| - Worst prognosis with highest recurrence | - Most tumors present in the antrum | - High frequency of EBV infection | - Frequently mutated genes: <br> - P53 <br> - CSKN1A <br> - MDM2 |
| - Diagnosed at an earlier age | - Best prognosis with low recurrence | - Frequently mutated genes: <br> - APC <br> - ARID1A <br> - KRAS <br> - PIK3CA <br> - SMAD4 | |
| - Loss of CDH1 with lower mutation events compared to other groups | - Frequently mutated genes: <br> - KRAS <br> - PI3K/PTEN-mTOR pathway <br> - ALK <br> - ARID1A <br> - Loss of MLH1 | | |

*Figure 2. **GC molecular subtypes according to TCGA and ACRG.** Modified from* (46).

Importantly, even if the two classification systems only partially overlap, probably due to the

ethnic and histological differences in the evaluated cohorts, they both identified an MSI

subgroup, accounting for 22-23% of all GC cases and characterised by well-defined features,

as high mutation frequency and favourable prognosis.

**DNA Mismatch Repair Deficiency leads to Microsatellite Instability.**

Microsatellite instability is a condition of genetic hypermutability associated with slippage

mispairing events occurring in repetitive DNA sequences. Microsatellites are short tandem

repeats typically consisting of 1-6 base pairs. These sequences are dispersed throughout the

15

genome and can be found in both coding and non-coding regions. Due to their repetitive nature, microsatellites are particularly prone to mutations involving changes in the number of repeats. Microsatellite instability arises from defects in the DNA mismatch repair (MMR) machinery (47).

The MMR system is a highly conserved pathway playing a pivotal role in the maintenance of genomic integrity. It specifically recognises and repairs base-base mismatches and small insertions/deletions that occur during DNA replication or following physical and chemical insults. MMR proteins are organised in two key protein complexes: MutS and MutL. The MutS complex is composed of heterodimeric protein pairs, which include MSH2 (MutS homolog 2) combined with either MSH6 (MutS homolog 6) or MSH3 (MutS homolog 3). The MutS complex is responsible for the initial detection of mismatches in the DNA. Specifically, MSH2/MSH6 (MutSα) recognizes single base-pair mismatches and small insertions or deletions (up to 3 nucleotides), while MSH2/MSH3 (MutSβ) primarily identifies larger insertions or deletions (up to 13 nucleotides). In eukaryotic cells, DNA error recognition is followed by an excision step during which MutS recruits MutLα, constituted by MLH1 (MutL homolog 1) and PMS2 (Postmeiotic Segregation Increased 2) proteins. MutS and MutLα form a tetrameric complex orchestrating the subsequent steps in the repair process. Eukaryotic MutLα has a latent endonuclease activity and introduces nicks primarily in the nascent DNA strand. After the DNA incision step, Exonuclease 1 (EXO1) is recruited and activated by either MSH2 or MLH1; once activated, EXO1 excises the newly-synthesised DNA strand, and the DNA excision gap is re-synthesised by DNA polymerase δ (Polδ). When DNA re-synthesis is complete, the remaining nick is ligated by DNA ligase I (48). The main steps of the eukaryotic MMR pathway are illustrated in Figure 3.
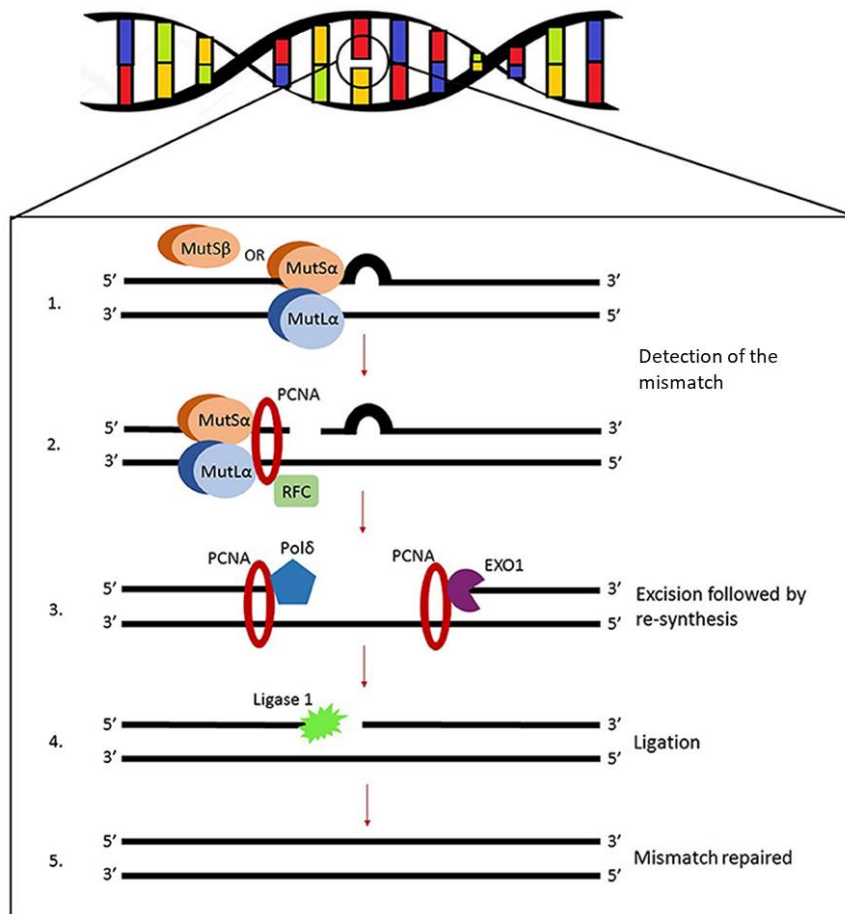
**Figure 3.**



*Figure 3.* **Illustration of the eukaryotic MMR system.** *Modified from* (49). *EXO1 = exonuclease 1; PCNA = proliferating cell nuclear antigen; Pol δ = DNA polymerase delta; RFC = replication factor C.*

Genetic defects or loss of expression of one or more MMR proteins determine the deficiency of the complexes and the subsequent ineffective DNA repair (47).

**Clinical Relevance of Microsatellite Instability in Familial and Sporadic Cancer.**

Microsatellite instability plays a significant role in hereditary cancer syndromes. These syndromes are caused by inherited mutations in specific genes associated with the DNA mismatch repair system.

Lynch syndrome, also known as hereditary nonpolyposis colorectal cancer, is one of the most well-known familial cancer syndromes linked to MSI. It is primarily caused by mutations in MMR genes like *MLH1*, *MSH2*, *MSH6*, and *PMS2*, but it can also result from alterations in the *EPCAM* gene, impacting the function of the nearby *MSH2* gene. In individuals with Lynch syndrome, MMR impairment predisposes them to a significantly elevated risk of developing certain types of cancers, primarily colorectal cancer. However, Lynch syndrome can also be associated with other malignancies, such as endometrial, ovarian, urothelial and gastric cancer (50).

Another rarer genetic condition linked to MSI is the constitutional mismatch repair deficiency (CMMRD) syndrome, resulting from biallelic germline mutations in one of the four key MMR genes, *MLH1*, *MSH2*, *MSH6* or *PMS2*. This syndrome is associated with a high predisposition to a broad spectrum of cancers, including haematological, brain and gastrointestinal tract tumours. Differently from Lynch syndrome in which MMR impairment is partial because only one gene copy displays a germline mutation, patients affected by CMMRD syndrome present a complete loss of MMR function, resulting in a constitutional MSI, a much higher level of DNA replication errors and the development of cancer at an early age, often in childhood or adolescence (51,52).

Individuals affected by either Lynch or CMMRD syndrome undergo regular surveillance and screening for associated neoplasms (53,54). Gastric cancer risk in individuals with Lynch syndrome can range up to 9%. However, this risk varies according to the specific genotype, with carriers of *MLH1* and *MSH2* mutations having a higher risk compared to carriers of *MSH6* and *PMS2* mutations (55). In the USA, the National Comprehensive Cancer Network (NCCN) has recently advised regular gastric surveillance for patients harbouring *MLH1*, *MSH2*, *MSH6*, and *EPCAM* gene mutations, starting between 30 and 40 years of age and repeating every 2-4 years (56). On the contrary, European institutions such as the British Society of

Gastroenterology (BSG), the European Hereditary Tumour Group (EHTG), and the European Society of Coloproctology (ESCP) do not recommend routine gastric surveillance in Lynch syndrome patients, unless they are enrolled in clinical trials (57,58). CMMRD patients develop gastrointestinal manifestations very early, predominantly in the form of multiple colorectal adenomas evolving in early-onset colorectal cancer. Surveillance for digestive tract cancers is based on colonoscopy and generally begins at 6 years of age (59).

Microsatellite instability is also present across multiple sporadic malignancies, most commonly in endometrial, ovarian, and gastrointestinal carcinomas (10-30% frequencies) (Figure 4).

**Figure 4.**
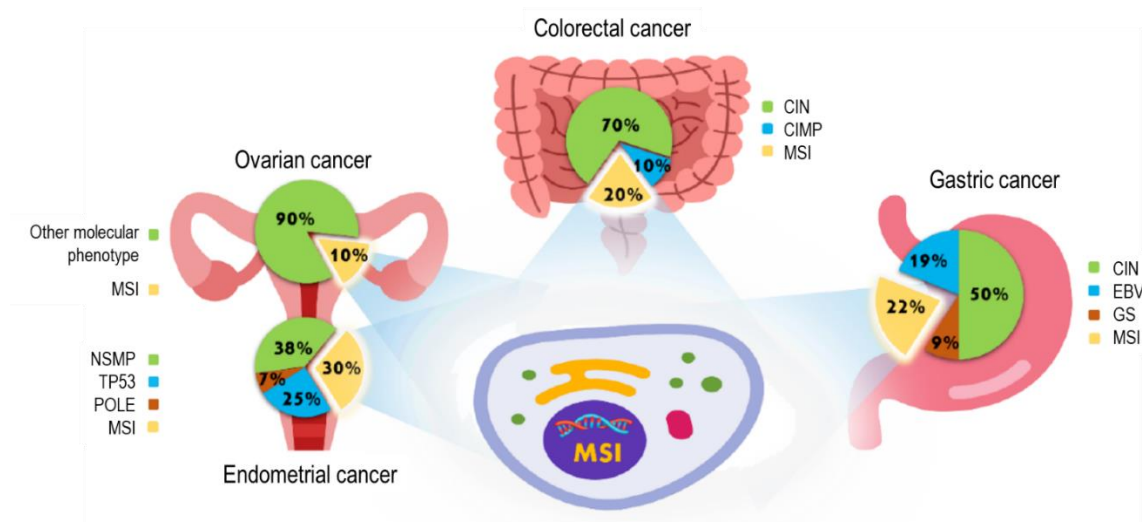


*Figure 4. **Frequency of microsatellite instability in gastrointestinal and gynecologic cancers.** Modified from (60). CIN = chromosome instability; CIMP = CpG island methylator phenotype; MSI = microsatellite instability; EBV= Epstein–Barr virus; GS = genomically stable; NSMP = no specific molecular profile; POLE = DNA polymerase epsilon.*

In the sporadic onset, MMR impairment most frequently occurs by hypermethylation of CpG islands in the promoter region of *MLH1*, leading to epigenetic gene silencing, but in some cases, MSI is due to biallelic loss-of-function mutations in MMR genes (61). In cancer types with high MSI prevalence, assessment of microsatellite status has become crucial for

prognosis, surveillance, and therapeutic decisions. Methods used in the clinical practice for MSI detection include immunohistochemistry (IHC), to evaluate the expression of the main MMR proteins, or molecular approaches for the analysis of microsatellite sequences (60). MSI molecular testing is typically conducted using polymerase chain reaction (PCR)-based amplification and measuring via capillary electrophoresis the size of the amplified DNA fragments. There are two widely used commercial panels for MSI-PCR: the Bethesda panel and the Pentaplex panel. The Bethesda panel comprises five pre-defined genomic regions, consisting of two single-nucleotide markers (BAT25, BAT-26) and three dinucleotide markers (D2S123, D5S346, and D17S250). The Pentaplex panel involves five mononucleotide loci, namely BAT-25, BAT-26, NR-21, NR-24, and NR-27 (62,63) (Figure 5).

**Figure 5.**
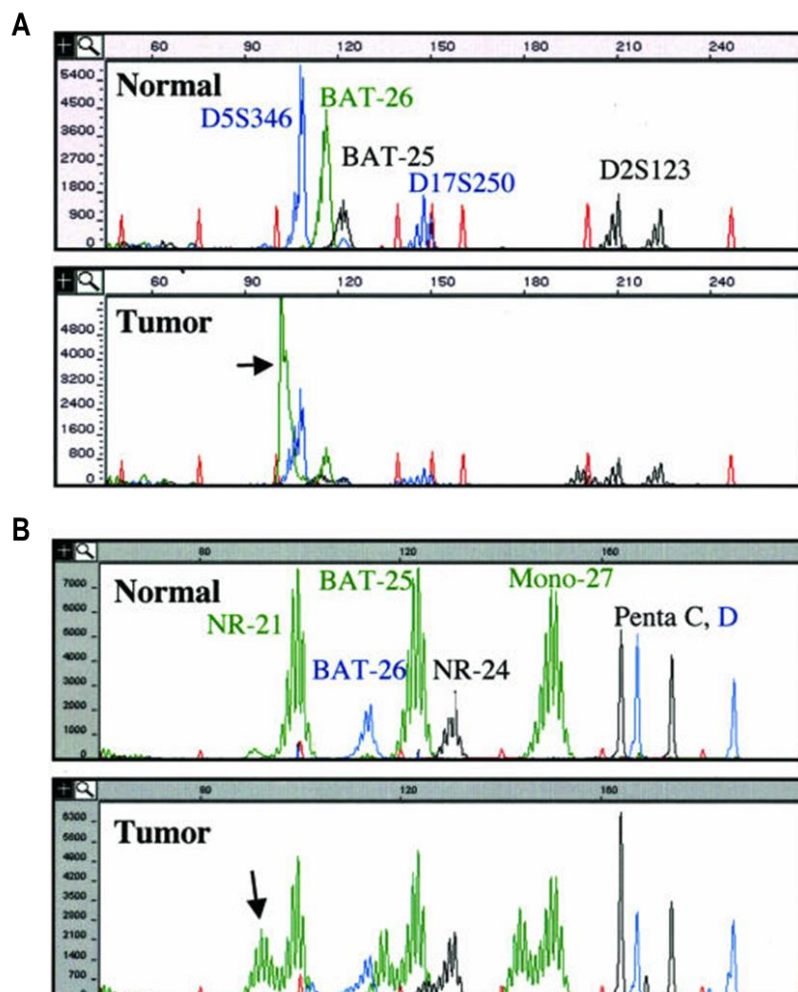
*Figure 5. **Capillary electrophoresis results from the Bethesda panel (A) and the Pentaplex panel (B) assays.** Modified from (64). X-axis indicates amplicon size (bases); y-axis indicates fluorescence intensity. Red peaks are internal size standards. Green, blue, and black peaks are amplification products from microsatellite loci. MSI status is evaluated on the basis of the shift in the size of the amplification products in the tumour specimen when compared with normal DNA. The arrow indicates an example of shifted locus in the tumour sample for each assay.*

On the basis of the number of unstable markers, microsatellite status is determined as follows: high microsatellite instability (MSI-H) (i) is defined when there are 2 or more unstable loci; low microsatellite instability (MSI-L) (ii) is defined in the presence of a single unstable locus; microsatellite stability (MSS) (iii) is defined when all the examined microsatellites are stable (65). MSI-L and MSS tumours exhibit comparable molecular and clinical characteristics. Thus, MSI-L and MSS patients are currently grouped together in clinical research studies (60).

MSI testing methods based on next-generation sequencing (NGS) have been developed as well. Some NGS gene panels for MSI detection include MSIPlus (66) and ColoSeq (67), optimized for colorectal cancer. MSIPlus examines 16 microsatellite sites in addition hotspots mutations within oncogenes such as *KRAS*, *NRAS*, and *BRAF* (66), while ColoSeq identifies mutations, deletions, or complex structural changes in MMR genes (67). Other approaches integrate NGS data with computational algorithms such as mSINGS (68), MSISensor (69), MOSAIC (70) and MANTIS (71), which allow the assessment of numerous microsatellite loci predominantly located in protein-coding regions. These tools calculate an instability score on the basis of microsatellite length distributions in normal and tumour samples (71).

Another possible way to infer MSI status could be through the analysis of specific mutational signatures associated with DNA mismatch repair deficiency. Mutational signatures represent specific patterns of alterations, encompassing single base substitutions, indels, copy number variants and structural variants. These patterns, arising from mutagenic processes comprising some form of DNA damage, provide profound insights into the aetiology of various diseases,

including cancer. The COSMIC catalogue includes several patterns specifically associated with MSI include single-base substitution (SBS) signatures – such as SBS6, SBS14, SBS20, SBS21, SBS26, and SBS44 – and small insertion and deletion (ID) signatures – like ID7 (72,73).

MSI testing plays a major role in the classification of sporadic colorectal cancer (CRC). NCCN guidelines recommend MSI molecular testing or IHC for MMR proteins to be done in all newly diagnosed CRC cases, especially at stage II (56). MSI status is indeed a well-established CRC prognostic and predictive biomarker, fundamental for guiding clinical management. Stage II/III MSI-H CRCs are associated with significantly better disease-free survival and overall survival compared with MSI-L/MSS cases at the same disease stage. Stage II MSI-H patients show also a lack of benefit from 5-fluorouracil-based adjuvant chemotherapy. However, the benefit is still uncertain in stage III CRC, where FOLFOX adjuvant chemotherapy remains the standard of care regardless of MSI status (74).

The clinical relevance of the MSI status in sporadic cancer is mostly due to its role as a strong predictor of response to immunotherapy (75). Cancer cells generate neoantigens, which are expressed on the cell surface via major histocompatibility complex (MHC) class I molecules. Cytotoxic CD8^{+} T-cells play a crucial role in antitumour immune responses by recognising neoantigens presented on MHC molecules through their T cell receptors (TCR). Beyond TCR-MHC interaction, T-cell activation is also affected by co-stimulatory and co-inhibitory signals. One of the main co-stimulatory pathways is represented by the interaction of the T-cell CD28 receptor with B7 family ligands, such as CD80 and CD86, which are expressed on antigen-presenting dendritic and B-cells. However, the cytotoxic T lymphocyte antigen 4 (CTLA4), not detectable on the cell surface of naïve T-cells but highly induced after T-cell activation, competes with the CD28 receptor in binding to B7 ligands leading to T-cell anergy. Cancer cells can take advantage of the CTLA4-B7 axis producing B7 ligands and thus escaping antitumour T-cell immunity. A further immune evasion opportunity for cancer cells is

represented by the programmed cell death-1 (PD-1) receptor, which is another key co-inhibitory receptor on the T-cell surface. By means of overexpression of programmed cell death-ligand 1 (PD-L1), cancer cells can indeed activate the PD-1/PD-L1 pathway in T-cells, thus inducing and maintaining immune tolerance (76). Monoclonal antibodies targeting the immune checkpoints CTLA-4 and PD-1 have been developed and tested for the treatment of metastatic tumours. Since the last decades, immune checkpoint inhibitors (ICIs) demonstrated to improve survival in multiple solid tumours, including metastatic melanoma and non-small cell lung cancer, leading to their clinical approval (77–81).

Regarding gastrointestinal malignancies, the first trials testing anti-PD-1 monoclonal antibodies were carried out in unselected CRC metastatic cases and showed limited clinical responses (82). However, when evaluated in the specific context of metastatic MSI-H/MMR-deficient CRC, anti-PD-1 ICIs demonstrated unprecedented efficacy (83,84). Promising results from phase II clinical studies led to accelerated approval of anti-PD-1 monoclonal antibodies and pembrolizumab is now the first-line treatment for patients with MSI-H/MMR-deficient CRC. Both the FDA and the EMA also approved the combination of nivolumab and the anti-CTLA4 antibody ipilimumab for the treatment of refractory MSI-H/MMR-deficient CRCs (85). ICIs have reshaped the treatment of advanced MSI-H CRC over the past decade. However, even more promising results are emerging when ICIs are administered in the neoadjuvant setting, opening new curative possibilities also for patients with early-stage tumours (86).

Despite this success, some MSI CRCs are refractory to immunotherapeutic regimens, probably due to both intrinsic and acquired resistance mechanisms (87). A highly immunosuppressive tumour microenvironment and a significant intratumour heterogeneity can mediate resistance to immunotherapy. Thus, developing new immunotherapeutic targets and therapeutic strategies

is a hot topic nowadays. Several ongoing trials are focused on testing new drug combinations or remodelling ICI molecular structures to improve their solubility and stability (85).

**Gastric Cancer with Microsatellite Instability: Molecular Features and Therapeutic Landscape.**

In recent years, several investigators have contributed to MSI GC molecular profiling, identifying signalling pathways and genes specifically altered in this molecular subtype. Through the analysis of 63 hypermutated GC cases, TCGA identified 37 genes significantly mutated in the MSI subgroup. These genes are involved in diverse cellular processes such as the maintenance of DNA integrity and cell cycle control (*TP53, CUL1, FBXW7, NF1, PAX6*), transcriptional regulation and chromatin remodelling (*ZBTB20, HDAC4, TBL1XR1, EP300*), signal transduction including phosphoinositide-3-kinase (PI3K) pathway (*PIK3CA, PTEN*) and Wnt pathway (*RNF43, CIC*). Moreover, MSI GC tumours showed a high expression of pro-mitogenic players, such as AURKA A/B, E2F, FOXM1, PLK1, and MYC activation targets (43).

PI3K pathway activation plays a pivotal role in GC development and progression, contributing to escape from apoptosis, sustained proliferation, and invasive phenotype (88). TCGA showed *PIK3CA* gene, encoding for catalytic subunit p110 isoforms α of class IA PI3K, to be mutated in 42% of analysed MSI GC tumours. Furthermore, H1047R *PIK3CA* hotspot mutation was specifically enriched in the MSI subgroup (43). In accordance, other investigators showed that only MSI GC cases harboured the H1047R mutation which was observed in 8 out of 39 MSI cases and was significantly associated with MSI status (89). Another report demonstrated a robust association between *PIK3CA* gene mutations and MSI status. Interestingly, in the same study, MSI patients harbouring *PIK3CA* mutations exhibited a less favourable 5-year survival rate (40%) in comparison to MSI patients with the wild-type gene (70.4%). Additionally, when

the prognosis was examined according to the specific hotspot of *PIK3CA* mutation, a completely different outcome was found in the presence of mutations in exon 9 (E542K, E545K) compared to exon 20 (H1047R), showing 0% and 80% 5-year survival rates, respectively (90).

According to TCGA analysis, *KRAS* is among the genes significantly mutated in the MSI subtype. More specifically, *KRAS* mutations are present in 24% of MSI GCs (43). The association between *KRAS* and MSI status was further confirmed by a more recent analysis performed on 595 GC patients identifying *KRAS* mutations in 14.9% of MSI and 1.2% of MSS GCs (91). Consistently, a large international multicentre study examining *KRAS* and *BRAF* alterations in 712 patients with locally advanced resectable GC reported that *KRAS* mutations were enriched in MMR-deficient tumours. Interestingly, in the same study, a *BRAF* mutation was detected only in a single GC case (92). Although MSI GCs and MSI CRCs share a similar prevalence of *KRAS* mutations, it is worth noticing that MSI GCs do not exhibit the BRAF V600E mutation commonly described in CRC (43).

Receptor tyrosine kinases (RTKs), generally playing a major role in GC, did not display gene amplification in the MSI subtype. However, MSI GCs usually show many hotspot mutations in RTK genes like *ERBB2*, *ERBB3* and *EGFR* (43).

Another gene frequently mutated in MSI GC is *ARID1A*, involved in chromatin remodelling and identified as a tumour suppressor gene in both GC and CRC (43,93–95). *ARID1A* mutations generally co-occur with *PIK3CA* mutations and MSI status in GC (94,96). A meta-analysis proposed that *ARID1A* alterations could play a role in MSI GC development (97). Consistently, low expression of *ARID1A*, particularly in early-stage undifferentiated carcinomas, is correlated with poor overall survival in GC patients (98).

Importantly, MSI GCs demonstrated also frequent truncating mutations in the major histocompatibility complex class I genes, including *B2M* and *HLA-B* (43). Hypermutated tumours benefit from these alterations as they result in the loss of expression of the HLA class I complex, leading to a reduced neoantigen presentation to the immune system (99,100).

The MSI status is not routinely tested in clinical practice for GC patients, as its role as a biomarker is still controversial. Similarly to CRC, many reports related the MSI status in GC patients to a good prognosis. An extensive meta-analysis comprising 48 studies revealed that MSI GC patients who underwent surgery alone showed better overall survival when compared to the MSS group (101). The favourable prognostic impact of MSI-high status after radical surgery has been also reported in post hoc analyses of randomised controlled trials (102–104). Furthermore, since adjuvant and perioperative chemotherapy are recommended for GC, several studies have explored the potential predictive significance of MSI status in chemotherapy response. A large-scale study involving 1,990 GC patients demonstrated improved disease-free survival in stage II/III MSS, but not in MSI patients, who received 5-fluorouracil-based adjuvant chemotherapy after gastrectomy (105). Similar results were reported in a post-hoc analysis of the CLASSIC trial, where capecitabine and oxaliplatin adjuvant chemotherapy did not significantly impact survival in MSI GC cases (104). Furthermore, an analysis of 1,276 GC cases (stage II/III) revealed that MSI patients displayed a better prognosis compared to MSS patients when treated with surgery alone, but this benefit was attenuated when chemotherapy was administered (106). The negative predictive value of the MSI status for chemotherapy efficacy was also highlighted in the post-hoc analysis of the MAGIC trial, indicating that MSI/MMR-deficient patients treated with surgery alone showed a more favourable survival than MSI/MMR-deficient patients undergoing both surgery and perioperative chemotherapy (107). More recently, a multinational meta-analysis pooling together data from four large clinical trials (MAGIC, CLASSIC, ARTIST and ITACA-S) found that the MSI GC subtype

26

was associated with superior 5-year disease-free survival and 5-year overall survival compared to the MSS subtype. Notably, patients with MSS or MSI-L status showed benefit from chemotherapy plus surgery, whereas the same benefit was not observed in MSI-H GCs (108). While the positive prognostic value of MSI in GC is widely acknowledged, the evidence supporting MSI as a negative predictor for the efficacy of adjuvant or neoadjuvant chemotherapy remains questionable. This uncertainty is mainly due to the limited number of MSI GC patients enrolled in each individual study and to the retrospective nature of the reported analyses (109).

Over the past few years, given the striking outcomes obtained in CRC patients, immunotherapy has been tested also in GC patients and regimens based on the anti-PD1 ICIs pembrolizumab and nivolumab and anti-CTLA4 ICI ipilimumab granted approval for treatment of patients with unresectable GC. Unfortunately, however, immunotherapy has not revolutionized the therapeutic landscape of GC as only a minority of patients have objective responses to ICIs (110). From this standpoint, the importance of identifying solid predictors of response clearly emerges. The specific hypermutated phenotype of MSI GC constitutes the logical foundation for ICI administration in this subgroup, as the abundant production of peptides functioning as neoantigens can trigger T-cell recruitment and activation (111). However, even if clinical trials testing these ICIs in GC demonstrated efficacy in MSI patients in each treatment line, the low incidence of MSI in metastatic stages (2-5%) limited the number of MSI cases enrolled in the studies and thus the statistical significance of individual post-hoc analyses. In the KEYNOTE-059 trial, MSI patients (n = 7) showed a higher overall survival (57.1%) upon pembrolizumab treatment compared to MSS patients (9%) (26). Consistently, in the CHECKMATE-032 trial, exploring the activity and safety of nivolumab monotherapy and nivolumab plus ipilimumab regimens in a PD-L1 unselected metastatic oesophagogastric cancer population, MSI patients (n = 11) reached a longer median overall survival (about 15 months) compared to MSS patients

and patients with unknown microsatellite status (112). Furthermore, a meta-analysis, including data deriving from the KEYNOTE-061, the KEYNOTE-062, the CHECKMATE-649 and the JAVELIN Gastric 100 phase III studies, showed a significantly improved overall survival upon anti-PD1 treatment in MSI GCs (n = 123, 4.8% of the entire cohort) compared to MSS cases (113). Taken together, these results strengthen the potential of the MSI status as a predictive biomarker for ICI efficacy in GC. Importantly, in 2022, EMA extended pembrolizumab indication for the treatment of 4 MSI-H/MMRd tumour types, including recurrent unresectable or metastatic GC, thus leading to the second approval for pembrolizumab in Europe based on the MSI-H/dMMR status as a predictive biomarker (114). Another putative alternative biomarker could be the tumour mutation burden (TMB), which demonstrated to be useful for the prediction of ICI efficacy in various cancer types (115). In an exploratory analysis of the KEYNOTE-061 trial, pembrolizumab led to an overall survival benefit compared with paclitaxel in the TMB-high GC cohort and this clinical efficacy was confirmed also when MSI patients were excluded (116). Nevertheless, the potential of TMB as a standalone or valuable biomarker for GC requires further investigation with more extensive patient cohorts.

An increasing number of reports are pointing out MSI GC as an entity characterized by low responsiveness to chemotherapy but heightened sensitivity to immunotherapy. However, the molecular complexity of the disease must be considered in order to effectively direct patient care. Indeed, GC high heterogeneity is emerging as a major concern for proper MSI GC stratification and treatment. Importantly, our team and other investigators reported the existence, among MSI GC patients, of two distinct populations endowed with peculiar transcriptional traits and different survival probabilities. Starting from the analysis of MSI GC patient-derived xenografts, our group extrapolated a cancer cell-intrinsic MSI signature able to identify a subset of MSS patients endowed with a better prognosis. Moreover, when the same signature was applied to MSI cases from the ACRG dataset (GSE66229), we managed to

discriminate a subgroup of patients with a lower MSI-like score showing a poorer outcome (117). In line with this observation, Yang et al. analysed gene expression profiles from 47 MSI GCs and found that they clustered in two subgroups of similar size, namely MSI-H1 (n = 24) and MSI-H2 (n = 23). The survival rate in the MSI-H1 subgroup was significantly lower compared to the MSI-H2 subgroup. Furthermore, no significant survival difference was observed when MSI-H1 cases were compared to MSS cases. Interestingly, the authors did not find any difference in TMB between MSI-H1 and MSI-H2 GCs but highlighted the high suppressive tumour microenvironment as a possible explanation for the poor outcome of the MSI-H1 subgroup (118).

The clinical heterogeneity of MSI GC also emerges from the different responses to ICI treatments. Among the 67 MSI GC patients enrolled in the Keynote-059, -061, and -062 trials, the overall response rates to pembrolizumab monotherapy were close to 50%, suggesting that nearly half of the tumours are intrinsically resistant (119). Furthermore, results from another clinical trial − a phase II study in which pembrolizumab monotherapy was tested in 19 advanced MSI GC patients − suggest that complete and long-lasting responses are achieved in very few cases (120).

In addition to inter-patient variability, the response to immunotherapy could also be affected by the high degree of intra-tumoral heterogeneity. For example, some biomarkers, like PD-L1 expression and MSI status, could be heterogeneous in time or space, possibly reducing the accuracy of ICI efficacy prediction. Furthermore, the presence of specific alterations in specific cell populations, such as secondary inactivation of additional MMR components (i.e. *MSH3/MSH6* frameshifts in MLH1-deficient cells), DNA polymerases *POLE* and *POLD1* mutations, *NOTCH4* mutations, co-stimulatory molecule overexpression and activation of antigen processing pathways, could affect tumour immunogenicity and immune cell infiltration (121,110).

Further exploration of MSI tumour biology is thus required to optimise both stratification and therapeutic paradigms. The knowledge of key MSI evolutionary patterns together with the identification of determinants of response/resistance to ICI treatment should be exploited to improve patient stratification and to maximise the eradicating potential of immunotherapeutic regimens.

In recent years, genome-scale CRISPR/Cas9 screens conducted in hundreds of human cancer cell lines from multiple cancer types led to the emergence of the RecQ DNA helicase Werner (WRN) as a synthetic lethal target in MSI cells (122,123). WRN inactivation has shown a selective impact on the viability of MSI but not MSS colorectal and endometrial cancer cell lines (124). In particular, in MSI cells, WRN depletion led to the occurrence of double-strand DNA breaks, triggering apoptosis and inducing cell cycle arrest (125). Importantly, WRN inhibition has been demonstrated to be effective also in MSI colorectal cancers that are refractory to targeted therapies, chemotherapy and immunotherapy (126). These data underscore WRN as a promising candidate for drug targeting in MSI cancers and the first WRN inhibitor has already been synthesized and is under preclinical investigation (127).

**Available Immunocompetent Gastric Cancer Mouse Models.**

Mouse immunocompetent models play a pivotal role in cancer research due to their ability to closely mimic the complex interactions between a functioning immune system and a developing tumour. These models may offer valuable insights into various aspects of cancer, including tumour evolution, development, and responses to immunotherapy.

Syngeneic and transgenic mouse models are two distinct approaches commonly used in cancer research to obtain *in vivo* cancer models. Syngeneic models involve the injection of mouse-derived cancer cells into genetically identical mice, allowing the study of tumour growth and

immune responses within a competent host immune system. In contrast, transgenic models entail genetically engineering mice altered in specific oncogenes or tumour suppressor genes, leading to the spontaneous development of tumours that recapitulate human cancer progression (128–130).

Immunocompetent GC mouse models have rarely been reported and very few of them specifically recapitulate the MSI subtype. Current available syngeneic GC models include MFC cells derived from C57BL/6 forestomach carcinoma (131) and 4 cell lines (YTN2, YTN3, YTN5, YTN16) established from N-methyl-N-nitrosourea-induced glandular stomach carcinoma in a *TP53* heterozygous knockout C57BL/6 mouse (132).

Some examples of transgenic GC mouse models are: the insulin-gastrin (INS-GAS) mouse (i), which expresses the gastrin gene under the control of the insulin promoter. Elevated gastrin levels lead to hyperplasia and spontaneous tumorigenesis in the gastric mucosa (133); K19-Wnt1 and K19-Wnt1/C2mE mice (ii), developed to investigate the role of Wnt and prostaglandin E2 pathways in gastric tumorigenesis (134); Trefoil factor 1 (TFF1)-KO mouse (iii), presenting a deficiency in the TFF1 tumour suppressor gene, useful for investigating genetic and environmental factors influencing GC (135); gp130$^{Y757F/Y757F}$ mouse (iv), carrying a homozygous mutation in the IL-6 signal transducer, which leads to abrogation of SHP2-Ras-ERK signalling and GC development (136); Pdx-1-Cre/Smad4$^{F/F}$/Trp53$^{F/F}$/Cdh1$^{F/+}$ mouse (v), in which conditional concomitant knockout of *SMAD4* and *TP53* together with *CDH1* heterozygosity accelerates the development and progression of gastric adenocarcinoma (137).

More recently, some authors established transgenic mouse models aiming at recapitulating specific TCGA GC subtypes. Starting from C57BL/6 embryonic stem cells, Seidlitz et al. generated 3 mouse models harbouring alterations in pathways that specifically characterize CIN and GS GC subgroups (CIN, GS-TGBF and GS-Wnt mice) (138).

31

Other approaches implied Electroporation-based Genetically Engineered Mouse Models (EPO-GEMMs). In this method, transposon-based vectors encoding cDNAs or CRISPR/Cas9 constructs targeting endogenous genes are delivered into the tissue through a precise surgical procedure and a short electric pulse. This process lets vectors enter a specific group of cells. In such a context, in case specific mutations or combinations of mutations provide a selective advantage, localized tumours develop at the site of electroporation. Taking advantage of EPO-GEMM and CRISPR/Cas9 techniques some authors inactivated the *TP53* gene alone or in combination with *MSH2* knockout, thus generating a setting in which to directly compare MSI and MSS GCs (139).

**AIMS OF THE PROJECT**

The major goal of the project is the *ex vivo* generation of syngeneic GC MSI models mimicking the key known molecular features of MSI tumours. Obtained models should be injectable into immunocompetent mouse models and potentially useful for the investigation of mechanisms underlying MSI GC clinical heterogeneity.

Interesting future applications may encompass the study of immune escape dynamics and regulators of the response to immunotherapy regimens, in order to identify new vulnerabilities as well as prognostic markers and determinants of resistance to ICIs which could be exploited as predictive biomarkers in the clinical practice.

**MATERIALS AND METHODS**

**BALB/c mouse gastric organoids derivation and culture.**

Healthy stomachs were explanted from three 10-week-old BALB/c mice (Charles River Laboratories, Inc.) without subjecting mice to preventative starvation. The stomachs were collected in ice-cold PBS and further processed within 15 minutes from explant. Gland isolation protocol was adapted by (140). In a culture dish, a scalpel was used to incise the stomachs laterally along the great curvature and remove most of the feed present in the gastric lumen. Chyme residuals were then removed with five gentle washes in ice-cold PBS. The stomachs were moved with forceps in a new culture dish with 5 mL of cold chelation buffer (10 mM EDTA, 5.6 mM $Na_2HPO_4$, 8.0 mM $KH_2PO_4$, 96.2 mM NaCl, 1.6 mM KCl, 43.4 mM sucrose, 54.9 mM D-sorbitol, 0.5 mM DL-dithiothreitol in distilled water) and epithelium fragments were scraped off the internal mucosa in the solution using a clean scalpel. Fragment suspension was collected in a 15 mL conical tube and gently mixed for 1 hour on an orbital rocker at 4 °C. Tube was put in ice vertically and tissue fragments were allowed to settle down for 5 minutes. The supernatant was discarded and the tube was filled with 5 mL of cold dissociation buffer (54.9 mM D-sorbitol, 43.4 mM sucrose in PBS). The tube was vortexed for 10 seconds and put again in ice vertically. As soon as big residual tissue fragments were settled at the bottom (about 10 seconds), the supernatant was transferred to a new 15 mL tube and the pellet was discarded. The total number of isolated glands was assessed by counting the gland number in a 10 μL suspension drop. The glands were centrifuged at 65 g for 10 minutes at 4 °C and the supernatant was discarded. The pellet was suspended in a proper volume of Matrigel™ (Corning) supplemented with EGF (50 ng/mL) and Y-27632 (10 μM) and the glands were seeded in a 24-well plate (100 glands/15 μL Matrigel™). The plate was placed in a $CO_2$ incubator (37° C, 5% $CO_2$) for 15 minutes to allow Matrigel™ complete polymerization.

Matrigel™ drops were overlayed with in-house produced 50% L-WRN conditioned medium (1:1 dilution in Advanced DMEM/F12 (Invitrogen)) (141) supplemented with penicillin/streptomycin (Gibco), Glutamax (Gibco), 10 mM HEPES, 1x B27 (Invitrogen), 1 mM N-acetylcysteine (Sigma-Aldrich), 50 ng/mL EGF, 100 ng/mL FGF10 (Cell guidance systems), 10 nM Gastrin I (Tocris), 500 nM A-8301 (MedChem Express), 10 µM Y-27632 (MedChem Express). The plate was cultured in the $CO_2$ incubator and the medium was refreshed every 3 days. As a stable growing culture was assessed, organoids were maintained in Matrigel™ without any growth factor addiction and regularly split 1:4-1:6 twice a week. Trypsin-EDTA (Gibco) was used to dissociate organoids during passages.

**Phase-contrast imaging.**

Organoids were dissociated into small cell clumps using Trypsin-EDTA (Gibco), seeded in Matrigel™ in the usual culture conditions and allowed to regrow for 2-3 days. Phase-contrast images were taken on an inverted microscope (Leica DFC350 FX).

**Whole-mount immunofluorescence.**

For immunofluorescent staining, organoids were dissociated into small cell clumps and seeded in Matrigel™ on 1.5 µm-thick round coverslips fit in a 24-well plate. Organoids were allowed to regrow for 2-3 days and then fixed with 4% paraformaldehyde in PBS for 15 minutes. After 2 washes in PBS, organoids underwent a permeabilization step in a 20mM HEPES, 0.3% Triton X-100 solution in PBS for 5 minutes followed by saturation in 4% BSA solution in PBS for 30 minutes. Organoids were stained with the following primary antibodies: anti-LGR5 (Abcam, Ab273092), anti-Ki67 (Abcam, Ab15580), Anti-MUC5AC (Santa Cruz, sc-21701), Anti-Pepsinogen II/PGC (Abcam, Ab255826). Images were captured using a Leica SP8 laser confocal microscope.

**Analysis of alterations in MMR genes in MSI-high cases from GEA and TCGA datasets.**

Genomic DNA and RNA are routinely extracted from patient-derived xenografts from our gastroesophageal adenocarcinoma (GEA: Gastro-Esophageal Annotated) platform (117) using ReliaPrep™ gDNA Miniprep system (Promega) and Maxwell® RSC miRNA tissue kit (Promega) respectively, according to the manufacturer's instructions. Microsatellite status was assessed in-house using a fluorescent, multiplex PCR-based test (OncoMate™ MSI Dx Analysis System, Promega), while whole-exome and RNA sequencing were performed in outsourcing by Macrogen (Seoul, South Korea). Copy number, mutation and expression data relative to the TGCA gastric cancer dataset (43) were downloaded from the *cBioportal* website (https://www.cbioportal.org/), together with microsatellite status and molecular subtype annotations. MSI-high cases from both cohorts were analysed for the presence of putative loss-of-function alterations in MutL and MutS genes (*MLH1, MLH3, PMS1, PMS2, MSH2, MSH3, MSH6*). Only truncating and splicing mutations, deep and shallow deletions and low gene expression (defined as Z-score $\leq$ -1) were included. Oncoprint was drawn using *ComplexHeatmap* R package (142). Frameshifts and stop mutations were represented using the same label ("trunc mutation"), as usually done in representations from the *cBioPortal* platform. Co-occurrence/mutual exclusivity analysis was performed using *Rediscover* R package which computes the Poisson binomial method to estimate co-occurrent/mutual exclusive events (143). Pearson correlation was performed using the *cor()* function from *stats* R package (144). Data from both analyses were drawn using *ggplot2* R package (145).

**Mlh1 and Msh2 knockout in BALB/c mouse gastric organoids using CRISPR/Cas9 system with stable Cas9 expression.**

To generate stable Cas9-expressing cells, BALB/c gastric organoids were dissociated into single cells using Trypsin-EDTA (Gibco) and $10^6$ cells were transduced in suspension overnight

with Cas9 lentivirus (pKLV2-EF1a-Cas9Bsd-W, Addgene #68343). Infected cells were then resuspended in Matrigel™ and cultured in the usual conditions. Regrown organoids were selected with 10 μg/ml blasticidin (Gibco).

*Mlh1* and *Msh2* sgRNAs compatible with Cas9 nuclease from *Streptococcus pyogenes* were designed using CHOPCHOP (https://chopchop.cbu.uib.no/). *Mlh1* sgRNA (GATTGACGTCCACGTTCTGA) and *Msh2* sgRNA (GCGGTCGAAGAGGCGCACCG) were cloned into lenti-sgRNA hygro (Addgene #104991) and lenti-sgRNA neo (Addgene #104992) vectors, respectively. Cas9-expressing BALB/c organoids were dissociated into single cells and $10^6$ cells were transduced with sgRNA lentivirus. Organoids regrown after infection underwent two cycles of selection with either 500 μg/mL hygromycin (Gibco) or 500 μg/mL G418 sulfate (Geneticin™, Gibco).


**Protein extraction and western blot analysis.**

Organoids for protein extraction were harvested and treated with Cell Recovery Solution (Corning) to allow Matrigel™ depolymerization and washout. Whole-protein extracts from both 3D and 2D cultures were prepared using Laemmli buffer and quantified using the BCA Protein Assay Kit (Pierce). The following primary antibodies were used: anti-MLH1 (Abcam, Ab92312), anti-MSH2 (Abcam, Ab70270), anti-MSH6 (Abcam, Ab92471), anti-Vimentin (Abcam, Ab92547), anti-E-Cadherin (BD Biosciences, 610182), anti-WRN (CST, 4666), anti-γH2AX S139 (Novus Biological, NB100-384PCP). Anti-βActin-HRP (Sigma, A3854) and anti-αTubulin (Abcam, Ab7291) were used as loading controls. Anti-mouse IgG HRP-linked and anti-rabbit IgG HRP-linked secondary antibodies were from Amersham.

**Genomic DNA extraction and quantification.**

Genomic DNA from WT and MMRd BALB/c organoids and cells was extracted using QIAamp DNA Mini Kit (Qiagen) and quantified using Qubit dsDNA BR Assay Kit (Invitrogen), following the manufacturer's instructions.

**Microsatellite instability analysis.**

Microsatellite instability in BALB/c mouse organoids was determined using a panel of five mouse noncoding mononucleotide markers as previously described (146).

DNA amplification was performed with the following labelled primers:

mBat64-fluorescein

(fw GCCCACACTCCTGAAAACAGTCAT, rv CCCTGGTGTGGCAACTTTAAGC),

AC096777-JOE

(fw TCCCTGTATAACCCTGGCTGACT, rv GCAACCAGTTGTCCTGGCGTGGA),

AA003063-Tamra

(fw ACGTCAAAAATCAATGTTAGG, rv CAGCAAGGGTCCCTGTCTTA),

U12235-JOE

(fw GCTCATCTTCGTTCCCTGTC, rv CATTCGGTGGAAAGCTCTGA),

L24372-fluorescein

(fw GGGAAGACTGCTTAGGGAAGA, rv ATTTGGCTTTCAAGCATCCATA).

The PCR reaction was performed in a total volume of 20 µL using 20 ng of genomic DNA and AmpliTaq Gold DNA Polymerase kit (Invitrogen). The cycling profile was as follows: 1 cycle at 94 °C for 4 min; 94 °C for 30 s, 56 °C for 45 s and 72 °C for 30 s for a total of 35 cycles. A final extension at 72 °C for 6 min completed the amplification. PCR fragments were separated

on a 3730 DNA analyser (Applied Biosystems) and raw data were analysed with GeneMarker software (Softgenetics).

**Whole exome sequencing.**

Whole exome sequencing was performed in outsourcing by Macrogen (Seoul, South Korea). The samples were prepared using Agilent SureSelect Mouse All Exon Kit and the libraries were sequenced with Illumina HiSeq 2000 sequencer. Data quality control and pre-processing were performed by Macrogen according to the following workflow:
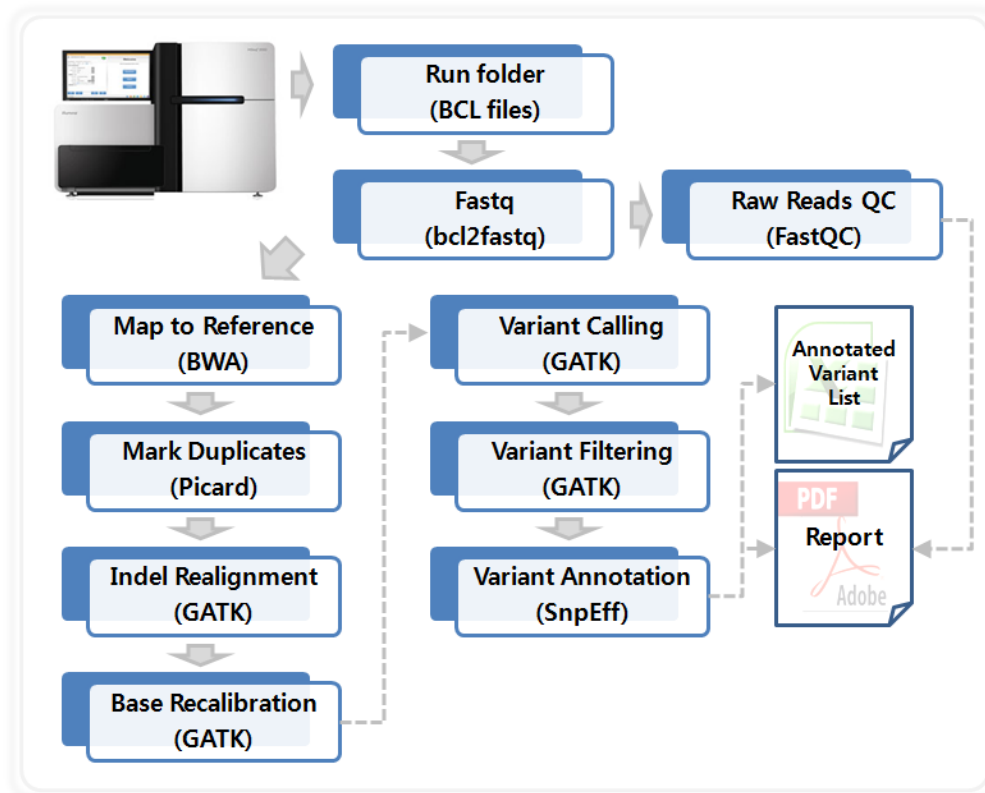


Mouse genome version mm10 from UCSC (original GRCm38 from NCBI, Dec. 2011) was used as mapping reference.

**Tumour mutational burden calculation and analysis of mutation types.**

DNA extracted from parental early-passage BALB/c gastric organoids underwent whole exome sequencing and was used as germline reference for the calling of somatic mutations. Tumour mutational burden was estimated based on whole exome sequencing data, either considering only coding non-synonymous somatic mutations with a minimum allele frequency of 0.1 or including all somatic mutations. The mutation count was then divided by the sequencing target region (49.370117 Mbp).

Filtered mutations were classified according to the following mutation types: insertions, deletions, and single-base substitutions. The count for each mutation type was divided by the total mutation count in each sample to assess the relative contribution. R base package was used for both mutation subsetting and counts. Plots were drawn using *ggplot2* package (145).

**X-irradiation conditions.**

Prior to irradiation, WT and MMRd BALB/c gastric organoids were dissociated to single cells using Trypsin-EDTA (Gibco). Cells were seeded in Matrigel™ in 24-well plates ($10^5$ cells in 15 µL Matrigel™/well) and overlayed with the usual culture medium.

Cells were irradiated by exposing them to X-rays at a dose rate of 1.5 Gy/minute using a Gilardoni RADGIL X-ray irradiator. The dose used at 3 months since the KO event was 0.5 Gy, administered in a unique radiation session. Between 9.5 and 10.5 months since the KO, organoids irradiated at 3 months underwent further irradiation sessions using a total dose of 2 Gy X-rays (dispensed once a week in 4 sessions, 0.5 Gy/session).

**Assessment of 2D cultures from BALB/c gastric organoids.**

BALB/c gastric organoids were dissociated to single cells using Trypsin-EDTA (Gibco). Cells were harvested in 15 mL tubes and centrifuged at 200 g for 5 minutes. The supernatant was discarded and the pellet was resuspended in culture medium. Tested media for 2D culture include in-house produced 50% L-WRN conditioned medium (141), DMEM medium (Gibco), ISCOVE medium (Gibco) and RPMI medium (Gibco). All media were supplemented with penicillin/streptomycin (Gibco), Glutamax (Gibco) and 10% Fetal Bovine Serum (Gibco). Cells were seeded at 50-60% confluency in 6-well plates. Cell series 3 was seeded in collagen-coated 6-well plates. The medium was refreshed twice a week.

**Preparation of cell suspensions for injection and *in vivo* tumorigenesis assays.**

The culture medium was refreshed the day before the injection. Before harvesting, Trypsin-EDTA (Gibco) was used for the dissociation of BALB/c organoids into single cells or for the detachment of organoid-derived cells growing in 2D-culture conditions (at approximately 80% confluence). Cells were collected in 15 mL tubes and counted. $5 \cdot 10^6$ cells/mouse were prepared in 200 μL of injection mixture (ice-cold culture medium + 20% Matrigel™). 8-week-old mice female NOD SCID mice and female BALB/c mice (Charles River Laboratories) were used for *in vivo* tumorigenicity studies. Cell suspensions were kept in ice and injected subcutaneously in the right flank of mice using 1 ml syringes, within 30 minutes from preparation. Mice were palpated at the injection site twice a week to observe nodule formation. As soon as tumours reached measurable size, tumour size was evaluated by calliper measurements and the approximate volume of the mass was calculated using the formula:

$$\frac{4\pi}{3} \cdot \frac{D}{2} \cdot \left(\frac{d}{2}\right)^2$$

where *d* indicates the minor tumour axis and *D* indicates the major tumour axis. Experiments were not performed in blind. Tumour growth curves and boxplots were plotted using *ggplot2* R package (145).

**Histology and immunohistochemistry.**

Tumour masses were explanted and a tissue portion was fixed with 10% neutral buffered formalin and paraffin-embedded. 3 μm sections were cut using a microtome and histology was investigated by haematoxylin and eosin staining. Immunohistochemical staining was performed using an anti-CD45 mouse-specific antibody (CST, 70257), according to the protocol recommended by the manufacturer. Images were captured using a Leica DM750 microscope.

**Crystal violet cell staining.**

Adherent cells were fixed with 11% glutaraldehyde solution for 20 minutes and then stained with 0.5% crystal violet solution (0.5 g crystal violet powder (Sigma-Aldrich), 80 mL distilled $H_2O$, 20 mL methanol).

**RNA extraction and quantification.**

RNA from WT and MMRd BALB/c organoids and cells was extracted using Maxwell® RSC miRNA tissue kit (Promega), following the manufacturer's instructions. and quantified using NanoDrop® ND-1000 UV-Vis Spectrophotometer.

**RNA sequencing.**

RNA sequencing was performed in outsourcing by Macrogen (Seoul, South Korea). Libraries were prepared using TruSeq Stranded Total RNA with Ribo-Zero Human/Mouse/Rat Gold kit (Illumina) and sequenced with Illumina HiSeq 2000 sequencer.

**Heatmap with epithelial–mesenchymal transition (EMT) markers.**

The analysis was performed from RNA sequencing row count data including 16 canonical EMT markers (CDH1, DSP, TJP1, EPCAM, GRHL2, VIM, CDH2, FOXC2, SNAI1, SNAI2, TWIST1, FN1, MMP2, MMP9, ZEB1, ZEB2). Mouse ortholog genes were identified using *biomaRt* R package (147). CPM values were calculated using *edgeR* R package (148). Heatmap was drawn using *heatmap.2()* function from *gplot* R package (149) plotting Z-scores calculated from $\log_2$CPM values.

**Differential gene expression analysis.**

Differential gene expression analysis was performed using *edgeR* and *limma* R packages (148,150). Starting from the RNA-sequencing raw count matrix, CPM values were calculated using *edgeR* package. A CPM of 1 was used as a cutoff to filter out lowly expressed genes. *EdgeR* package was also used to calculate factors for library size normalization across samples and *voom* normalization was applied to prepare data for linear modelling (151). Results from differential expression analysis were plotted in volcano plots using *ggplot2* and *ggrepel* R packages (145,152).

**GSEA.**

Data from differential gene expression analysis were used to rank the genes. Gene ranking was done by combining fold change values (LogFC) and t-statistics (*logFC * abs(t)*). The ranked gene list was used as input for GSEA, performed using *fgsea* R package (153). Hallmark and KEGG pathway gene sets were retrieved using *msigdbr* R package (154). GSEA bar plots were drawn using *ggplot2* (145).

**Comparative analysis of somatic mutations in cells retrieved from tumours.**

Pre-processed WES data in the form of Excel SNV files were imported into the R environment and used as input for the following analysis. Mutations were filtered to exclude germline mutations detected in parental BALB/c gastric organoids sequenced at an early passage. Area-proportional Euler diagrams depicting the extent of mutation sharing among the analysed cells were generated using *eulerr* R package (155). Plots were drawn considering all somatic mutations or considering only somatic mutations with high and intermediate functional impact (frameshifts, truncating and missense variants).

**Analysis of alterations in genes correlated to MSI subgroup according to TCGA.**

The list of genes significantly mutated in the MSI subgroup according to TCGA analysis was derived from (43). Correspondent mouse ortholog genes were identified using *biomaRt* R package (140). Whole exome sequencing data, derived from MMR deficient cells retrieved from tumours, were filtered to consider only somatic alterations with allele frequency equal to or greater than 0.2 and high/moderate predicted impact (coding frameshift variants, inframe indels, splice and missense mutations). Mutation data were represented in oncoprints drawn using ComplexHeatmap R package (135). Frameshifts and stop mutations were represented

using the same label ("trunc mutation"), as usually done in representations from the *cBioPortal* platform (https://www.cbioportal.org/).

**Real-time PCR for Cas9-expression.**

Before real-time PCR, reverse transcription was performed starting from 500 ng of RNA per sample and using High-Capacity cDNA Reverse Transcription Kit (Applied Biosystems) according to the manufacturer's instructions. Quantitative PCR experiments for assessment of Cas9 expression were performed in technical triplicates using SsoAdvanced Universal SYBR Green Supermix (Bio-Rad) and the following primers:

Cas9 (fw GAAAGTTCGACAATCTGACCAAGG, rv TGCCACGTGCTTTGTGATCTG),

Mouse-Actin (fw TTGCTGACAGGATGCAGAAG, rv CTGCTTGCTGATCCACATCT).

PCR runs were performed with ABI Prism 7900HT (Applied Biosystems).

**Mlh1 and Msh2 knockout in BALB/c mouse gastric organoids using CRISPR/Cas9 system with transient Cas9 expression.**

To generate cells expressing sgRNAs, BALB/c gastric organoids were dissociated into single cells using Trypsin-EDTA (Gibco) and $10^6$ cells were transduced in suspension overnight with sgRNA lentiviruses (as described above). Infected cells were then resuspended in Matrigel™ and cultured in the usual conditions. Regrown organoids were selected for 72 hours with either 500 μg/mL hygromycin (Gibco) or 500 μg/mL G418 sulfate (Geneticin™, Gibco). Selected organoids were then dissociated into single cells and $10^5$ cells were transfected in suspension overnight for the introduction of the Cas9 plasmid DNA (pKLV2-EF1a-Cas9Bsd-W, Addgene #68343) using Lipofectamine™ 2000 Transfection Reagent (Invitrogen). Transfected cells were then resuspended in Matrigel™, cultured in the usual conditions and selected with 10

μg/ml blasticidin (Gibco) 48 hours after transfection. Regrown organoids were again dissociated and single cells were clones in 96-well plates for generation of clones.

**RNA interference-based Wrn sensitivity assay.**

Approximately $1\text{-}1.5\cdot10^3$ cells/well were reverse-transfected in a 96-well plate in technical quintuplicate with ON-TARGETplus siRNAs to a final concentration of 20 nM. RNAiMAX (Invitrogen) was used as transfection reagent following the manufacturer's instructions. Each experiment included a non-transfected control, transfection reagent only as mock control, a non-targeting pool as negative control (Dharmacon, D-001810–10–20), mouse polo-like kinase 1 (*Plk1*) pool as positive control (Dharmacon, L-040566-00-0020), and the targeting pool against *Wrn* (Dharmacon, L-058494-01-0020). Cells were grown for 6 days and cell viability was assessed using the CellTiter-Glo 2.0 Assay (Promega).

**Genome editing-based Wrn sensitivity assay.**

Cas9-expressing cells were generated transducing overnight $10^6$ cells with Cas9 lentivirus (pKLV2-EF1a-Cas9Bsd-W, Addgene #68343). Infected cells underwent two cycles of selection with 10 μg/ml blasticidin (Gibco). Approximately $2\text{-}2.5\cdot10^4$ cells/well were then seeded in 6-well plates and transduced with sgRNAs lentiviruses. Each experiment included a sgRNA targeting a mouse non-essential negative control (*Cyp4f40*), a sgRNA targeting mouse polo-like kinase 1 (*Plk1*) pool as positive control and a sgRNA targeting mouse *Wrn*. sgRNA sequences were designed using CHOPCHOP (https://chopchop.cbu.uib.no/) and Benchling (https://www.benchling.com/) as follows:

Cyp4f40 (GCGACGTCGCTCCTGGATGA),

Plk1 (GCAGCCGGCGGCAGTATGTA),

Wrn (GCCAGACCAGAAGTGCACCG).

Cells were selected with 500 μg/mL hygromycin (Gibco) 48 hours after infection and were grown for 7 days. Cells were then stained using crystal violet.

## Contributions to this project.

| | Candidate | Working group | Internal facilities | External collaborators | Outsourcing |
|---|---|---|---|---|---|
| Explant of stomachs for organoid generation | - | 100% | - | - | - |
| Organoid derivation | 100% | - | - | - | - |
| Organoid and cell culture | 90% | 10% | - | - | - |
| Organoid and cell characterization (imaging, immunofluorescence, western blot) | 100% | - | - | - | - |
| Knockout of MMR genes with stable Cas9 expression | - | - | - | 100% | - |
| Knockout of MMR genes with transient Cas9 expression | 100% | - | - | - | - |
| Single-cell cloning and clone characterization (western blot, real time) | 90% | - | 10% | - | - |
| X-irradiation | 80% | - | 20% | - | - |
| Assessment of 2D cultures | 100% | - | - | - | - |
| Sampling (DNA, RNA and protein extraction and quantification) | 90% | 10% | - | - | - |
| Microsatellite instability analysis | 60% | 40% | - | - | - |
| Preparation of cell suspensions for injection in mice | 90% | 10% | - | - | - |
| Cell injection in mice, palpation and measurement of tumour volume | 10% | 90% | - | - | - |
| Histology and immunohistochemistry | 60% | 40% | - | - | - |
| Sequencing and data pre-processing | - | - | - | - | 100% |
| Post-processing bioinformatic analyses | 100% | - | - | - | - |
| Wrn sensitivity assays | 50% | - | - | 50% | - |
| Experimental design | 70% | 20% | - | 10% | - |
| Data analysis and graphics | 100% | - | - | - | - |

## RESULTS

**Establishment and characterization of non-transformed BALB/c mouse gastric organoids.**

Obtaining cultures of gastric epithelial non-transformed cells was the essential starting point for generating an *ex vivo* model mimicking MSI gastric cancer tumorigenesis. To generate gastric cultures, we explanted stomachs from immunocompetent BALB/c mice and dissociated gastric epithelium to isolate gastric glands, similarly to what was previously done by (140,156). The first attempts done following the methods found in the literature resulted in a low gland yield. We thus pooled together epithelial fragments from three mice and made some adjustments in the isolation protocol in order to obtain a proper number of single gastric glands (3000-5000 units). Glands were seeded in Matrigel™ in three-dimensional (3D) conditions with appropriate medium to allow self-renewal of the stem cell compartment and long-term expansion. After 10 days, some glands ballooned up and formed sparse large 3D structures (Figure 6A). Organoids from the initial plate were enzymatically dissociated into smaller cell clumps, re-seeded and allowed to regrow. After passage, BALB/c gastric organoids reformed effectively in a few days and showed the typical spherical and hollow morphology of non-transformed 3D gastric cultures (140,156). Furthermore, to assess their long-living potential, organoids were subjected to freeze-thaw cycles and cultured for several months: after every manipulation they were able to reform 3D structures and did not show any evident morphological alteration over time (Figure 6B).

We characterized BALB/c gastric organoids analysing their cellular composition. In both human and murine gastric mucosa, stem cells reside at the gland base and/or in the isthmus region and produce progenitors that are actively proliferating and giving rise to the differentiated cell lineages (157). In the mouse stomach, several stem cell markers have been

proposed (158–162). Among them, Wnt target genes − such as Lgr5, Troy and Axin2 − played a key role in the identification of cells with self-renew capacities. Lgr5 is a well-known marker of mitotically active homeostatic stem cells in the gastrointestinal tract. Its expression in mouse gastric glands is high at the gland base and gradually decreases going up to the pit (162). Lineage tracing studies revealed that Lgr5-expressing cells are responsible for the long-term renewal of the gastric epithelium and a single Lgr5^{+} cell can efficiently generate long-living gastric organoids *in vitro* (156,158). Furthermore, Lgr5^{+} chief cells have been proposed as gastric cancer-initiating cells (163). We analysed Lgr5 expression in organoids via whole-mount immunofluorescence staining and found widespread positivity. In accordance, we observed that a significant cell fraction is actively proliferating in the organoids, as indicated by the diffuse expression of Ki67 in cell nuclei. We also assessed the expression of two markers of differentiated gastric cell lineages: Muc5ac, a marker for pit mucous cells, and Pgc, a marker for chief cells (Figure 6C). The observed positivity for the markers under analysis indicates that our cultures effectively capture the main cell populations present in the normal gastric mucosa.

**Figure 6.**
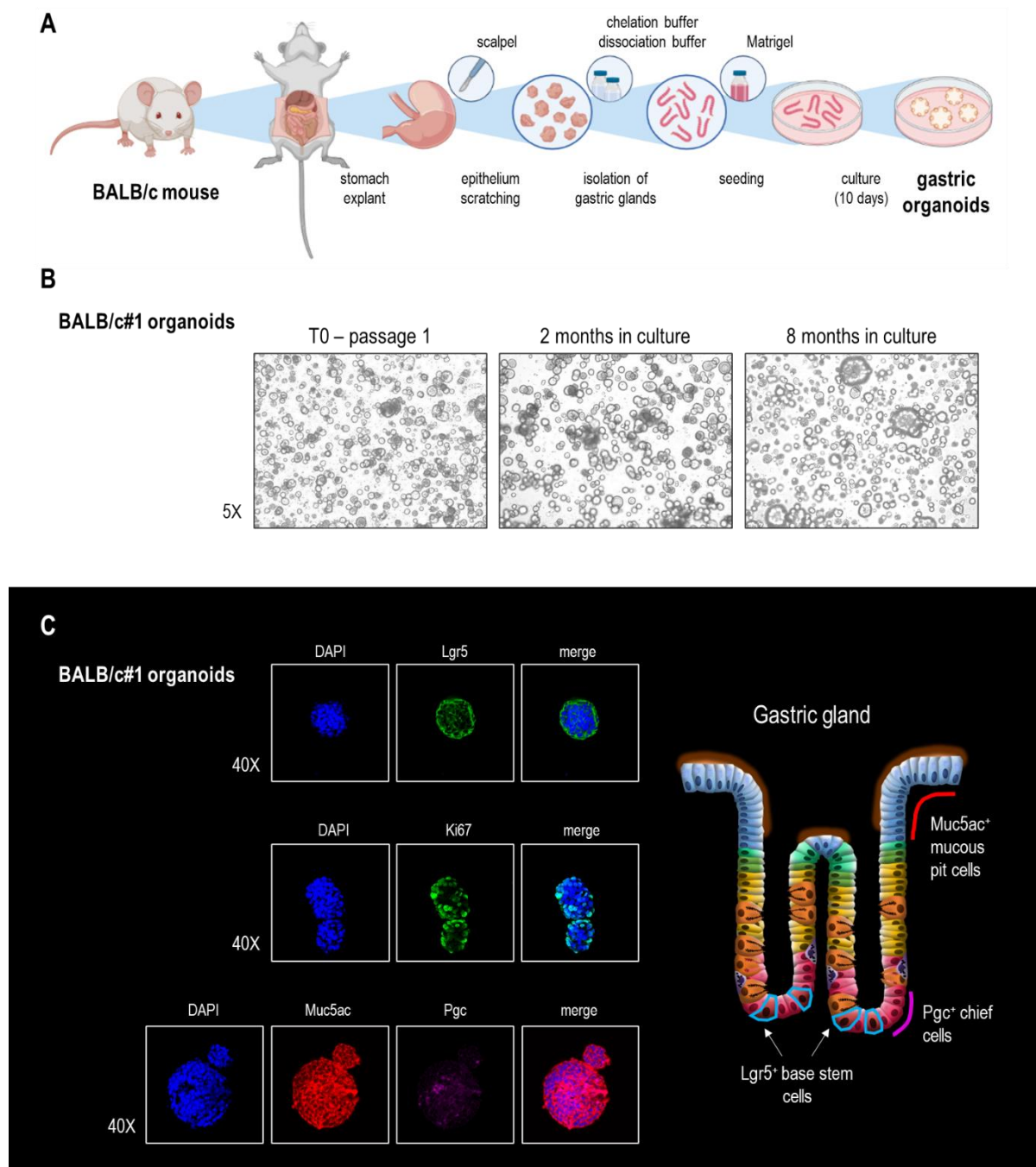


*Figure 6. **Generation and characterization of BALB/c#1 organoids**. **A**. Schematic representation of the protocol used to isolate gastric glands from the normal gastric epithelium of BALB/c mice. Created using BioRender.com. **B**. Phase-contrast images of BALB/c#1 organoids at time 0 (T0), 2 and 8 months of continuous culture. **C**. Whole-mount immunofluorescent staining of BALB/c#1 organoids with anti-Lgr5 (green), anti-Ki67 (green), anti-mucin 5ac (Muc5ac, red) and anti-pepsinogen (Pgc, far red) antibodies.*

**MMR impairment in BALB/c mouse gastric organoids.**

Lynch syndrome is a genetic disorder associated with germline mutations in MMR genes (*MLH1, MSH2, MSH6,* and *PMS2*) and alterations in the *EPCAM* gene, affecting the function of the nearby *MSH2* gene. MMR deficiency in Lynch syndrome patients can cause MSI, predisposing to different cancer types, including colorectal, endometrial, ovary, gastric and small intestinal cancers (50). However, the vast majority of MSI cancers are not inherited and arise mainly through sporadic *MLH1* promoter hypermethylation, completely silencing *MLH1* gene expression. *MLH1* epigenetic silencing and MSI were detected in colorectal adenomas, endometrial hyperplasia, dysplasia and intestinal metaplasia of gastric mucosa (164–166). Increased cancer risk in Lynch Syndrome patients together with MSI detection in a variety of sporadic cancers, including pre-cancerous lesions, suggest that MSI could be an early molecular event during carcinogenesis, significantly contributing to the acquisition of malignant cell phenotype and cancer progression.

In line with these findings, to evaluate spontaneous cell transformation we planned to impair MMR system function in BALB/c gastric organoids, without inducing any concomitant alteration in known oncogenes or tumour suppressor genes.

We analysed the occurrence of main MMR gene alterations in MSI-high tumours from two independent cohorts, our GEA platform of patient-derived xenografts (117) and the gastric carcinoma TCGA dataset (43). Only potentially loss-of-function alterations in MutL (*MLH1, MLH3, PMS1, PMS2*) and MutS genes (*MSH2, MSH3, MSH6*) such as homozygous deletion, truncating and splicing mutations and low gene expression, were included in the analysis. As expected, *MLH1* was the most altered gene (78% of cases), with the vast majority of MSI-high tumours displaying low *MLH1* gene expression. Protein-truncating mutations in *MSH3* and *MSH6* genes were common as well (Figure 7A). We performed statistical pairwise tests for

detecting co-occurrences and mutual exclusivities in MMR loss-of-function alterations in the same datasets. Only two gene pairs (*MLH1-MSH2* and *MLH1-MLH3*) showed a significant tendency to mutual exclusivity (Figure 7B). Consistently, when we calculated Pearson correlation, the same gene pairs displayed a trend to negative correlation, with the *MLH1-MSH2* pair being the best hit even if the p-value did not reach the threshold of 0.05 (p-value = 0.075) (Figure 7C). However, a very significant mutual exclusivity emerged when we grouped together the alterations affecting genes which are part of the same MMR complex (either MutL or MutS) (Figure 7D). These results suggest that the dysfunction of a single complex is sufficient to establish a state of MMR deficiency leading to MSI, while the simultaneous loss of both complexes may not confer a significant advantage during the neoplastic transformation process.

**Figure 7.**
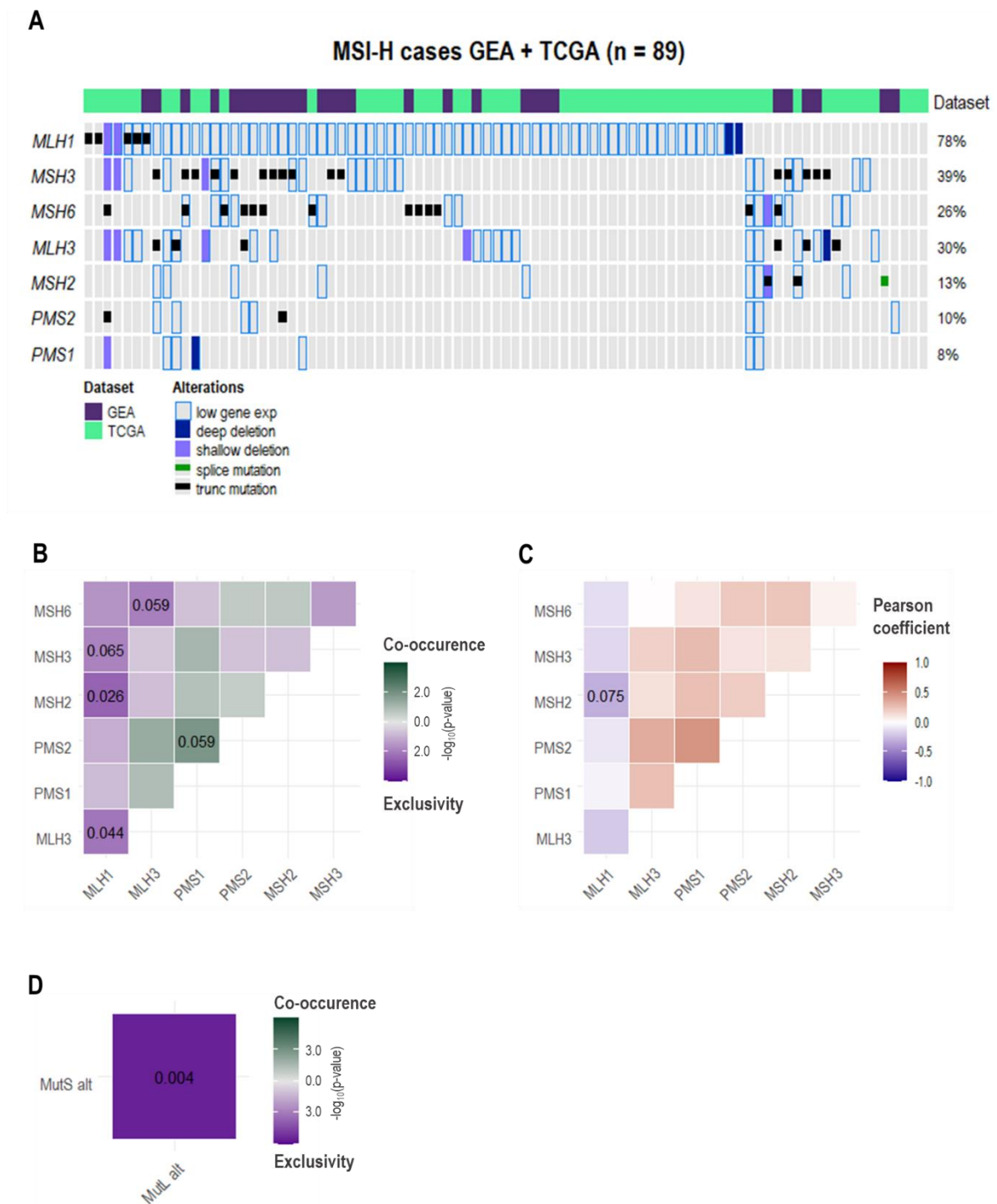




*Figure 7. **Analysis of loss-of-function alterations in the main MMR genes in GEA and TCGA GC datasets. A.*** *Oncoprint visualisation of 89 MSI-high gastric cancer cases from the GEA PDX platform* (117) *and the TCGA cohort* (43)*. The chart displays the putative loss-of-function alterations (low gene expression, gene deletions, splicing, truncating mutations and frameshifts) in the MMR genes forming MutL and MutS complexes. The annotation refers to the dataset of origin. Deep deletion = homozygous deletion; shallow deletion = heterozygous deletion.* **B.** *Triangle heatmap from co-occurrence/mutual exclusivity analysis for alterations in the main MMR*

*genes. Numbers in the plot indicate the p-values which were significant (p-value < 0.05) or close to significance according to the Poisson binomial test. C. Triangle heatmap from Pearson correlation. The number in the plot indicates the p-value for the only pair which was close to significance. D. Plot depicting results from co-occurrence/mutual exclusivity analysis performed comparing alterations occurring in MutL and MutS complexes. The number in the plot indicates the p-value according to the Poisson binomial test.*

In order to obtain a good representation of the MMR deficiency landscape in MSI gastric cancer − in collaboration with Dr Gabriele Picco (Wellcome Sanger Institute, Hinxton, UK) − we used CRISPR/Cas9-based genome editing to knock down either Mlh1 or Msh2 proteins in BALB/c gastric organoids, thus completely impairing function of MutL or MutS complexes, respectively (Figure 8A). Briefly, organoids were dissociated to single cells and infected overnight in suspension with lentivirus for Cas9 expression. Once reseeded in Matrigel™ and regrown, organoids were then infected with lentiviruses for sgRNA expression following the same protocol. After two cycles of antibiotic selection, bulk edited organoids resulted in a complete knockout (KO) of the target gene. Given the high efficacy of the genome editing step, we did not subject these organoids to single-cell cloning procedures. We primarily employed these bulk lines to prove the tumorigenic potential resulting from the inactivation of *Mlh1* and *Msh2* genes. Both wild type (WT) and MMR-deficient (MMRd) organoids were then kept continuously in culture for over a year without any further antibiotic selection. We checked periodically the KO profile via Western Blot and we never observed any reappearance of non-edited cell populations (Figure 8B). Furthermore, we did not notice any significant morphological change in MMRd cultures compared to their WT counterpart (Figure 8C).
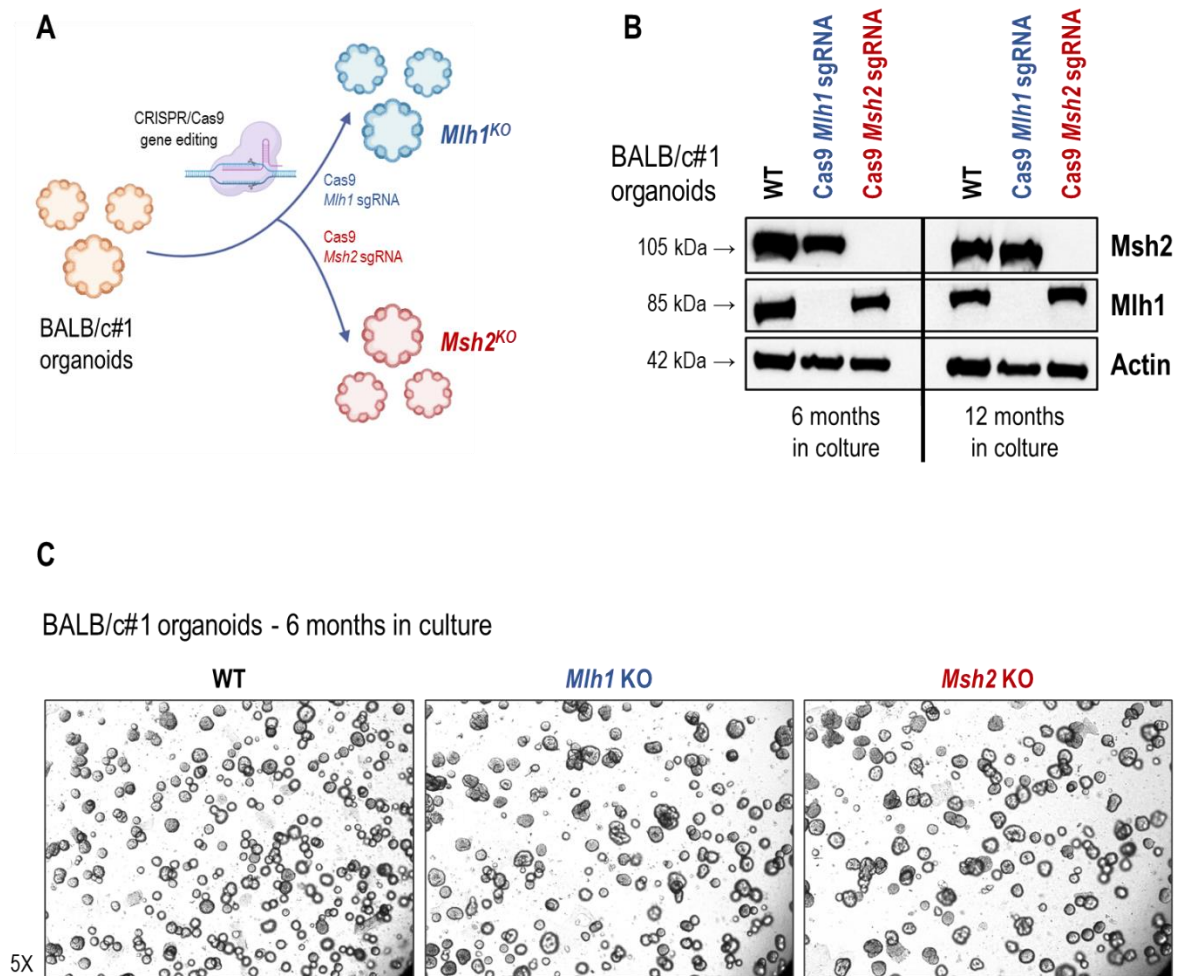
**Figure 8.**



Figure 8. ***Derivation of MMR-deficient BALB/c#1 organoids. A.*** *Schematic representation of the CRISPR/Cas9-based genome editing procedure followed to obtain Mlh1 KO and Msh2 KO cultures. Organoids underwent subsequent transductions with Cas9 and sgRNA lentiviruses. Created using BioRender.com.* ***B.*** *Western blot analysis of Mlh1 and Msh2 proteins in WT and CRISPR/Cas9-edited BALB/c#1 organoids. Actin was used as loading control.* ***C.*** *Phase-contrast images of WT and CRISPR/Cas9-edited (MMR-deficient) BALB/c#1 organoids at 6 months of continuous culture from the knockout event.*

**MMR-deficient but not wild type BALB/c mouse gastric organoids show key MSI features.**

Both MMR-deficient and WT organoids were banked at several time points and genomic DNA was extracted for the assessment of key known features of MSI tumours, such as the microsatellites status and the tumour mutational burden (TMB). For microsatellite instability analysis, 5 independent mouse mononucleotide repeat markers were amplified by fluorescent multiplex PCR and evaluated by capillary electrophoresis. In this analysis, MSI-high status definition requires the shift of at least 2 out of 5 loci in comparison to the matched normal DNA. Thus, using DNA from parental early-passage BALB/c organoids as normal control, we observed that – after 3.5-6 months of culture – MMRd, but not WT organoids, developed microsatellite instability (Figure 9A shows electropherogram traces for the shifted loci).

We performed whole exome sequencing (WES) from DNA aliquots derived from both WT and MMRd organoids at early and late time points since the KO event (3.5 and 10 months). Based on WES data, we calculated TMB by considering the number of non-synonymous single-nucleotide variants and indels per mega-base of the sequencing target genome (as generally done for the assessment of the mutational load in solid tumours (167)). DNA extracted from parental early-passage BALB/c gastric organoids was used as germline reference for the calling of somatic mutations. Consistent with the status of microsatellites, only MMRd organoids increased their TMB over time. Interestingly, at 10 months of culture, *Msh2* KO organoids showed a higher TMB compared to *Mlh1* KO organoids (62.8 versus 37.2 mut/Mb) (Figure 9B).

In the context of MSI, errors often accumulate mostly as indels as a consequence of ineffective repair of double-strand breaks (168). To verify the presence of such a mutation signature in our models, we further analysed WES data to assess the mutational landscape associated with each

genotype. As done for TMB calculation, we first considered only non-synonymous somatic mutations and classified them according to the mutation types. However, we observed no extensive changes in the relative contribution of each mutation type across samples. At both early and late time points, all genotypes showed a large prevalence of single-base substitutions (SBS) over insertions and deletions and the *Msh2* KO model further increased the SBS portion over time (67% to 80%) (Figure 9C).

Considering this unexpected result, we repeated both the TMB evaluation and the analysis of relative mutation type contribution including all somatic alterations. In the case of TMB, we confirmed the trend of the previous evaluation, with *Msh2* KO organoids presenting the highest mutational load (Figure 9D). When we reanalysed the relative mutation type contribution, the indel portions were wider compared to what we observed in the previous analysis. In particular, only *Mlh1* KO organoids maintained indels over 50% of all alterations at both time points, while *Msh2* KO organoids showed again a relative increase of single-base substitutions (47% to 66%) over time and a consequent prevalence of SBS at 10 months since the KO event (Figure 9E).

# Figure 9.
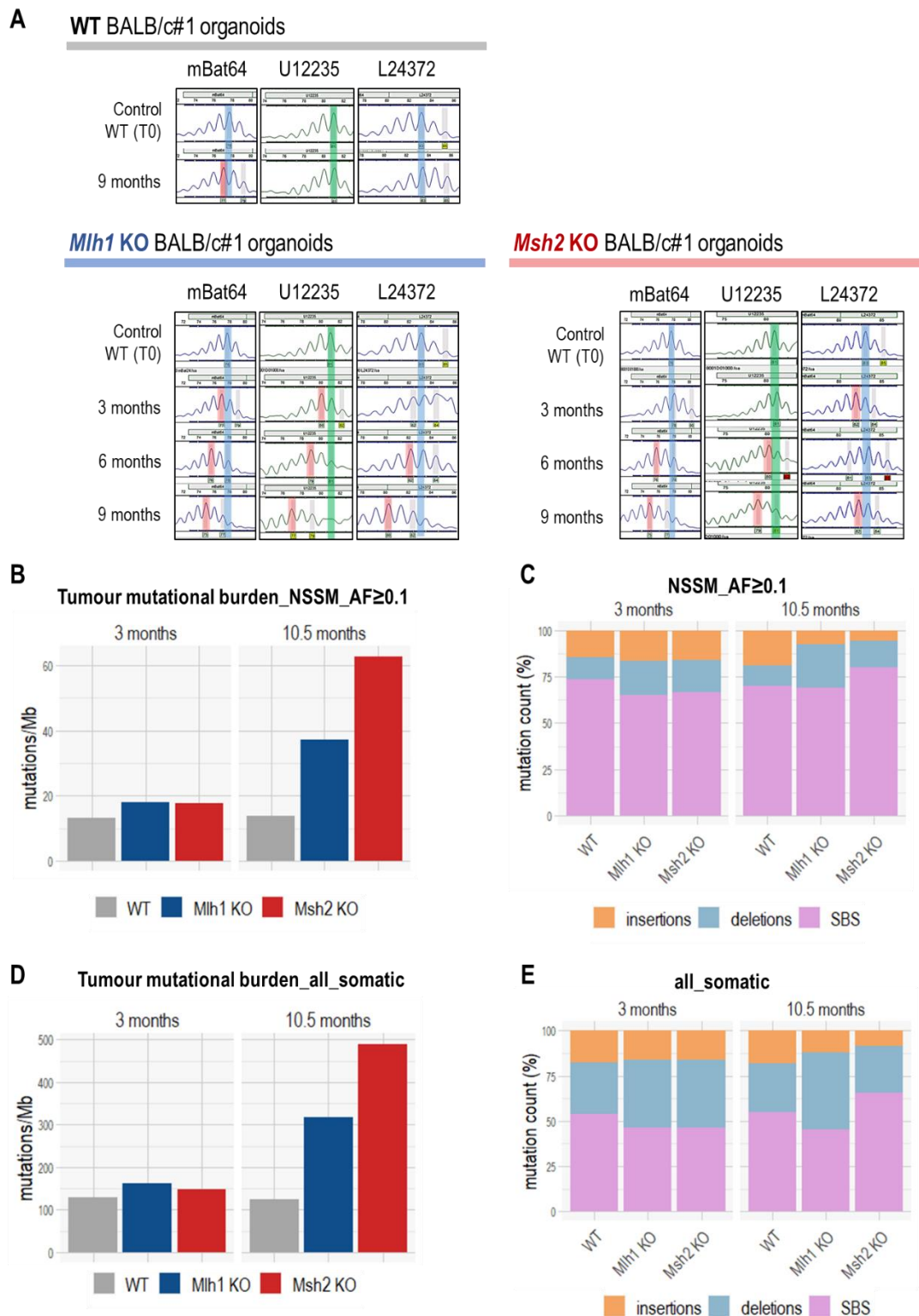


*Figure 9. **Evaluation of the microsatellite status and the mutational load in WT and MMRd BALB/c#1 organoids**. A. STR analysis for the assessment of the microsatellite status in MMRd BALB/c#1 gastric organoids at 3, 6 and 9 months of continuous culture since the knockout event. Electropherograms show the PCR products*

*for the loci (3 out of 5) in which we observed shifted profiles. **B.** Histogram depicting tumour mutational burden in WT and MMRd BALB/c#1 organoids, at 3 and 10.5 months of continuous culture since the knockout event, calculated as non-synonymous somatic mutations per megabase of whole exome sequencing target genome. **C.** Stacked histogram depicting the relative mutation type contribution for non-synonymous somatic mutations in WT and MMRd BALB/c#1 organoids at 3 and 10.5 months of continuous culture since the knockout event. **D.** Histogram depicting tumour mutational burden in WT and MMRd BALB/c#1 organoids, at 3 and 10.5 months of continuous culture since the knockout event, calculated as all somatic mutations per megabase of whole exome sequencing target genome. **E.** Stacked histogram depicting the relative mutation type contribution for all somatic mutations in WT and MMRd BALB/c#1 organoids at 3 and 10.5 months of continuous culture since the knockout event. NSSM = non-synonymous somatic mutations; SBS = single base substitutions; T0 = time zero (early-passage parental organoids).*

## BALB/c mouse gastric organoids are not tumorigenic upon subcutaneous injection in NOD SCID mice.

In order to evaluate their tumorigenic potential, we performed *in vivo* tumorigenicity assays by injecting both WT and MMRd BALB/c organoids into immunocompromised NOD SCID mice. We performed the experiment at three different time points: 3.5, 6 and 12 months of continuous culture since the KO event. Organoids were dissociated and $5 \cdot 10^6$ cells/mouse were injected subcutaneously in the right flank. Three mice were injected for each experimental arm and periodically palpated for over 8 months. In the first 4 months after injection, we did not observe any palpable tumour mass either in WT or in MMRd groups. Afterwards, some tumour masses emerged together with distress for the involved mice (Figure 10A and B). However, haematoxylin-eosin staining performed on tumour slides revealed the presence of small-sized cells with large round nuclei, indicating lymphomas spontaneously arose in ageing mice (Figure 10C).

**Figure 10.**

## A

BALB/c#1 organoids
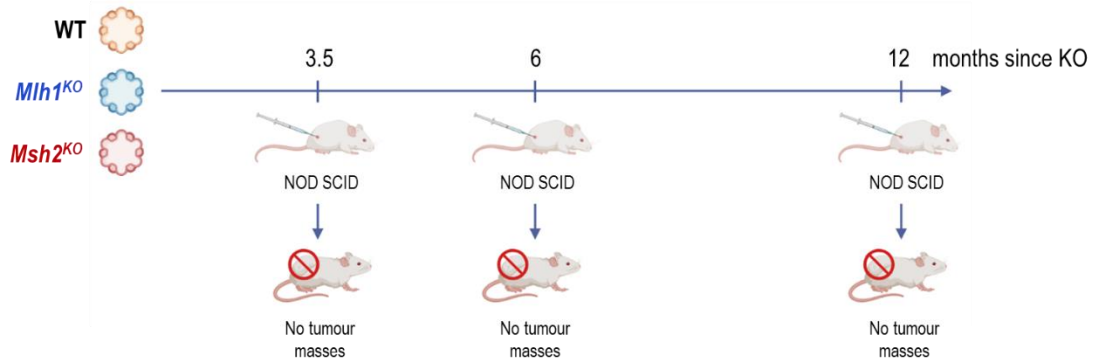
WT  
Mlh1KO  
Msh2KO

3.5 — 6 — 12 months since KO

NOD SCID — No tumour masses (×3)

## B

Injection timepoint

| 3.5 months | Days after injection | 28 | 40 | 47 | 61 | 127 | Endpoint |
|---|---|---|---|---|---|---|---|
| | WT mouse#1 | 16 | 7 | Not palpable | Not palpable | Not palpable | sacrificed at day 147 (no mass) |
| | WT mouse#2 | 16 | 4 | Not palpable | Not palpable | Not palpable | sacrificed at day 263 (no mass) |
| | WT mouse#3 | 6 | 2 | Not palpable | Not palpable | Not palpable | sacrificed at day 263 (no mass) |
| | Mlh1 KO mouse #1 | 17 | 7 | 14 | Not palpable | Not palpable | sacrificed at day 249 (no mass) |
| | Mlh1 KO mouse #2 | 28 | 7 | 4 | Not palpable | Not palpable | sacrificed at day 263 (no mass) |
| | Mlh1 KO mouse #3 | 19 | 12 | 4 | Not palpable | Not palpable | sacrificed at day 166 (no mass) |
| | Msh2 KO mouse #1 | Not palpable | Not palpable | 4 | Not palpable | Not palpable | sacrificed at day 263 (no mass) |
| | Msh2 KO mouse #2 | 33 | 14 | Not palpable | Not palpable | Not palpable | sacrificed at day 263 (no mass) |
| | Msh2 KO mouse #3 | 7 | 2 | 4 | Not palpable | Not palpable | sacrificed at day 258 (no mass) |

*volume (mm³)*

| 6 months | Days after injection | 21 | 37 | 44 | 52 | 141 | Endpoint |
|---|---|---|---|---|---|---|---|
| | WT mouse#1 | 4 | 4 | 4 | Not palpable | Not palpable | sacrificed at day 269 (no mass) |
| | WT mouse#2 | Not palpable | Not palpable | Not palpable | Not palpable | Not palpable | sacrificed at day 269 (no mass) |
| | WT mouse#3 | Not palpable | Not palpable | Not palpable | Not palpable | Not palpable | sacrificed at day 226 (no mass) |
| | Mlh1 KO mouse #1 | Not palpable | Not palpable | Not palpable | Not palpable | 10 | explanted at day 226 (small subcutis mass) |
| | Mlh1 KO mouse #2 | Not palpable | NA | NA | NA | NA | sacrificed at day 30 (no mass) |
| | Mlh1 KO mouse #3 | Not palpable | Not palpable | Not palpable | Not palpable | Not palpable | sacrificed at day 246 (no mass) |
| | Msh2 KO mouse #1 | Not palpable | Not palpable | 4 | Not palpable | Not palpable | explanted at day 226 (small subcutis mass) |
| | Msh2 KO mouse #2 | 4 | Not palpable | Not palpable | Not palpable | Not palpable | sacrificed at day 226 (no mass) |
| | Msh2 KO mouse #3 | Not palpable | 4 | Not palpable | Not palpable | Not palpable | sacrificed at day 269 (no mass) |

*volume (mm³)*

| 12 months | Days after injection | 21 | 37 | 44 | 52 | 141 | Endpoint |
|---|---|---|---|---|---|---|---|
| | WT mouse#1 | 4 | 4 | 4 | 4 | Not palpable | sacrificed at day 169 (no mass) |
| | WT mouse#2 | Not palpable | Not palpable | Not palpable | Not palpable | Not palpable | sacrificed at day 269 (no mass) |
| | WT mouse#3 | Not palpable | Not palpable | Not palpable | Not palpable | 50 | explanted at day 141 (small subcutis mass) |
| | Mlh1 KO mouse #1 | Not palpable | 4 | Not palpable | Not palpable | NA | sacrificed at day 78 (no mass) |
| | Mlh1 KO mouse #2 | Not palpable | Not palpable | Not palpable | Not palpable | Not palpable | sacrificed at day 269 (no mass) |
| | Mlh1 KO mouse #3 | 4 | 4 | 4 | Not palpable | Not palpable | sacrificed at day 269 (no mass) |
| | Msh2 KO mouse #1 | 4 | 4 | Not palpable | Not palpable | Not palpable | sacrificed at day 147 (no mass) |
| | Msh2 KO mouse #2 | 10 | Not palpable | 4 | Not palpable | NA | sacrificed at day 71 (no mass) |
| | Msh2 KO mouse #3 | 4 | Not palpable | Not palpable | Not palpable | Not palpable | sacrificed at day 269 (no mass) |

*volume (mm³)*

## C

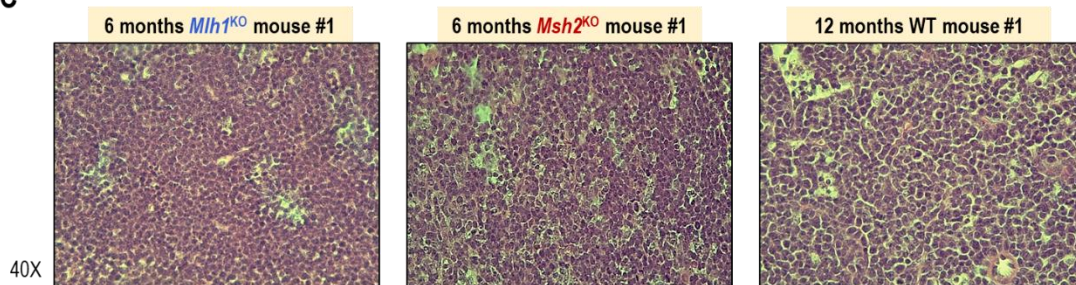6 months Mlh1KO mouse #1 | 6 months Msh2KO mouse #1 | 12 months WT mouse #1

40X

*Figure 10. **Assessment of tumorigenicity of WT and MMRd BALB/c#1 gastric organoids upon subcutaneous injection in NOD SCID mice. A.** Schematic representation of the injection time points and the results from the tumorigenicity assays. Created using BioRender.com. **B.** Table with history of tumour volume measurements and endpoints for all mice. **C.** Haematoxylin and eosin staining of late tumour masses arisen in ageing mice.*

*In vivo* assays suggested that, although MMRd organoids acquired microsatellite instability and a high mutational load, they did not harbour sufficient driver alterations to undergo malignant transformation. We considered other strategies to speed up the transformation process introducing further random mutations, without transducing cells to introduce any specific driver alteration. It is known from the literature that pre-neoplastic cells are more susceptible to radiation-induced transformation processes compared to healthy cells from the same tissue. Moreover, a relatively low radiation dose (0.5 Gy of ionizing radiations) was sufficient to enhance anchorage-independent growth capacity in partially transformed breast primary epithelial cells at 4 and 8 weeks post-irradiation (169). We thus exposed both WT and MMRd organoids to ionizing radiation. At 3 months since the KO event, organoids were dissociated into single cells and reseeded in usual 3D culture conditions just before the radiation procedure. The radiation dose of 0.5 Gy of X-rays was delivered in a single exposure using a blood irradiator, in collaboration with the radiologists of our institute (Figure 11A). Radiation did not seem to affect organoid regrowth: eight days post-irradiation all irradiated cells effectively regenerated organoids as efficiently as their non-irradiated counterparts (Figure 11B). We previously optimised irradiation doses on parental WT organoids and higher tested doses (1 Gy, 2 Gy and 5 Gy) affected cell growth in the short term (6 days) (data not shown).

**Figure 11.**
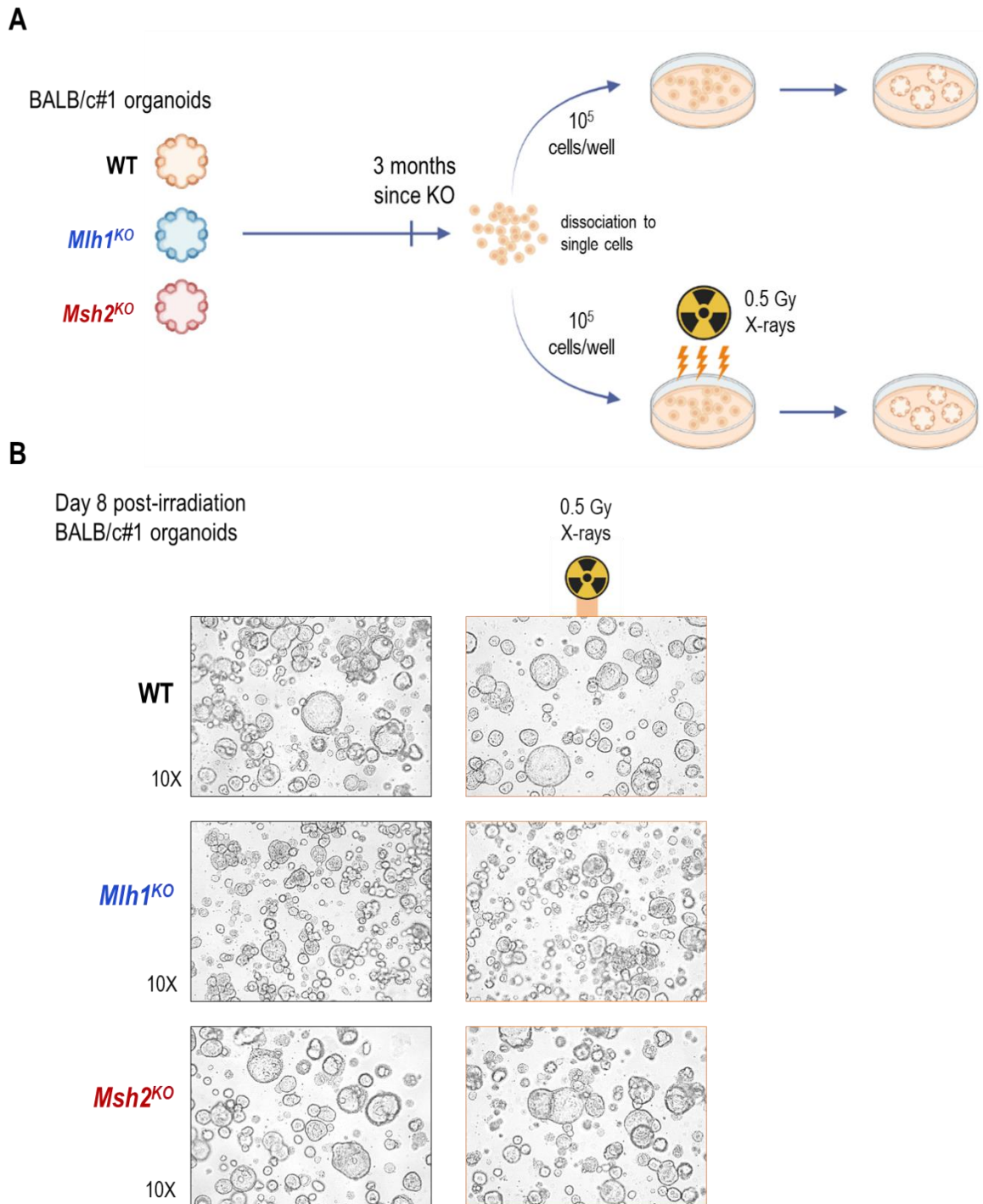


*Figure 11. **X-ray irradiation of WT and MMRd gastric organoids. A.** Schematic representation of the irradiation procedure. Created using BioRender.com. **B.** Phase-contrast images of WT and MMRd BALB/c#1 gastric organoids, exposed or not to X-rays, at day 8 post-irradiation.*

We then repeated *in vivo* tumorigenicity assays, injecting into NOD SCID mice irradiated WT and MMRd organoids at 2 time points: 2 weeks and 2 months post-irradiation (corresponding to 3.5 and 6 months of global continuous culture since the KO event, respectively). However, as in the previous experiments, organoids generated no tumour masses and only some late sporadic lymphomas emerged (Figure 12A, B and C). We then further exposed organoids to ionizing radiations. Between 9.5 and 10.5 months since the KO event, pre-irradiated organoids were subjected to new radiation sessions: 0.5 Gy of X-rays were dispensed once a week for 4 weeks (with a total administered radiation dose of 2 Gy). At 12 months, we repeated once again the in vivo tumorigenicity assay but, unfortunately, we did not succeed in generating any MSI tumour mass (Figure 12A and B). We confirmed the non-epithelial nature of the tumour masses that emerged during the tumorigenesis experiments by performing immunohistochemical staining with an antibody that specifically recognizes the murine CD45, used as a marker of leukocytes. Figure 12D shows the staining performed on a representative slice.

**Figure 12.**



**A.** BALB/c#1 organoids — WT, Mlh1KO, Msh2KO; timeline of months since KO (3.5, 6, 9.5, 10.5, 12) with irradiation and NOD SCID injection time points; "No tumour masses" at each. IONIZING RADIATION (X-rays): 0.5 Gy single exposure; 0.5 Gy once a week for 4 weeks.
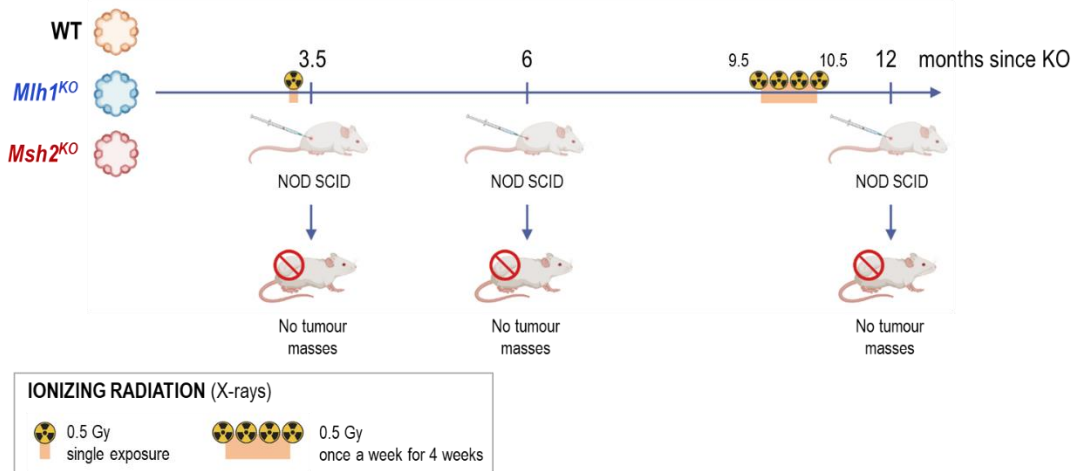
**B.** Injection timepoint

**3.5 months**

| Days after injection | 28 | 40 | 47 | 61 | 127 | Endpoint |
|---|---|---|---|---|---|---|
| WT mouse#1 | 26 | 5 | Not palbable | Not palbable | Not palbable | sacrificed at day 263 (no mass) |
| WT mouse#2 | 14 | 6 | Not palbable | Not palbable | Not palbable | sacrificed at day 228 (no mass) |
| WT mouse#3 | 21 | 11 | Not palbable | Not palbable | Not palbable | sacrificed at day 263 (no mass) |
| Mlh1 KO mouse #1 | 26 | Not palbable | 4 | Not palbable | Not palbable | sacrificed at day 263 (no mass) |
| Mlh1 KO mouse #2 | 28 | 21 | 4 | Not palbable | Not palbable | sacrificed at day 263 (no mass) |
| Mlh1 KO mouse #3 | 11 | 4 | Not palbable | Not palbable | Not palbable | sacrificed at day 263 (no mass) |
| Msh2 KO mouse #1 | 20 | 15 | Not palbable | Not palbable | Not palbable | sacrificed at day 263 (no mass) |
| Msh2 KO mouse #2 | 38 | 25 | Not palbable | Not palbable | Not palbable | sacrificed at day 130 (no mass) |
| Msh2 KO mouse #3 | Not palbable | Not palbable | Not palbable | 4 | Not palbable | sacrificed at day 193 (no mass) |

(volume ($mm^3$))

**6 months**

| Days after injection | 21 | 37 | 44 | 52 | 141 | Endpoint |
|---|---|---|---|---|---|---|
| WT mouse#1 | Not palbable | Not palbable | Not palbable | Not palbable | Not palbable | sacrificed at day 169 (no mass) |
| WT mouse#2 | Not palbable | Not palbable | Not palbable | Not palbable | Not palbable | sacrificed at day 269 (no mass) |
| WT mouse#3 | 4 | Not palbable | Not palbable | Not palbable | Not palbable | sacrificed at day 269 (no mass) |
| Mlh1 KO mouse #1 | Not palbable | Not palbable | Not palbable | Not palbable | Not palbable | sacrificed at day 212 (no mass) |
| Mlh1 KO mouse #2 | Not palbable | Not palbable | Not palbable | Not palbable | Not palbable | explanted at day 176 (bilateral subcutis masses) |
| Mlh1 KO mouse #3 | Not palbable | Not palbable | Not palbable | Not palbable | NA | sacrificed at day 64 (no mass) |
| Msh2 KO mouse #1 | Not palbable | 4 | 4 | Not palbable | Not palbable | explanted at day 269 (small subcutis mass) |
| Msh2 KO mouse #2 | 4 | 4 | 4 | Not palbable | NA | sacrificed at day 115 (no mass) |
| Msh2 KO mouse #3 | 4 | 4 | Not palbable | Not palbable | 75 | sacrificed at day 160 (no material explanted) |

(volume ($mm^3$))

**12 months**

| Days after injection | 21 | 37 | 44 | 52 | 141 | Endpoint |
|---|---|---|---|---|---|---|
| WT mouse#1 | Not palbable | Not palbable | Not palbable | Not palbable | NA | sacrificed at day 128 (no mass) |
| WT mouse#2 | 4 | 4 | 4 | Not palbable | Not palbable | sacrificed at day 259 (no mass) |
| WT mouse#3 | Not palbable | Not palbable | Not palbable | Not palbable | NA | sacrificed at day 128 (no mass) |
| Mlh1 KO mouse #1 | 4 | 4 | 4 | Not palbable | 51 | sacrificed at day 253 (no mass) |
| Mlh1 KO mouse #2 | 4 | 4 | 4 | Not palbable | NA | sacrificed at day 106 (no mass) |
| Mlh1 KO mouse #3 | Not palbable | Not palbable | Not palbable | Not palbable | Not palbable | sacrificed at day 205 (no mass) |
| Msh2 KO mouse #1 | 4 | 4 | 4 | Not palbable | Not palbable | sacrificed at day 269 (no mass) |
| Msh2 KO mouse #2 | 4 | 4 | 4 | Not palbable | Not palbable | sacrificed at day 269 (no mass) |
| Msh2 KO mouse #3 | 4 | 4 | 4 | Not palbable | Not palbable | sacrificed at day 269 (no mass) |

(volume ($mm^3$))

**C.** 6 months Mlh1KO mouse #2 — 40X; 6 months Msh2KO mouse #1 — 40X

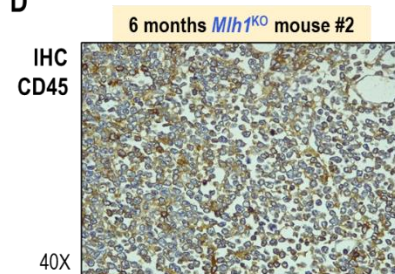**D.** 6 months Mlh1KO mouse #2 — IHC CD45 — 40X
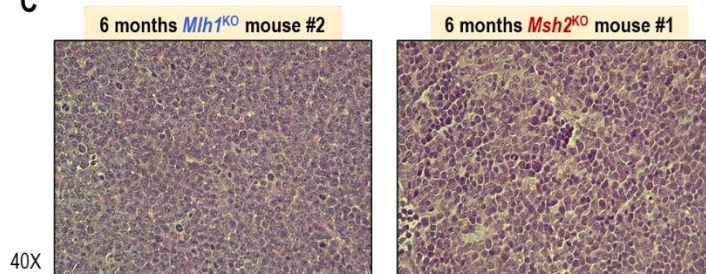
*Figure 12. **Assessment of tumorigenicity of irradiated WT and MMRd BALB/c#1 gastric organoids upon subcutaneous injection in NOD SCID mice. A.** Schematic representation of the irradiation and injection time points and the results from the tumorigenicity assays. Created using BioRender.com. **B.** Table with history of*

*tumour volume measurements and endpoints for all mice. **C.** Haematoxylin and eosin staining of late tumour masses arisen in ageing mice. **D.** Immunohistochemical mouse specific CD45 staining of a representative late tumour mass arisen in ageing mice. IHC = immunohistochemistry.*

**Assessment of BALB/c mouse gastric organoid-derived 2D cultures.**

Phenotypic plasticity disrupting cellular differentiation was recently proposed as a new cancer hallmark. Terminal cell differentiation implies, in most cases, an antiproliferative phenotype and constitutes a barrier against tumorigenesis (170).

The culture medium we use for normal organoids includes several factors maintaining a homeostatic balance between self-renewal and differentiation of the stem cell compartment. Given the results from *in vivo* experiments described in the previous paragraph, we thought that – due to the medium formulation and the presence of a steady basal membrane matrix – 3D-culture conditions may not represent a selective microenvironment able to drive MMRd gastric cells towards a complete neoplastic transformation.

In order to induce a potential cell reprogramming, we subjected cells to more selective culture settings. Both WT and MMRd organoids – exposed or not to ionizing radiations at 3 months since KO – were dissociated to single cells and seeded in conventional 2D conditions. All cell populations were able to adhere and form a monolayer when fetal bovine serum (FBS) was added to the culture medium, independently of the specific medium composition. Conversely, long-term cell survival and proliferation were affected by the culture medium chosen for 2D culture initiation, by the time point of derivation and by the following culture handling. We generated 3 independent cell series changing the derivation timing, testing different culture media and – in the case of series 3 – trying also to stimulate cell growth with extra detachment-attachment cycles in collagen-coated plates.

Cell series 1 represents the first attempt at 2D culture and was derived from BALB/c organoids at 3.5 months since the KO event. Single cells obtained from organoid dissociation were resuspended, seeded at 50-60% confluency and cultured in 50% L-WRN conditioned medium (141), ISCOVE medium, DMEM medium or RPMI medium, supplemented with 10% FBS. Both WT and MMRd cells underwent a long latency period (6-8 weeks) in which they did not proliferate but survived in adhesion. After that, few viable cells remained in culture, but they did not survive detachment procedures. Cells derived from *Msh2* KO irradiated organoids and cultured in 50% L-WRN medium were the only exception: 7 weeks since organoid dissociation and seeding, they began to proliferate and were successfully expanded. After some passages, we were able to culture *Msh2* KO cells in RPMI medium without affecting their proliferation (Figure 13). RPMI medium represents a way to further select cells, as 3 key factors for gastric organoid culture are still present in 50% L-WRN conditioned medium (Wnt3a, R-spondin and Noggin), while none of them is included in RPMI medium.

**Figure 13.**
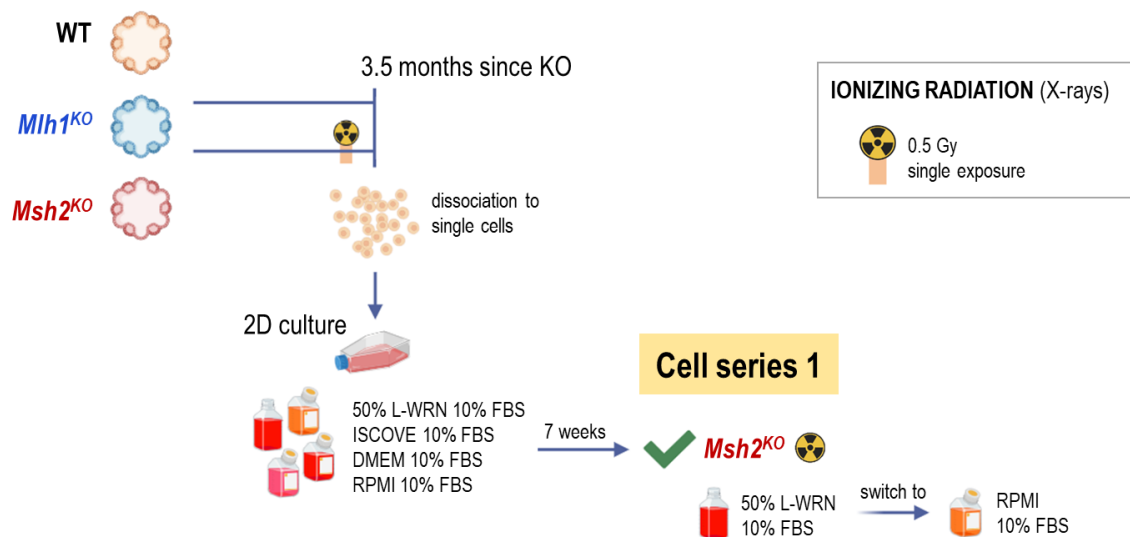


*Figure 13. **Schematic representation of the derivation conditions and protocol used to generate cell series 1.** The green tick indicates the case in which we were able to obtain a stably growing 2D culture. FBS = fetal bovine serum. Created using BioRender.com.*

66

Cell series 2 was derived from BALB/c organoids at 8 months since the KO event. In this case, cells derived from organoid dissociation were cultured in either 50% L-WRN conditioned medium or RPMI medium, supplemented with 10% FBS. Four weeks since the seeding, all *Mlh1 KO* cells, as well as *Msh2* KO cells derived from irradiated organoids, were actively proliferating in both 50% L-WRN and RPMI media. After a longer latency (8 weeks), also WT cells derived from irradiated organoids and cultured in 50% L-WRN medium started to grow. However, we did not manage to obtain stable 2D cultures from WT and *Msh2* KO cells derived from the dissociation of non-irradiated organoids (Figure 14).

**Figure 14.**
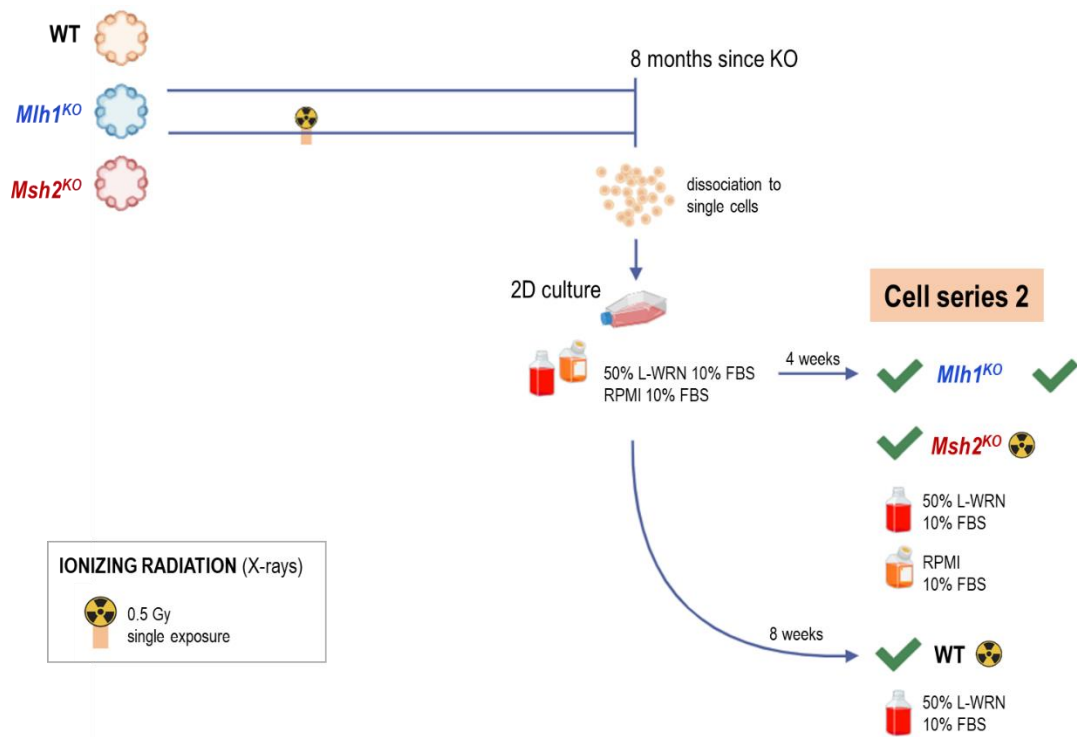


*Figure 14.* ***Schematic representation of the derivation conditions and protocol used to generate cell series 2.*** *The green ticks indicate the cases in which we were able to obtain stably growing 2D cultures. FBS = fetal bovine serum. Created using BioRender.com.*

In order to obtain a complete cell set including both WT and MMRd cells derived from both irradiated and not-irradiated organoids, we did a third attempt of derivation, dissociating organoids at an intermediate time point (6 months since the KO event). Cells from series 3 were seeded in collagen-coated plates and cultured in 50% L-WRN conditioned medium supplemented with 10% FBS. After one week from seeding, all cells were detached and reseeded in collagen-coated plates. *Mlh1* KO cells, from both irradiated and not irradiated organoids, began to actively proliferate after 3-4 weeks and were successfully expanded. At 6-7 weeks since derivation, we managed to achieve the same result with *Msh2* KO cells. Over 10 weeks have been necessary to observe the proliferation of WT cells derived from irradiated organoids. For all growing cell populations, we were able to switch the culture medium to RPMI and keep expanding cells for banking in non-coated plates. Interestingly, in over 10 weeks, we did not observe any active proliferation of WT cells derived from non-irradiated organoids and cultured in 50% L-WRN medium supplemented with 10% FBS. However, when we reintroduced the complete organoid medium supplemented with 10% FBS, we obtained a growing cell population (Figure 15A and B).

Overall, these observations suggest that the effectiveness of 2D culture is enhanced by a gradual shift from the nutrient-rich medium used for organoid growth to a poorer one. A sudden transition may lead to an amplified bottleneck effect, depriving the cell population of adequate time to adapt and endure the altered culture conditions.

**Figure 15.**
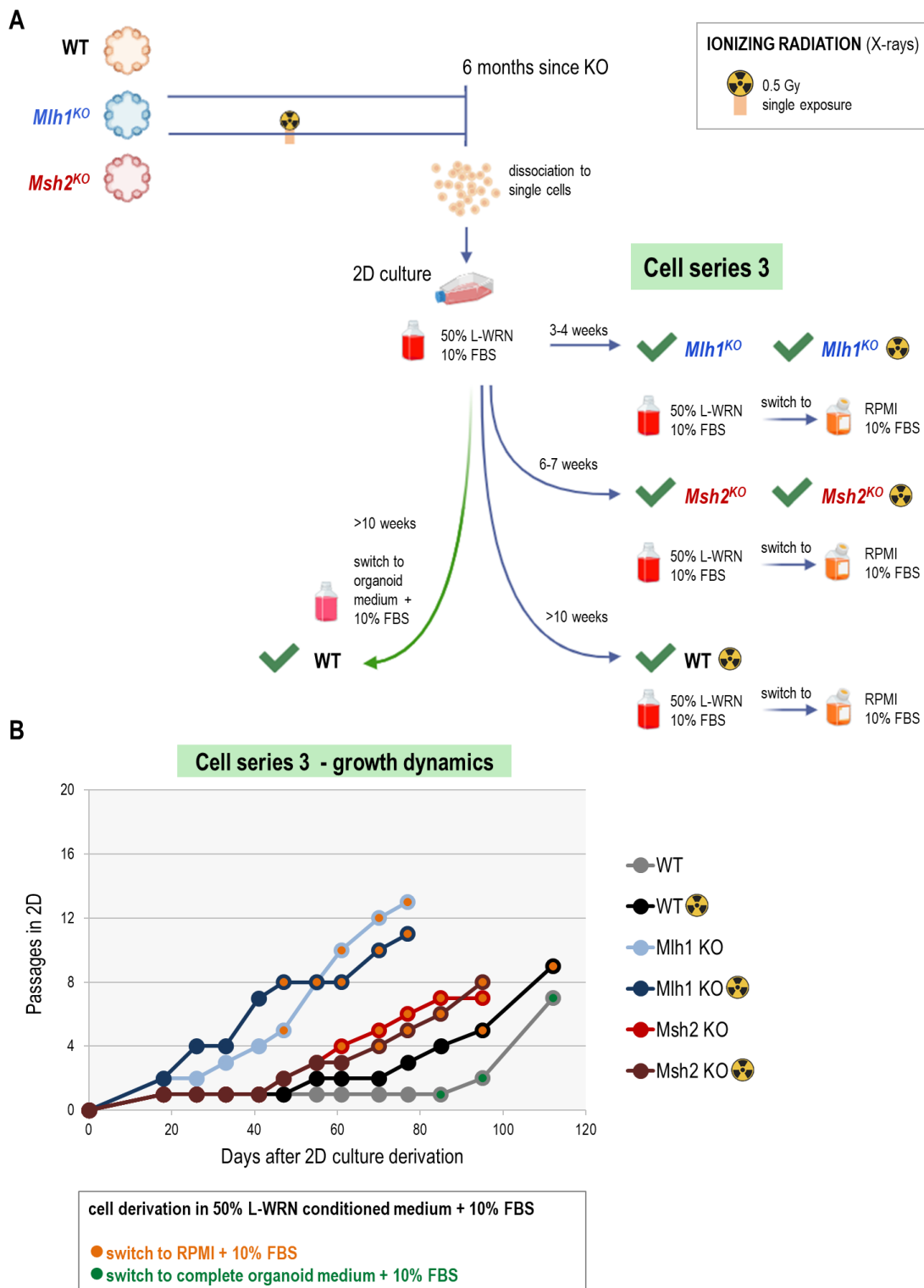


*Figure 15. **Generation of cell series 3. A.** Schematic representation of the derivation conditions and protocol used to generate 2D cultures. The green ticks indicate the cases in which we were able to obtain stably growing 2D cultures. Created using BioRender.com. **B.** Growth dynamics of 2D cultures from series 3. The plot starting point*

**MMR-deficient, but not WT, BALB/c organoid-derived 2D-cultures form tumour masses upon subcutaneous injection in NOD SCID mice.**

We performed *in vivo* tumorigenicity assays injecting all cell series derived from BALB/c organoids into immunocompromised NOD SCID mice.

*Msh2* KO cells from cell series 1 have been injected twice (Figure 16A). In the first experiment, performed at 7 months of overall culture since the KO event, 3 out of 4 mice developed a tumour mass. After a latency period of over 70 days, tumours became measurable and started to grow fast and invade the mouse leg close to the injection point. Mice were sacrificed due to paralysis in the right leg and, for this reason, tumour masses were explanted at relatively small volumes ($\leq 500$ mm$^3$). The same cells were injected again subcutaneously in NOD SCID mice at 10 months of overall culture since the KO event. This time, all mice developed tumour masses which became measurable in 20-40 days. However, as in the previous experiment, cells invaded the nearby leg and mice were sacrificed prematurely (Figure 16B). During explant procedures, we collected specimens for further analyses from all mice (formalin-fixed paraffin-embedded tissue samples, RNAlater preserved tissues and OCT frozen tissues). Figure 16C-H shows the characterisation of mouse #1 from the first experiment. Histological analysis revealed an undifferentiated tissue (Figure 16D). In order to verify the tumour origin, we re-derived cells from the tissue and cultured them in 2D conditions. Western blot analysis confirmed that the cells retrieved from mouse #1 tumour were KO for the *Msh2* gene as well as the injected cells and the organoids from which they derive. As expected, the loss of Msh2 protein implied the concomitant downregulation of Msh6 (its partner in the MutSα complex) (Figure 16E). Consistently with their invasive phenotype, we noticed changes in the

morphology of the cells. Before being injected, cells in culture showed two mixed populations: isles of polygonal epithelial cells grew surrounded by cells with a fibroblast-like morphology. Interestingly, after the *in vivo* passage, the elongated morphology was positively selected (Figure 16F). To explore the possibility of an epithelial-to-mesenchymal transition, we checked via Western Blot the expression of E-cadherin and Vimentin, used as key epithelial and mesenchymal markers, respectively. E-cadherin was clearly downregulated only after the *in vivo* passage, while Vimentin was already expressed *in vitro* in 2D culture and was further upregulated in cells retrieved from the tumour (Figure 16G). Moreover, starting from RNA sequencing data, we confirmed the downregulation of E-cadherin together with other canonical epithelial markers (Epcam, Dsp, Tjp1, Grhl2) and the concomitant upregulation of Vimentin and other canonical mesenchymal markers (N-cadherin, Twist1, Zeb1/2, Fibronectin 1, Metalloproteinases and Snail) (Figure 16H).

**Figure 16.**
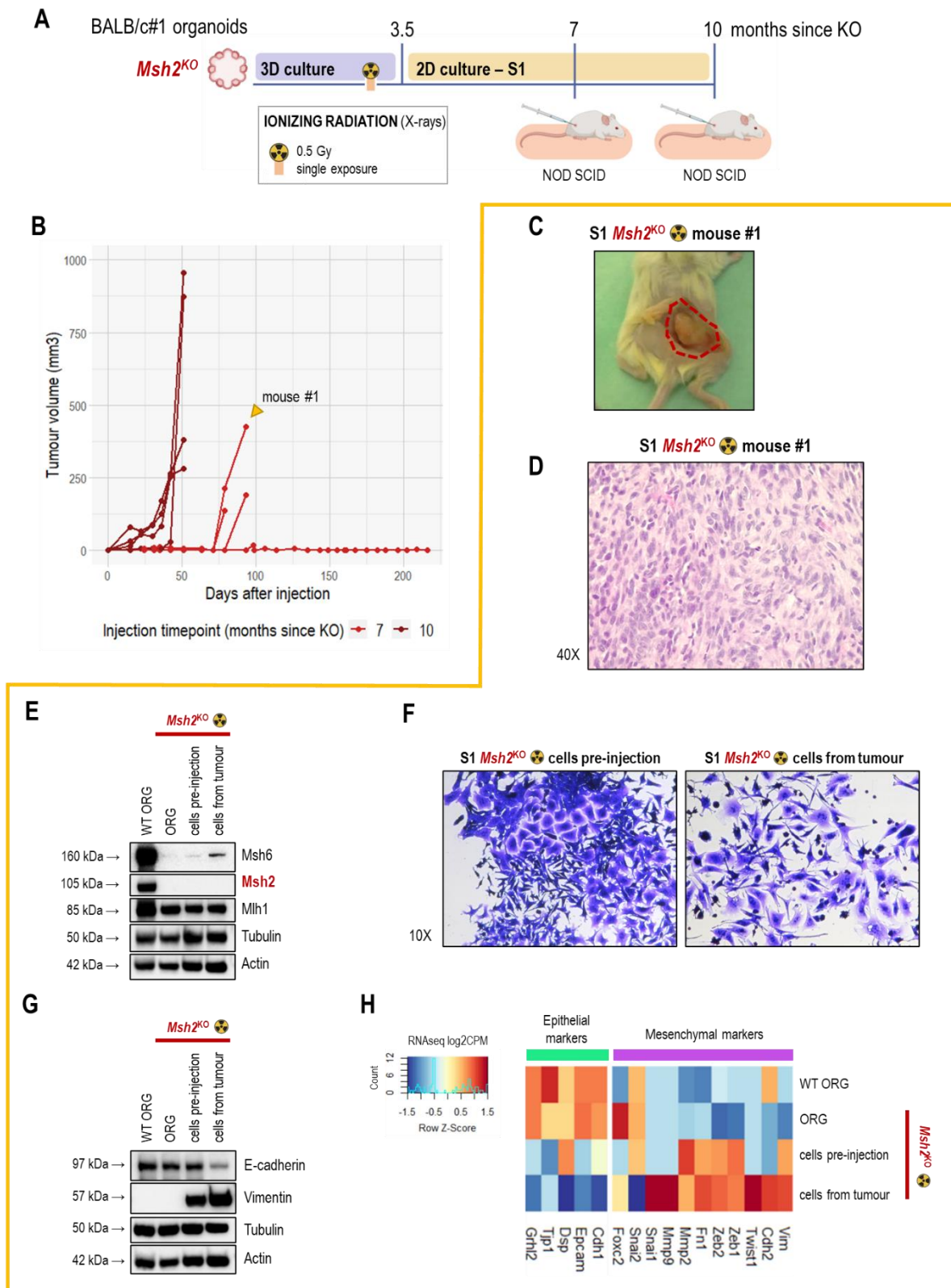


*Figure 16. **Assessment of tumorigenicity of series 1 Msh2 KO organoid-derived cells upon subcutaneous injection in NOD SCID mice. A.** Schematic representation of the cell culture phases and the injection time points. Created using BioRender.com. **B.** In vivo growth curves upon cell injection at 7 and 10 months of global culture*

*since the knockout event. Each line corresponds to a single mouse. The tumour mass obtained from the mouse indicated by the yellow arrow (mouse #1) was used for subsequent post-in vivo analyses. Panels C-H are related to mouse #1 characterization. **C.** Image of the tumour mass at the explant site. **D.** Haematoxylin and eosin staining of the tumour mass. **E.** Western blot analysis of Mlh1, Msh2 and Msh6 proteins in WT BALB/c#1 organoids, Msh2 KO organoids and organoid-derived cells from series 1, at pre-injection time point and retrieved from the tumour mass. Actin and tubulin were used as loading controls. **F.** Crystal violet staining on Msh2 KO organoid-derived cells from series 1, at pre-injection time point and retrieved from the tumour mass. **G.** Western blot analysis of E-cadherin and vimentin proteins in WT BALB/c#1 organoids, Msh2 KO organoids and organoid-derived cells from series 1, at pre-injection time point and retrieved from the tumour mass. Actin and tubulin were used as loading controls. **H.** Heatmap depicting the expression of canonical epithelial and mesenchymal markers based on Z-score normalized RNA sequencing data. CPM = counts per million; ORG = organoids; S1 = cell series 1.*

*Mlh1* KO cells from series 2 derived from not-irradiated organoids were injected as well. The experiment was performed at 10 months of overall culture since the KO event (8 months of 3D culture followed by 2 months of 2D culture) (Figure 17A) and, as in the case of *Msh2* KO cells from series 1 injected at 10 months, all NOD SCID mice showed measurable tumour masses in 20-40 days. As masses were growing, mice developed at first skin abrasions at the injection site and then ulcerating tumours. Thus, mice were explanted without reaching high tumour volumes ($\leq 1000$ mm$^3$) (Figure 17B). We checked histology via haematoxylin-eosin staining in tumour masses from mice #1 and #4. They both displayed an epithelial morphology with epithelial cell isles surrounded by evident portions of stromal tissue. However, mouse #1 showed two populations of epithelial cells: one population constituted by smaller cells with a relatively small cytoplasm and another one formed by big cells with an enlarged cytoplasm and a granular nucleus with prominent nucleoli. Interestingly, mouse #4 displayed only the latter cell population (Figure 17C).
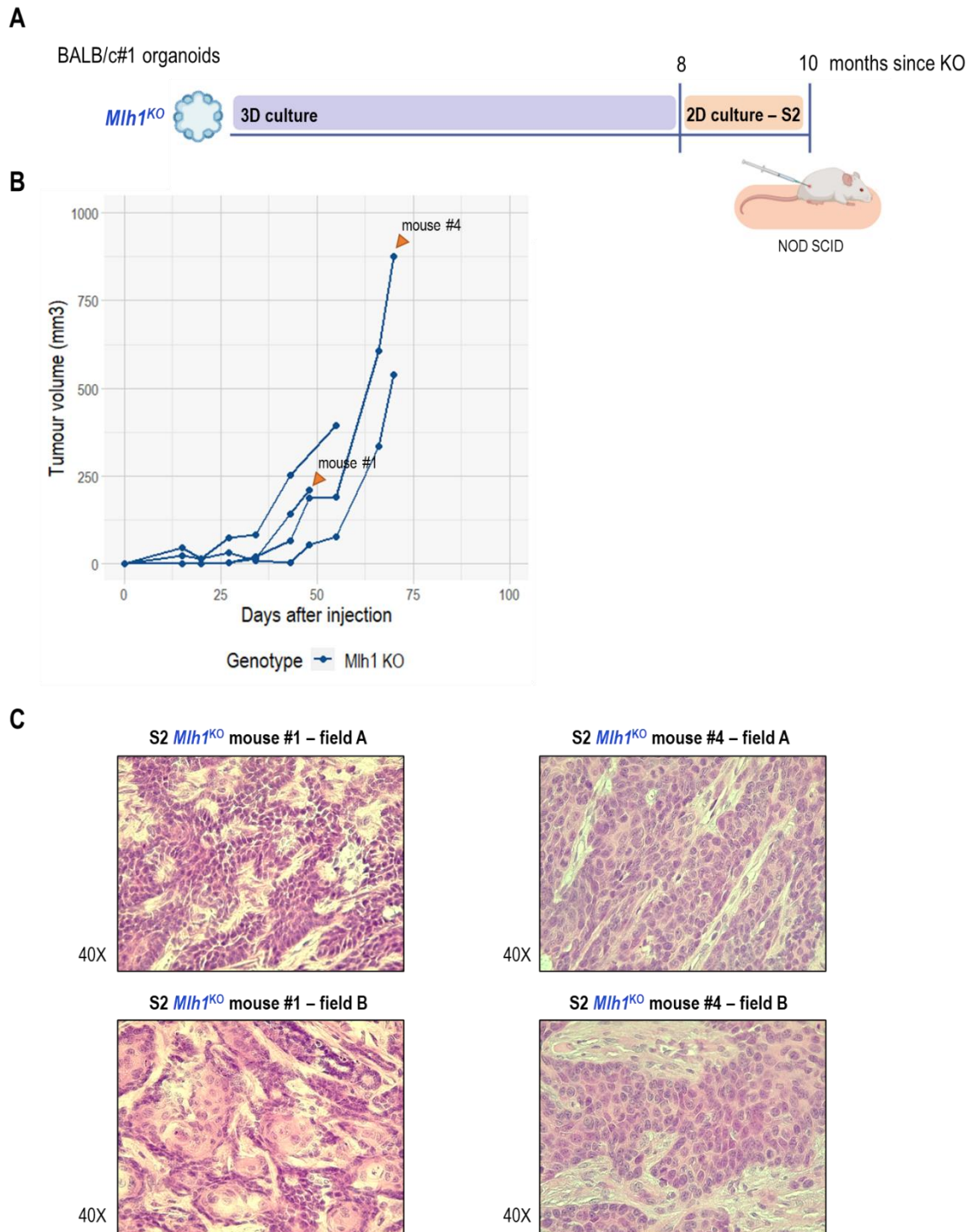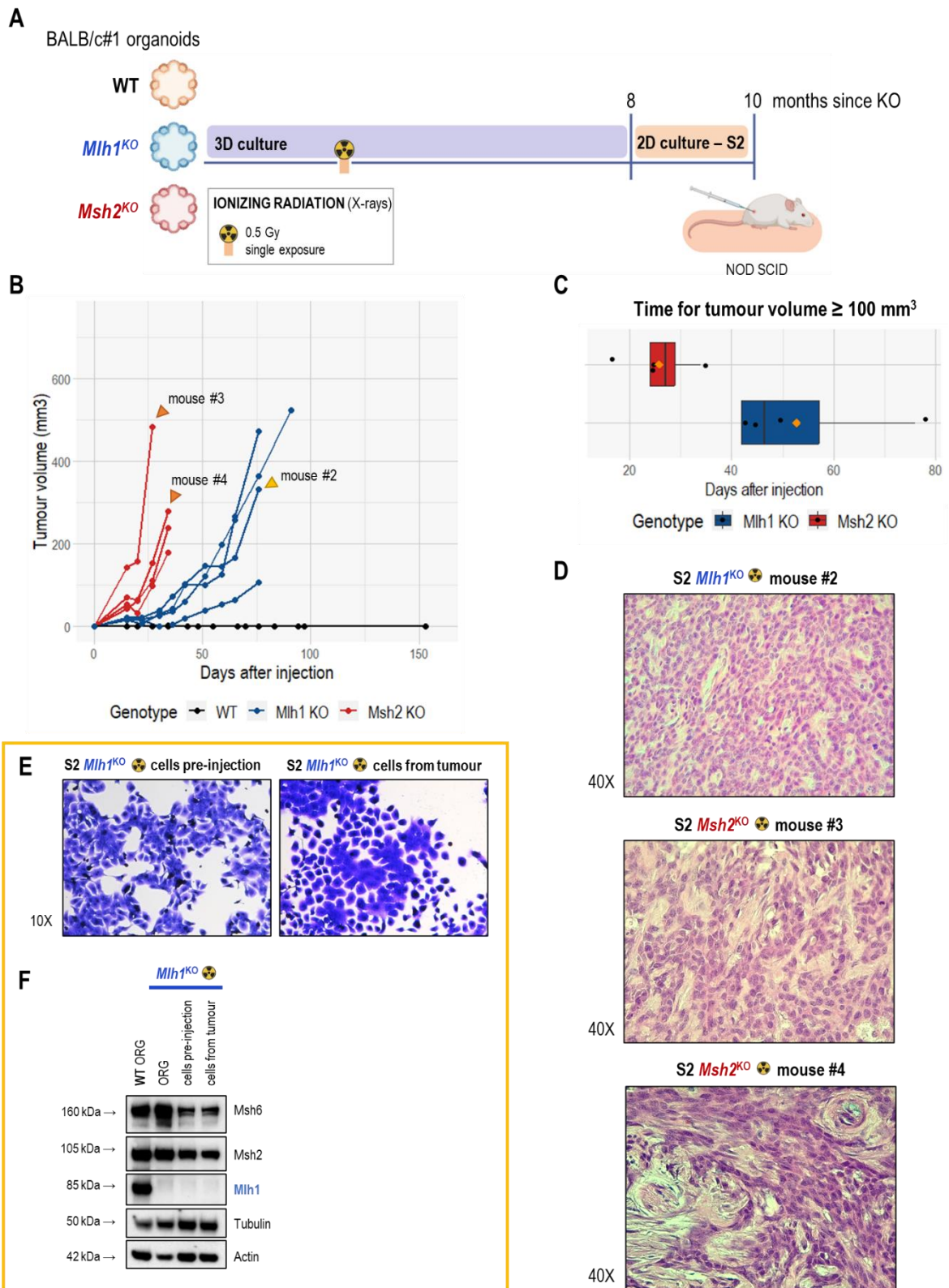
**Figure 17.**



*Figure 17. **Assessment of tumorigenicity of series 2 Mlh1 KO cells, derived from non-irradiated organoids, upon subcutaneous injection in NOD SCID mice. A.** Schematic representation of the cell culture phases and the injection time point. Created using BioRender.com. **B.** In vivo growth curves upon cell injection at 10 months of global culture since the knockout event. Each line corresponds to a single mouse. The tumour masses obtained from the mice indicated by orange arrows (mice #1 and #4) were used for subsequent post-in vivo analyses. **C.***

*Haematoxylin and eosin staining of the tumour masses explanted from mice #1 and #4. Two representative fields are presented. S2 = cell series 2.*

*In vivo* tumorigenesis assays described up to this point were performed by injecting in mice MMRd 2D cultures without co-injection of any correspondent WT control. As previously mentioned, we did not manage to stably grow in 2D conditions neither the WT cells from series 1 nor the WT cells from non-irradiated organoids in series 2. Thus, we performed another set of *in vivo* tumorigenesis experiments injecting cells from series 2 derived from irradiated organoids as well as all cells from series 3.

Cell series 2, derived from irradiated organoids, was injected in mice at 10 months from the KO event (Figure 18A). Importantly, MMRd cells gave rise to tumour masses in all mice, while no palpable masses developed from WT cells (Figure 18B). We observed different growth dynamics in *Mlh1* KO and *Msh2* KO arms, as the average time necessary to reach a measured volume over 100 mm$^3$ was 53 days and 26 days, respectively (Figure 18C). We also assessed tumour histology in some representative mice (Figure 18D) and we retrieved cells back from one mouse per experimental arm. Figure 18E-F shows the characterization of cells derived from the explant of a mouse from the *Mlh1* KO group. Cells retrieved from the tumour presented a morphology similar to that of the correspondent cells stained before the injection and were still completely knocked out for *Mlh1* gene.

**Figure 18.**



*Figure 18. **Assessment of tumorigenicity of series 2 WT and MMRd cells, derived from irradiated organoids, upon subcutaneous injection in NOD SCID mice. A.** Schematic representation of the cell culture phases and the*

The last *in vivo* tumorigenesis experiments were performed on the cells from series 3, which were derived from organoids at 6 months of culture since the KO event. For cell series 3, we had the complete set of genotypes (WT, *Mlh1* KO and *Msh2* KO) for 2D cultures derived from both irradiated and not-irradiated organoids. *In vivo* experiments with cell series 3 were performed at 12 months, a time that allowed the establishment of steady-growing 2D cultures also from WT organoids (Figure 19A). In the case of cells derived from not-irradiated organoids, *Mlh1* KO cells generated tumour masses with very fast dynamics, while *Msh2* KO cells only gave rise to a small mass in 1 out of 4 mice and with a long delay (mass was measurable from day 137 post injection) (Figure 19B). However, when we performed the same experiment on the correspondent cells which were derived with the same modalities and timing but from irradiated organoids, both *Mlh1* and *Msh2* KO arms generated measurable tumour masses in 10-40 days (Figure 19C). We confirmed the epithelial origin of the tumours generated from MMRd cells analysing histology in some representative mice (Figure 19D and E). Consistently with previous experiments, WT control arms did not originate any tumour mass derived from injected cells, as the only mass generated in a WT arm around day 65 showed small tightly packed CD45^{+} cells, thus probably being a lymphoma (Figure 19F).
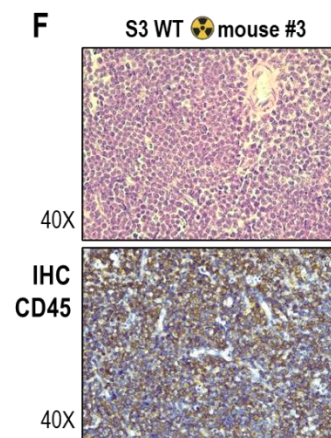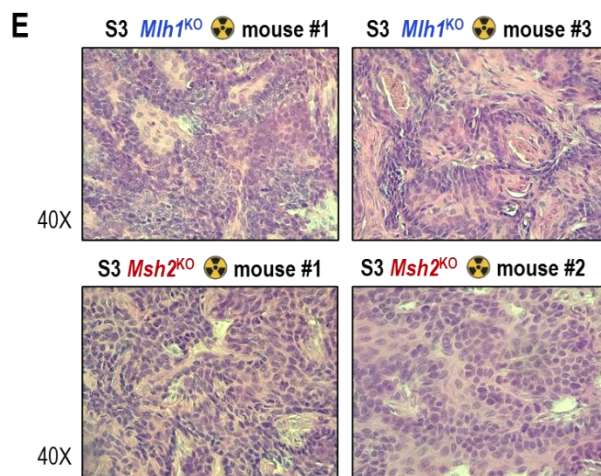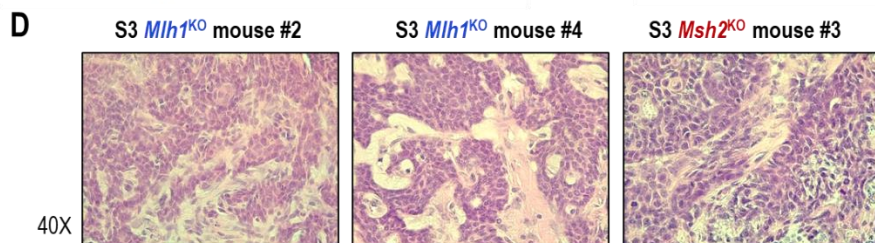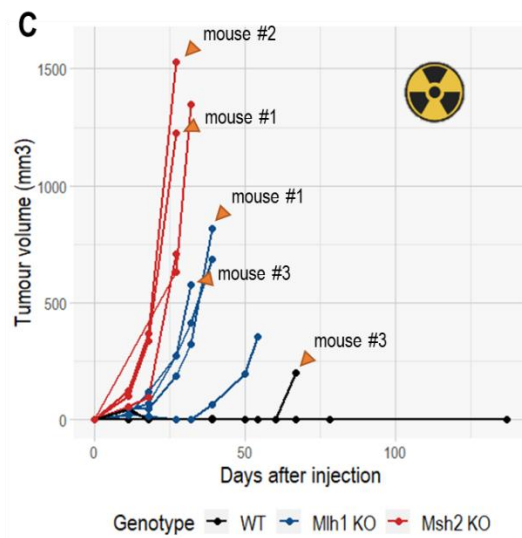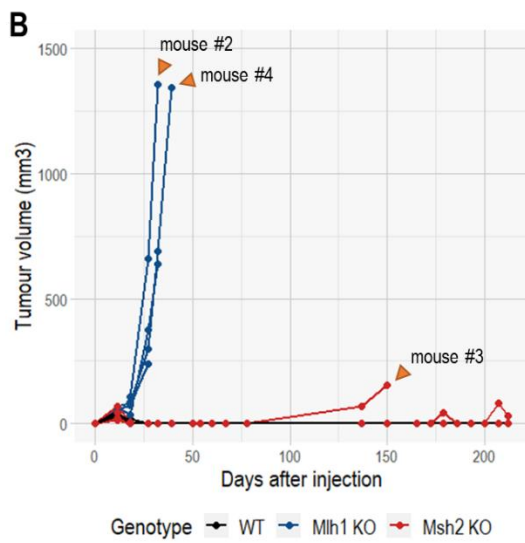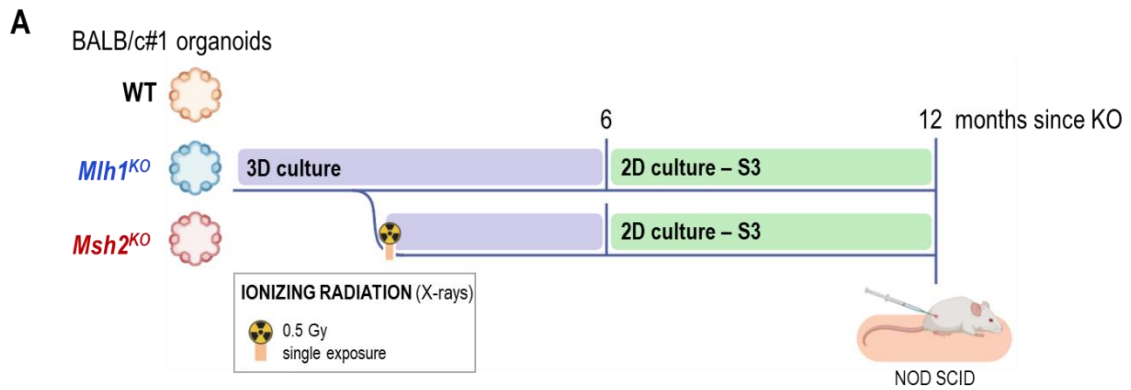
**Figure 19.**

*Figure 19. **Assessment of tumorigenicity of series 3 WT and MMRd cells, upon subcutaneous injection in NOD SCID mice at 12 months of overall culture. A.** Schematic representation of the cell culture phases and the injection time point. Created using BioRender.com. **B.** In vivo growth curves upon injection of cells derived from non-irradiated organoids. Each line corresponds to a single mouse. The tumour masses obtained from the mice indicated by orange arrows (Mlh1 KO mice #2 and #4 and Msh2 KO mouse #3) were used for subsequent post-in vivo analyses. **C.** In vivo growth curves upon injection of cells derived from irradiated organoids. Each line corresponds to a single mouse. The tumour masses obtained from the mice indicated by orange arrows (Mlh1 KO mice #1 and #3, Msh2 KO mice #1 and #2 and WT mouse #3) were used for subsequent post-in vivo analyses. **D.** Haematoxylin and eosin staining of tumour masses arisen from the injection of MMRd cells derived from non-irradiated organoids. **E.** Haematoxylin and eosin staining of tumour masses arisen from the injection of MMRd cells derived from irradiated organoids. **F.** Haematoxylin and eosin staining and immunohistochemical mouse-specific CD45 staining of the only tumour mass arisen in a mouse from the control WT arm. S3 = cell series 3.*

As all series 3 MMRd cells, but *Msh2* KO cells derived from not-irradiated organoids, showed a 100% engraftment rate, we chose to reevaluate their tumorigenic potential at a later time point. We then repeated a similar assay by injecting cell series 3 at 15 months since the KO event (Figure 20A). We used more NOD SCID mice per experimental arm compared to previous *in vivo* experiments (6 instead of 4 mice). Conversely to the 12-month time point, *Mlh1* KO cells from non-irradiated organoids did not develop large tumours, as mice had to be sacrificed very soon after injection because masses were ulcerated. As far as the *Msh2* KO arm is concerned, 1 out of 6 mice grew a tumour mass, but the experiment is still currently ongoing, and another mouse carries a growing mass (Figure 20B). Importantly, cells from irradiated organoids confirmed the promising results obtained in the previous experiment (Figure 20C).
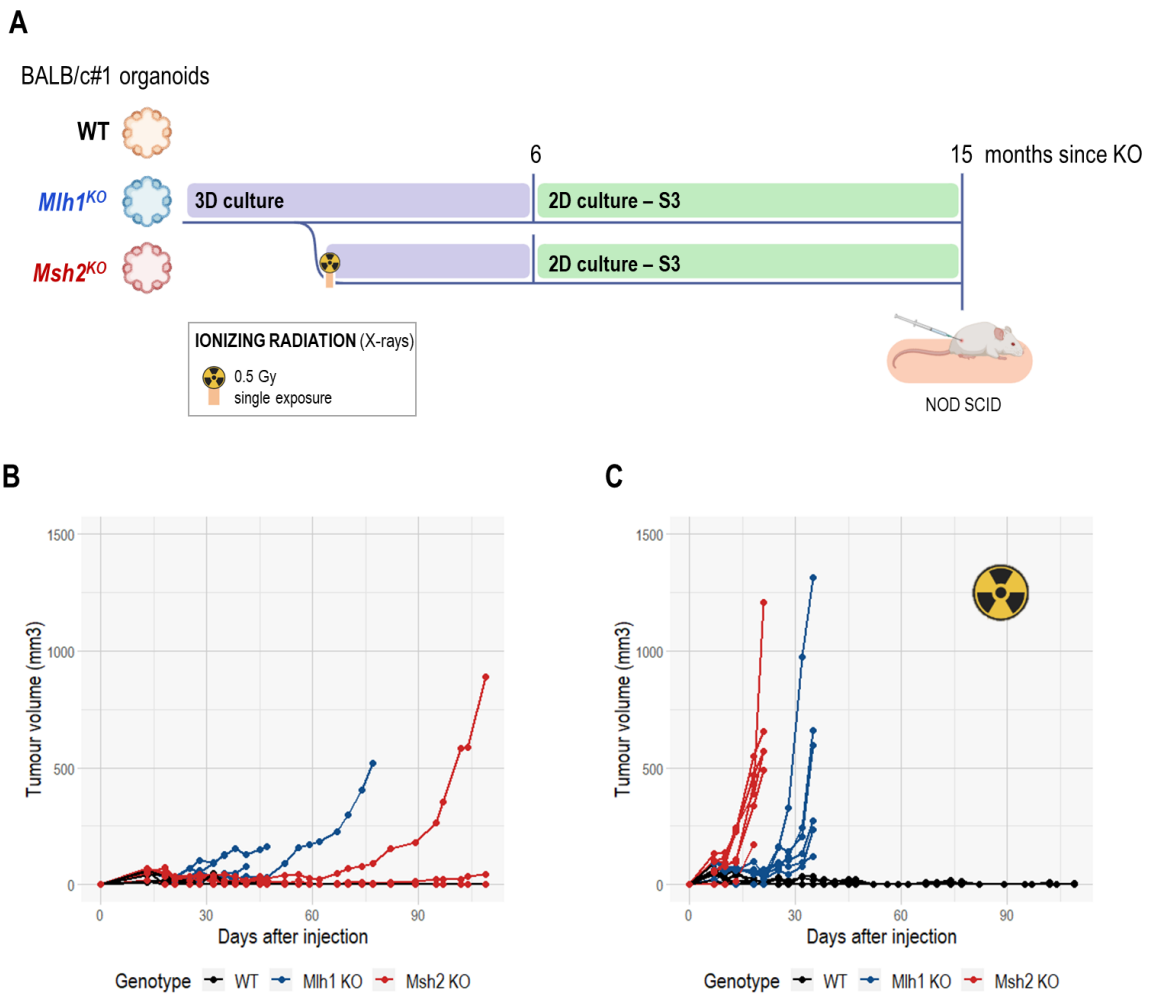
**Figure 20.**



*Figure 20. **Assessment of tumorigenicity of series 3 WT and MMRd cells, upon subcutaneous injection in NOD SCID mice at 15 months of overall culture. A.** Schematic representation of the cell culture phases and the injection time point. Created using BioRender.com. **B.** In vivo growth curves upon injection of cells derived from non-irradiated organoids. Each line corresponds to a single mouse. **C.** In vivo growth curves upon injection of cells derived from irradiated organoids. Each line corresponds to a single mouse. S3 = cell series 3.*

To sum up *in vivo* tumorigenesis experiments performed injecting organoid-derived cells in NOD SCID mice, we can assert that WT cells (MMR-proficient) never formed a tumour mass, while MMR-deficient cells showed extensive tumorigenicity (with 25-100% engraftment rates) (Figure 21A). To quantify tumour growth dynamics and compare them among the different tumorigenesis experiments, we evaluated the time *in vivo* necessary for the development of a mass of at least 100 mm$^3$. The tumour growth time, measured as days after injection, was

plotted as a function of the injection time point (months of overall culture since the KO event). *Mlh1* KO cells injected at 12 and 15 months showed a significant reduction of the tumour growth time compared to cells injected at 10 months (p-value < 0.01) (Figure 21B), suggesting that the tumorigenic potential may increase with cell culture time. Similarly, in the case of the *Msh2* KO genotype, the time necessary to form a tumour mass of at least 100 mm$^3$ was significantly reduced when cells were injected at 10 and 15 months compared to 7 months. However, no statistical significance was reached testing the other comparisons, likely due to the presence of outlier points in 12- and 15-month injections: series 3 *Msh2* KO cells derived from non-irradiated organoids showed a long growing latency, forming 100 mm$^3$ tumours in 80-150 days (Figure 21C).
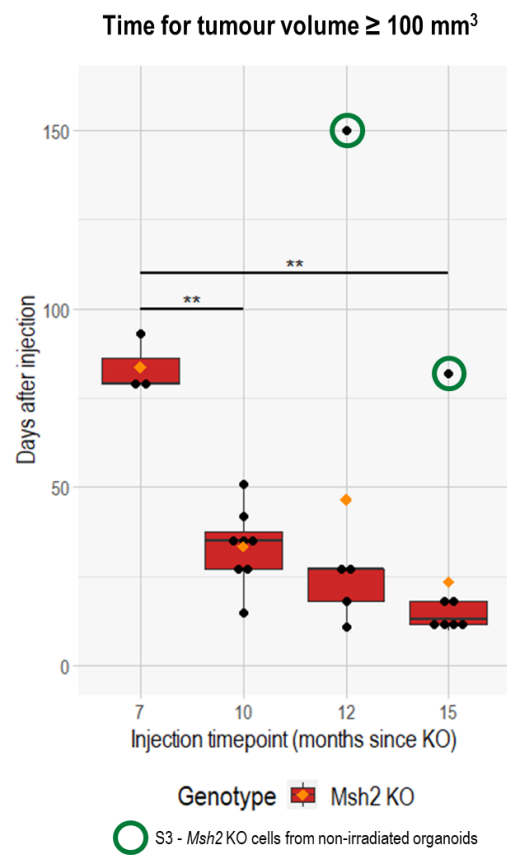
# Figure 21.

**A**

| Cell series | Genotype | X-irradiation | Injection timepoint (months since KO) | Engraftment rate (mice, %) |
|---|---|---|---|---|
| 1 | *Msh2* KO | yes | 7 | 3 out of 4 mice (75%) |
| 1 | *Msh2* KO | yes | 10 | 4 out of 4 mice (100%) |
| 2 | *Mlh1* KO | no | 10 | 4 out of 4 mice (100%) |
| 2 | WT | yes | 10 | 0 out of 4 mice (0%) |
| 2 | *Mlh1* KO | yes | 10 | 4 out of 4 mice (100%) |
| 2 | *Msh2* KO | yes | 10 | 4 out of 4 mice (100%) |
| 3 | WT | no | 12 | 0 out of 3 mice (0%) |
| 3 | *Mlh1* KO | no | 12 | 4 out of 4 mice (100%) |
| 3 | *Msh2* KO | no | 12 | 1 out of 4 mice (25%) |
| 3 | WT | yes | 12 | 0 out of 3 mice (0%) |
| 3 | *Mlh1* KO | yes | 12 | 4 out of 4 mice (100%) |
| 3 | *Msh2* KO | yes | 12 | 4 out of 4 mice (100%) |
| 3 | WT | no | 15 | 0 out of 6 mice (0%) |
| 3 | *Mlh1* KO | no | 15 | 4 out of 5 mice (80%) |
| 3 | *Msh2* KO | no | 15 | 2 out of 6 mice (30%) |
| 3 | WT | yes | 15 | 0 out of 6 mice (0%) |
| 3 | *Mlh1* KO | yes | 15 | 6 out of 6 mice (100%) |
| 3 | *Msh2* KO | yes | 15 | 6 out of 6 mice (100%) |
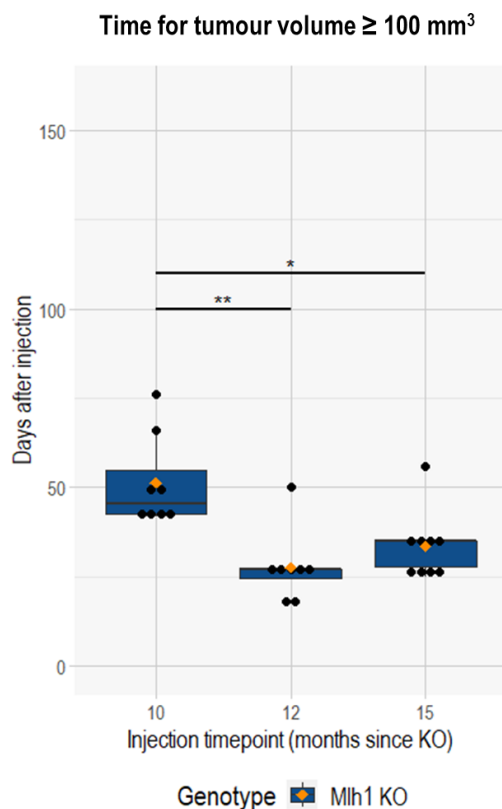


*Figure 21. **Overall results from tumorigenicity assays performed upon subcutaneous injection of WT and MMRd 2D cultures in NOD SCID mice. A.** Table indicating cell features, injection time points and engraftment rates. **B.** Box plot illustrating the time required for Mlh1 KO tumour masses to reach a 100 mm³ volume in relation*

*to the injection time point. Black dots indicate the single mice, while the orange square indicates the average time at each time point. The plot reports only statistics for the significant comparisons. \* = p-value ≤ 0.05; \*\* = p-value ≤ 0.01 **C.** Box plot illustrating the time required to Msh2 KO tumour masses to reach a 100 mm³ volume in relation to the injection time point. Black dots indicate the single mice, while the orange square indicates the average time at each time point. The plot reports only statistics for the significant comparisons. \*\* = p-value ≤ 0.01. S3 = cell series 3.*

**Molecular characterization of MMRd tumorigenic cells.**

From *in vivo* tumorigenesis experiments we found that the 2D-culture phase is fundamental for the acquisition of a neoplastic phenotype in our MMRd models. We thus focused on assessing the molecular differences between non-tumorigenic MMRd organoids and tumorigenic MMRd 2D-cultured cells in order to identify putative pathways that guide the malignant transformation process.

Firstly, we wondered whether MMRd 2D cultures harboured more marked MSI features compared to the corresponding 3D cultures. We thus compared cells and organoids with the same genotype at the same time point (considered as the time of overall culture since the inactivation of the MMR gene) and found that it was not the case. When we analysed the 5 mononucleotide repeat markers for the assessment of microsatellite status, we observed that 2D cultures had indeed the same or a lower number of shifted loci compared to organoids. Consistently, 2D cultures also displayed a lower tumour mutational burden. Figure 22A-B shows the representative comparison between the *Msh2* KO 2D culture from series 1 and the correspondent *Msh2* KO organoids at 10 months since the KO event.
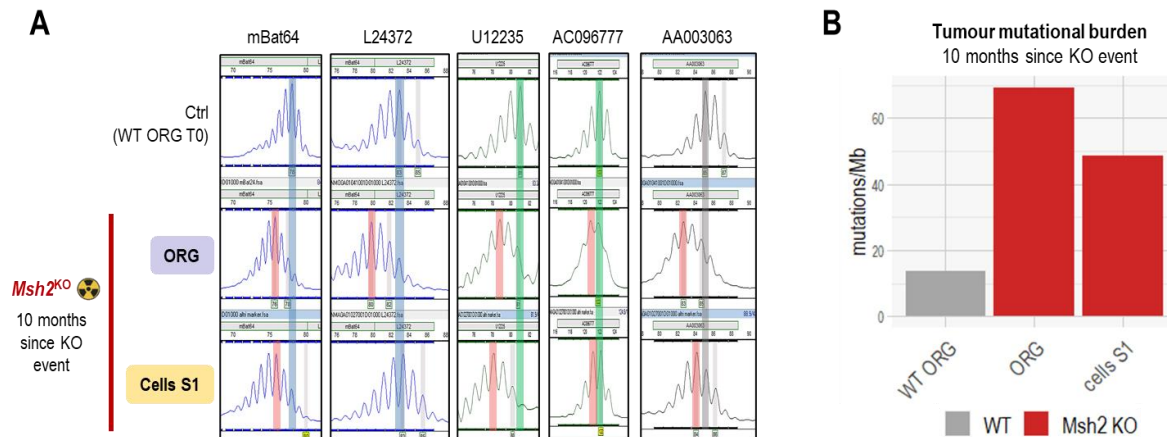
**Figure 22.**



*Figure 22. **Comparison of MSI features in Msh2 KO 2D culture from series 1 and the correspondent Msh2 KO organoids. A**. STR analysis for the assessment of the microsatellite status at 10 months of overall culture since the knockout event. Electropherograms show the PCR products for the 5 analysed loci. **B**. Histogram depicting tumour mutational burden at 10 months of overall culture since the knockout event, calculated as non-synonymous mutations per megabase of whole exome sequencing target genome. ORG = organoids; S1 = cell series 1; T0 = time zero (early-passage parental organoids).*

In order to identify putative driver pathways, we performed RNA sequencing on both 3D and 2D MMRd cultures at key time points (early 3-month time point and time points correspondent to cell injections and explants). We performed principal component analysis to evaluate the variance in the dataset and we observed that organoids and cells formed clearly separated clusters. All *Mlh1* KO and *Msh2* KO organoids placed close to each other, while MMRd cells formed two distinct groups (figure 23A). The following step was a differential gene expression analysis performed comparing MMRd tumorigenic cells together with cells retrieved from tumours (n = 12) against all non-tumorigenic MMRd organoids (n = 10). *Msh2* KO cells from series 3, derived from non-irradiated organoids which, once injected in NOD SCID mice, gave rise to tumours with a very long latency and a relatively low engraftment rate (25-30%), were excluded from this analysis. Using a false discovery rate of 0.05, we were able to identify 3402 differentially expressed genes among which 1538 were upregulated in tumorigenic cells versus non-tumorigenic organoids, while 1864 were downregulated (Figure 23B). We ranked the

genes combining fold change values (LogFC) and t-statistics and performed a Gene Set Enrichment Analysis (GSEA) using mouse hallmark-ortholog and KEGG pathway gene sets. Positively enriched gene sets included mitogenic signalling pathways, while among negatively enriched gene sets we noticed metabolic pathways. Glycolysis gene sets emerged as negatively enriched considering both hallmark and KEGG terms (Figure 23C and D). The gene encoding for the aldolase C enzyme (*Aldoc*), in particular, was among the top differentially expressed genes, resulting significantly downregulated in tumorigenic cells compared to organoids (adjusted p-value < 0.0001, Figure 23B and E).

Results from transcriptome analysis indicate that the passage from 3D to 2D culture implied an important reshaping towards a more proliferative cellular phenotype, accompanied by a metabolic rearrangement.
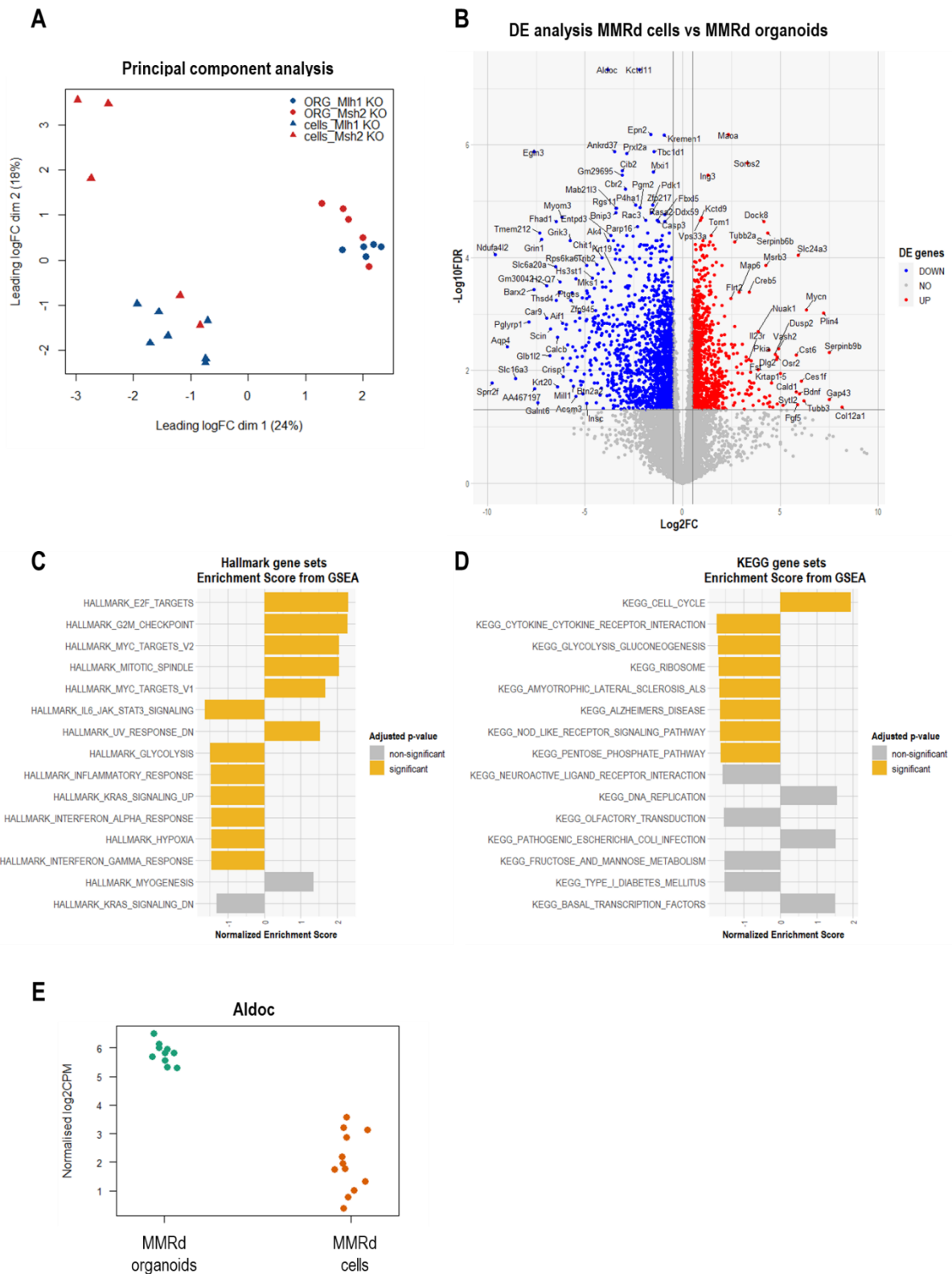
**Figure 23.**



*Figure 23. **Differential gene expression analysis in MMRd cells (2D cultures) versus MMRd organoids (3D cultures). A.** Principal component analysis, considering the two dimensions with the highest percentage of explained variance. **B.** Volcano plot representing the results from the differential gene expression analysis. **C.***

*Bar plot showing the top 15 gene sets from GSEA on mouse hallmark-ortholog gene sets. **D.** Bar plot showing the top 15 gene sets from GSEA on mouse KEGG gene sets. **E.** Aldoc gene expression levels in MMRd organoids and cells. CPM = counts per million; DE = differentially expressed; FC = fold change; FDR = false discovery rate; ORG = organoids.*

To further characterize the MMRd cultures retrieved from tumour masses and assess their evolution in relation to the various 2D culture derivations, we analysed whole exome sequencing data to evaluate the extent of their mutational divergence. As done for tumour mutational burden calculation, we excluded mutations already detected in parental early-passage BALB/c organoids to keep somatic mutations only. We analysed 5 *Mlh1* KO cultures: S2_IR_#2 and S2_IR_#3 were derived from brother mice from the same *in vivo* experiment, while the other three derived from distinct 2D cultures and were retrieved from independent experiments (Figure 24A). When we consider all somatic mutations, S2_IR_#2 and S2_IR_#3 showed the highest degree of overlap (sharing over 60% of all somatic mutations) (Figure 24B). Interestingly, the divergence of cells derived from different 2D cultures became more evident when we considered exclusively mutations with predicted high or moderate impact (excluding synonym, intergenic, intronic, 5'-UTR and 3'-UTR alterations) (Figure 24C). We repeated the same analysis on 3 *Msh2* KO cultures, confirming again the substantial divergent evolution of models obtained from independent 2D culture derivations (Figure 25).

**Figure 24.**



*Figure 24. **Genetic evolution of different Mlh1 KO 2D cultures.** A. Schematic representation summarising the experimental design. Created using BioRender.com. **B.** Euler diagram depicting the overlap of somatic mutations in cells retrieved from tumours. **C.** Euler diagram depicting the overlap of somatic mutations with predicted high/moderate impact in cells retrieved from tumours. S1 = cell series 1; S2 = cell series 2; S3 = cell series 3; noIR = cells derived from non-irradiated organoids; IR = cells derived from irradiated organoids. Euler diagrams present a 0.01 error due to the intersection of more than 3 samples.*
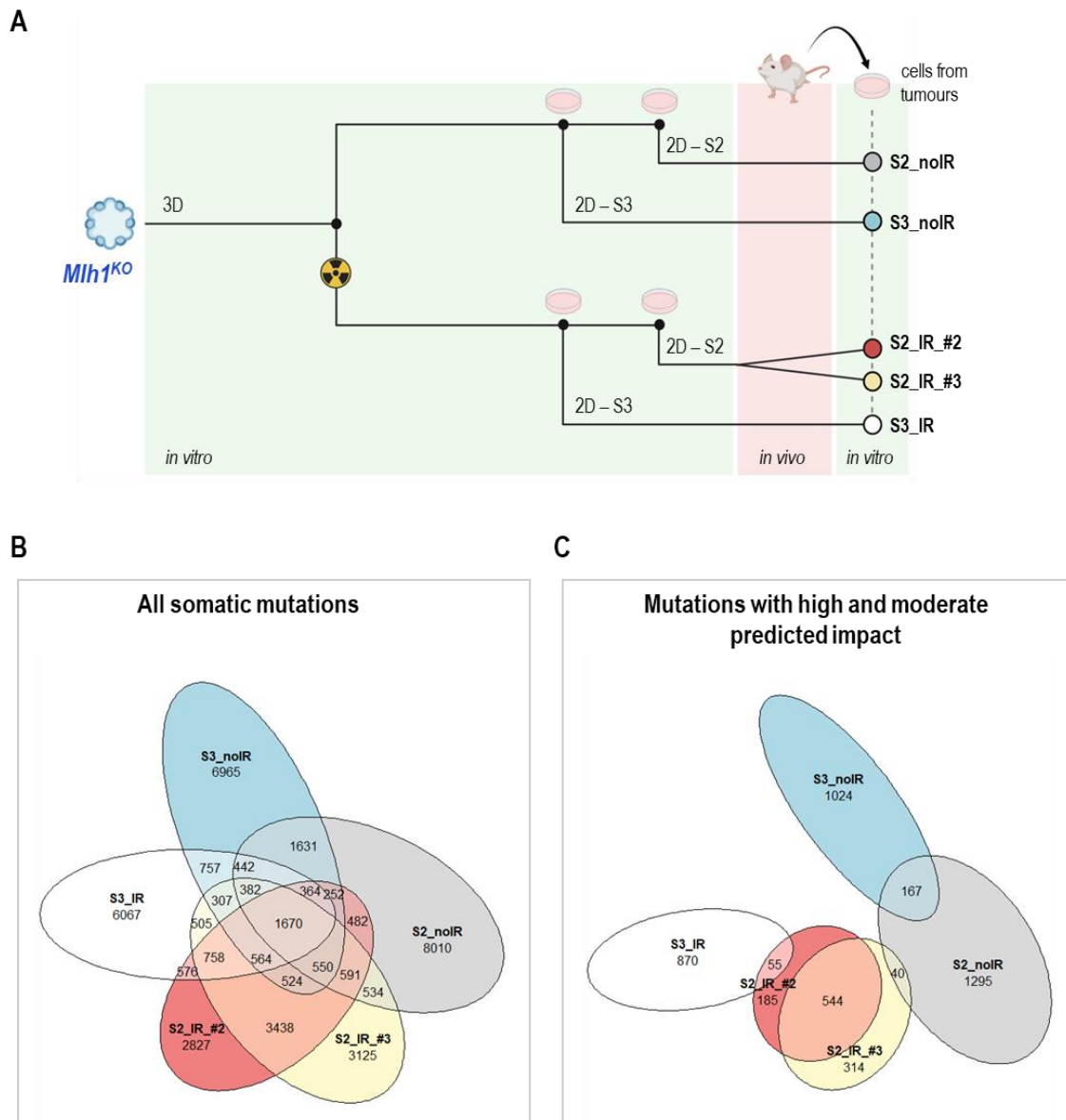
**Figure 25.**
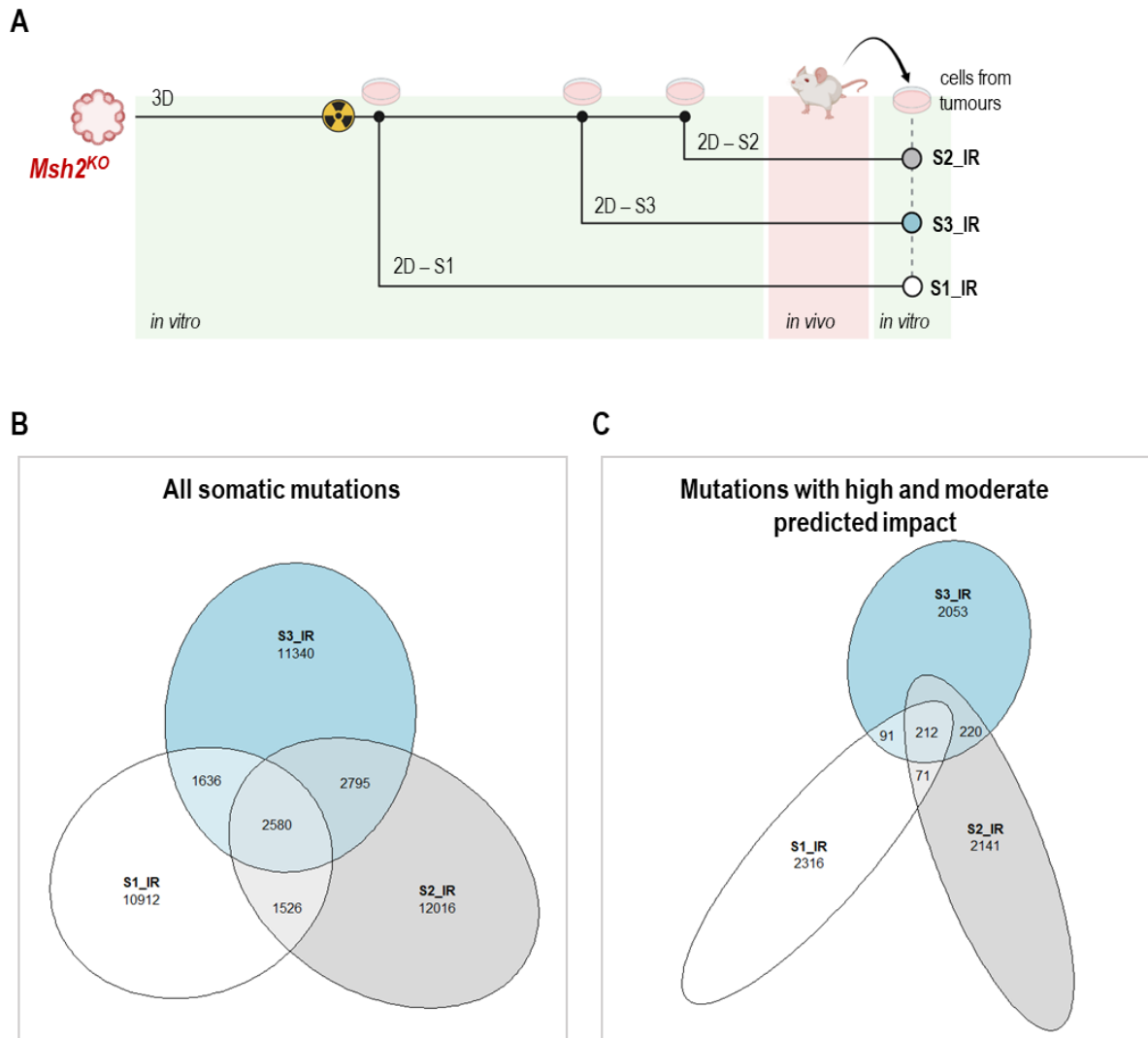


*Figure 25. **Genetic evolution of different Msh2 KO 2D cultures. A**. Schematic representation summarising the experimental design. Created using BioRender.com. **B.** Euler diagram depicting the overlap of somatic mutations in cells retrieved from tumours. **C.** Euler diagram depicting the overlap of somatic mutations with predicted high/moderate impact in cells retrieved from tumours. S1 = cell series 1; S2 = cell series 2; S3 = cell series 3; IR = cells derived from irradiated organoids. Euler diagrams present a 0.00 error.*

By examining 63 cases of hypermutated gastric cancer, TCGA identified 37 genes significantly mutated within the MSI subgroup (43). To assess whether our models could recapitulate the MSI GC mutational landscape, we searched for coding mutations in mouse orthologs corresponding to the gene panel identified by TCGA. Analysed samples included again MMRd cells retrieved from NOD SCID mice and data were filtered to include only mutations with

allele frequency equal to or greater than 0.2. We found mutations in 21 out of 35 mouse orthologs, including *Kras, Arid1a, Erbb3, Tpr53* and the MHC class I gene *H2-K1* (Figure 26A). Furthermore, when we looked at alterations specifically present in each MMRd culture, we observed that while some of them were shared across multiple samples, the vast majority were cell line specific (Figure 26B and C).

These data further confirm that by means of separate 2D culture derivations, even if originated from the same initial MMRd organoid line, we are able to generate distinct models exhibiting a unique set of somatic mutations. These models also demonstrate the ability to recapitulate a considerable portion of the alterations previously associated with the MSI subtype.
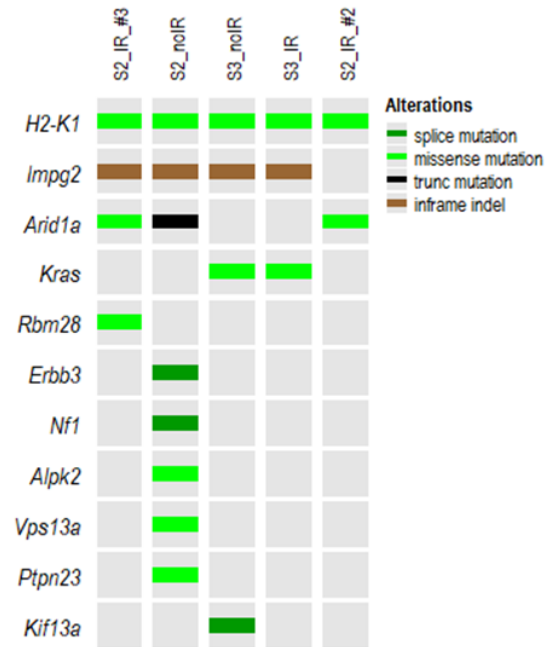
**Figure 26.**

# A

**TCGA MSI genes**

| N | Human gene | Mouse ortholog gene | Mutation |
|---|---|---|---|
| 1 | IWS1 | Iws1 | Present |
| 2 | ZBTB20 | Zbtb20 | Present |
| 3 | IMPG2 | Impg2 | Present |
| 4 | KIF13A | Kif13a | Present |
| 5 | LMAN1 | Lman1 | Present |
| 6 | ALPK2 | Alpk2 | Present |
| 7 | CUL1 | Cul1 | Present |
| 8 | PTEN | Pten | Absent |
| 9 | BCORL1 | Bcorl1 | Absent |
| 10 | FBXW7 | Fbxw7 | Absent |
| 11 | IGF2BP3 | Igf2bp3 | Present |
| 12 | LARP4B | Larp4b | Absent |
| 13 | KRAS | Kras | Present |
| 14 | CHRD | Chrd | Absent |
| 15 | IRF2 | Irf2 | Absent |
| 16 | NF1 | Nf1 | Present |
| 17 | HDAC4 | Hdac4 | Absent |
| 18 | TBL1XR1 | Tbl1xr1 | Absent |
| 19 | B2M | B2m | Absent |
| 20 | IL2RG | Gm20489 | Absent |
| 20 | IL2RG | Il2rg | Absent |
| 21 | TMEM63A | Tmem63a | Present |
| 22 | FRMD4A | Frmd4a | Absent |
| 23 | PTPN23 | Ptpn23 | Present |
| 24 | ERBB3 | Erbb3 | Present |
| 25 | EP300 | Ep300 | Present |
| 26 | RBM28 | Rbm28 | Present |
| 27 | PIK3CA | Pik3ca | Absent |
| 28 | VPS13A | Vps13a | Present |
| 29 | ARID1A | Arid1a | Present |
| 30 | CIC | Cic | Present |
| 31 | NAA25 | Naa25 | Absent |
| 32 | PAX6 | Pax6 | Present |
| 33 | RNF43 | Rnf43 | Present |
| 34 | TP53 | Trp53 | Present |
| 35 | HLA-B | H2-K1 | Present |
| 35 | HLA-B | H2-K2 | Absent |
| 36 | MYEOV | none | Absent |
| 37 | GPR124 | none | Absent |

**Mutation in cells from tumour**
Present
Absent

# B

**Mlh1 KO cells from tumours**

Samples: S2_IR_#3, S2_noIR, S3_noIR, S3_IR, S2_IR_#2

Genes: H2-K1, Impg2, Arid1a, Kras, Rbm28, Erbb3, Nf1, Alpk2, Vps13a, Ptpn23, Kif13a

**Alterations**
splice mutation
missense mutation
trunc mutation
inframe indel

# C

**Msh2 KO cells from tumours**

Samples: S2_IR, S3_IR, S1_IR

Genes: Trp53, Impg2, H2-K1, Vps13a, Kif13a, Ep300, Arid1a, Erbb3, Nf1, Ptpn23, Zbtb20, Iws1, Tmem63a, Cul1, Igf2bp3, Rnf43, Pax6, Kras, Cic

**Alterations**
splice mutation
missense mutation
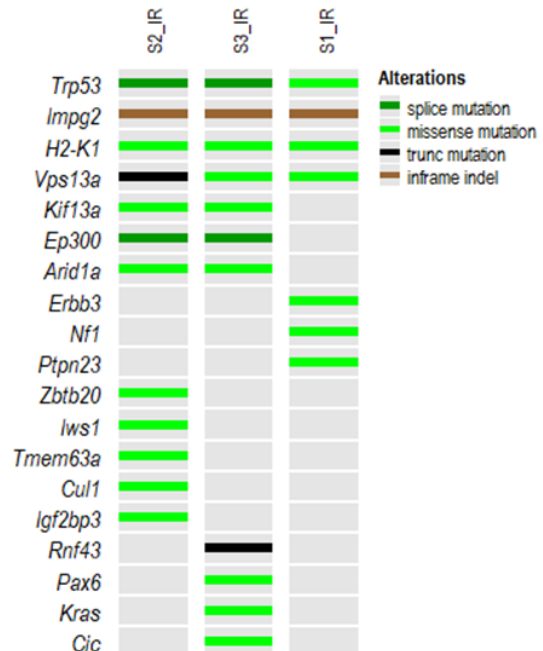trunc mutation
inframe indel

*Figure 26. **Analysis of MMRd cultures for mutations in 37 TCGA MSI genes. A**. Table indicating the presence/absence of mutations in the genes significantly altered in MSI GC. **B.** Oncoprint visualisation of*

*alterations in TCGA MSI gene panel in Mlh1 KO cells retrieved from tumours.* **C.** *Oncoprint visualisation of alterations in TCGA MSI gene panel in Msh2 KO cells retrieved from tumours.*

**Generation of syngeneic allograft mouse models of MSI gastric cancer.**

The final goal of my PhD project is the generation of mouse syngeneic models of MSI gastric cancer suitable to be injected back into immunocompetent BALB/c mice. We knew from the literature that the Cas9 protein we used to generate bulk MMRd models could be potentially immunogenic. *Streptococcus pyogenes*, from which the most used Cas9 nuclease is derived, is indeed an important human commensal and anti-Cas9 antibodies and T-cells have been detected in human plasma (171). Furthermore, some studies revealed the existence of an innate and adaptive cellular immune response to Cas9 protein also in mouse models (172).

We analysed Cas9 expression in our MMRd bulk models via real-time PCR. WT organoids and cells were used as negative controls. Interestingly, Cas9 expression levels decreased over time and by changing culture modalities: MMRd cells from series 3, analysed at 15 months of overall culture since the genetic inactivation of the target gene via CRISPR/Cas9 technique, showed a 70-80% reduction in Cas9 expression compared to correspondent organoids at 3 months of culture (Figure 27).
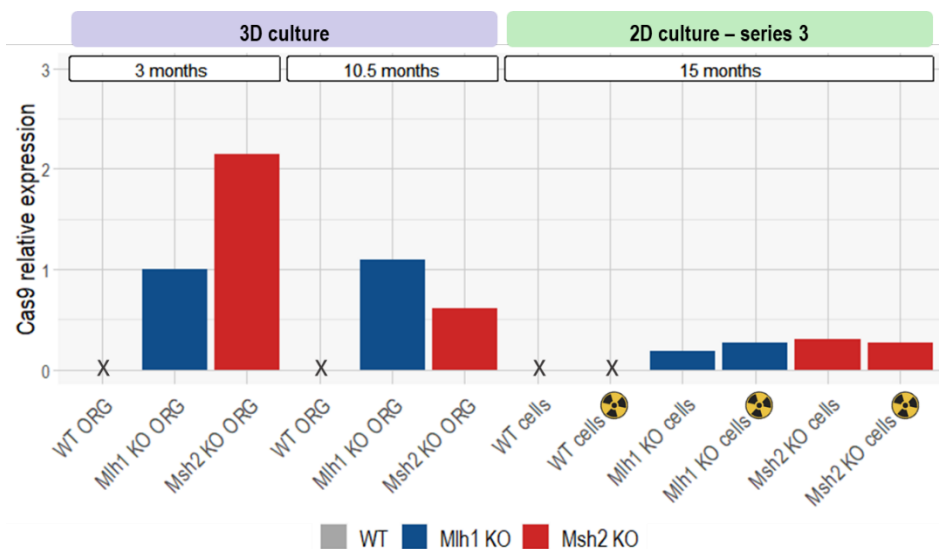
**Figure 27.**

Considering their relatively low Cas9-expression levels, we tried to inject MMRd cells from series 3 at 15-month time point also into BALB/c mice to assess their ability to grow in the presence of a complete immune system (Figure 28A). Compared to the results we achieved with injection in NOD SCID mice, cells formed tumours less effectively in BALB/c mice. If we consider cells derived from non-irradiated organoids, only one mouse from *Mlh1* KO cells formed a growing mass after a latency of 90 days from injection (Figure 28B). Regarding cells derived from irradiated organoids, several mice presented palpable masses after 20-30 days, but, in many cases, we observed ulcerating masses and only 3 mice developed relatively large tumour masses (volume over 500 mm$^3$) (Figure 28C).
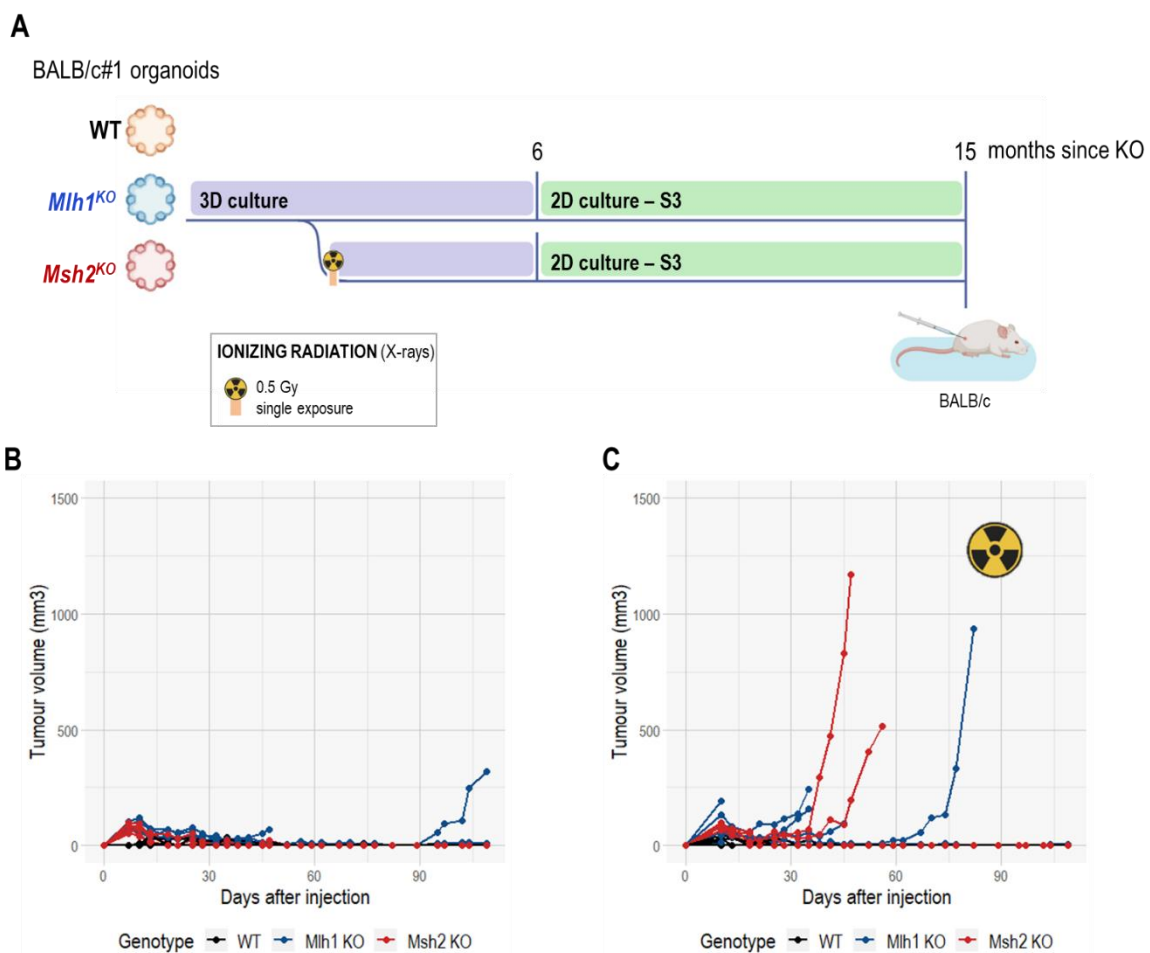
**Figure 28.**

*Figure 28. **Subcutaneous injection of series 3 WT and MMRd cells in immunocompetent BALB/c mice. A.** Schematic representation of the cell culture phases and the injection time point. S3 = cell series 3. Created using BioRender.com. **B.** In vivo growth curves upon injection of cells derived from non-irradiated organoids. Each line corresponds to a single mouse. **C.** In vivo growth curves upon injection of cells derived from irradiated organoids. Each line corresponds to a single mouse.*

In order to prevent any possible issue related to Cas9 immunogenicity, we optimized the genome editing protocol to generate other models avoiding stable Cas9 integration. MMRd bulk models described up to this point were obtained using lentiviruses to transduce both Cas9 and sgRNAs. To knock out the target MMR gene without integrating the Cas9 sequence into the genomic DNA of the host cell, we pre-infected organoids with sgRNA lentiviruses and, after a cycle of antibiotic selection, we introduced the Cas9 plasmid using liposomes. Forty-eight hours after the transfection organoids underwent a single cycle of selection with 10 µg/ml blasticidin to enrich transiently Cas9-expressing cells before the single-cell cloning. We generated multiple *Mlh1* KO and *Msh2* KO clones cloning single cells in 96-well plates (Figure 29A). The average efficiency of Cas9-transient gene editing procedure was close to 30% (1 out of 3 screened clones was knockout for the target gene). We assessed Cas9 expression in MMRd newly generated clones using stable-Cas9 MMRd bulk organoids and WT BALB/c organoids as positive and negative controls, respectively. Figure 29B shows a representative real-time PCR analysing two *Mlh1* KO clones and two *Msh2* KO clones which resulted in very low or null Cas9 expression. Cas9 was undetected in *Mlh1* KO clone #1 and *Msh2* KO clone #1.

As done for bulk MMRd models, we grew cells in 3D in the first period after the KO event and then we moved to 2D culture conditions. *Mlh1* KO clone #1 was cultured in 2D conditions starting from 4 months (a time sufficient to develop MSI) and was injected in both NOD SCID and BALB/c mice at 6 months of overall culture (Figure 29C). Importantly, this clone was able to generate tumour masses in both immunodeficient and immunocompetent mice with very fast dynamics. All mice were explanted within 30 days from injection and cells were retrieved from

all tumour masses (Figure 29D). We checked tumour histology and observed no substantial differences between masses grown in NOD SCID and BALB/c mice. In both cases, tumour sections presented two different cell populations, one formed by smaller cells and another one including big cells with enlarged eosinophilic cytoplasm and evident nucleoli (Figure 29E).

**Figure 29.**



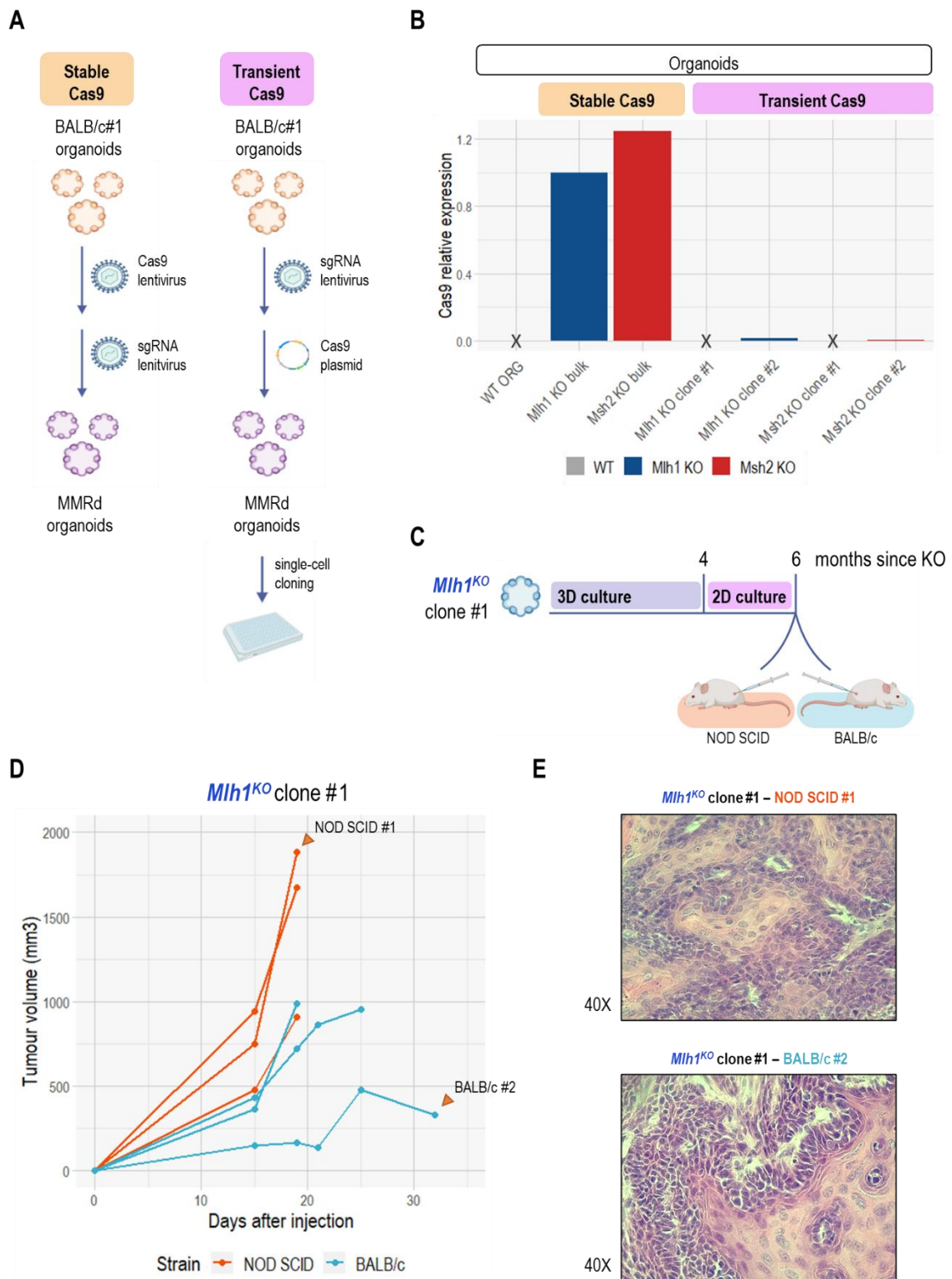*Figure 29. **Generation of MMRd Cas9-free clones and evaluation of tumour growth in NOD SCID and BALB/c mice. A.** Schematic representation of the used genome editing protocols. Created using BioRender.com. **B.** Evaluation of Cas9 expression via real-time PCR in representative MMRd clones obtained using genome editing protocol with transient Cas9 expression. Stable-Cas9 MMRd bulk organoids and WT BALB/c organoids were*

*used as positive and negative controls, respectively. X represents cases in which Cas9 was undetected. **C.** Schematic representation of the cell culture phases and the injection time point for Mlh1 KO clone #1. Created using BioRender.com. **D.** In vivo growth curves upon injection of cells derived from Mlh1 KO clone #1 in NOD SCID and BALB/c mice (3 mice/group). Each line corresponds to a single mouse. The orange arrows indicate the mice (NOD SCID mouse #1 and BALB/c mouse #2) corresponding to the representative haematoxylin and eosin images in panel **E**.*

We confirmed via Western Blot the KO of *Mlh1* gene in cells cultured *in vitro* from clone #1 at several time points and also in the correspondent cells retrieved from tumour masses (Figure 30A). *Mlh1* KO clone #1 cells at injection and explant time points and cells rederived from tumours underwent both WES and RNAseq. Examining the molecular traits of tumours grown in the presence/absence of the immune system could potentially help elucidating immune escape mechanisms. Taking advantage of RNAseq data, we thus performed a differential gene expression analysis to compare cells grown up in immunocompetent and immunocompromised mice. Probably due to the limited numerosity of the analysed dataset (3 cell lines from BALB/c mice versus 3 cell lines from NOD SCID mice), only 12 genes reached statistical significance with a false discovery rate of 0.05. *Gm40514*, *Gm42031*, *Gm46156*, *Gm40525*, *Vgll3, Cryab, Cald1* and *Anxa1* were downregulated in cells from BALB/c mice, while *Hmga1b, Hmga1*, *Areg* and *Ier3* were upregulated. More hits emerged when we raised the false discovery rate cutoff to 0.1, including *Vegfa* among upregulated genes and *Gas6* among downregulated genes (Figure 30B).

**Figure 30.**
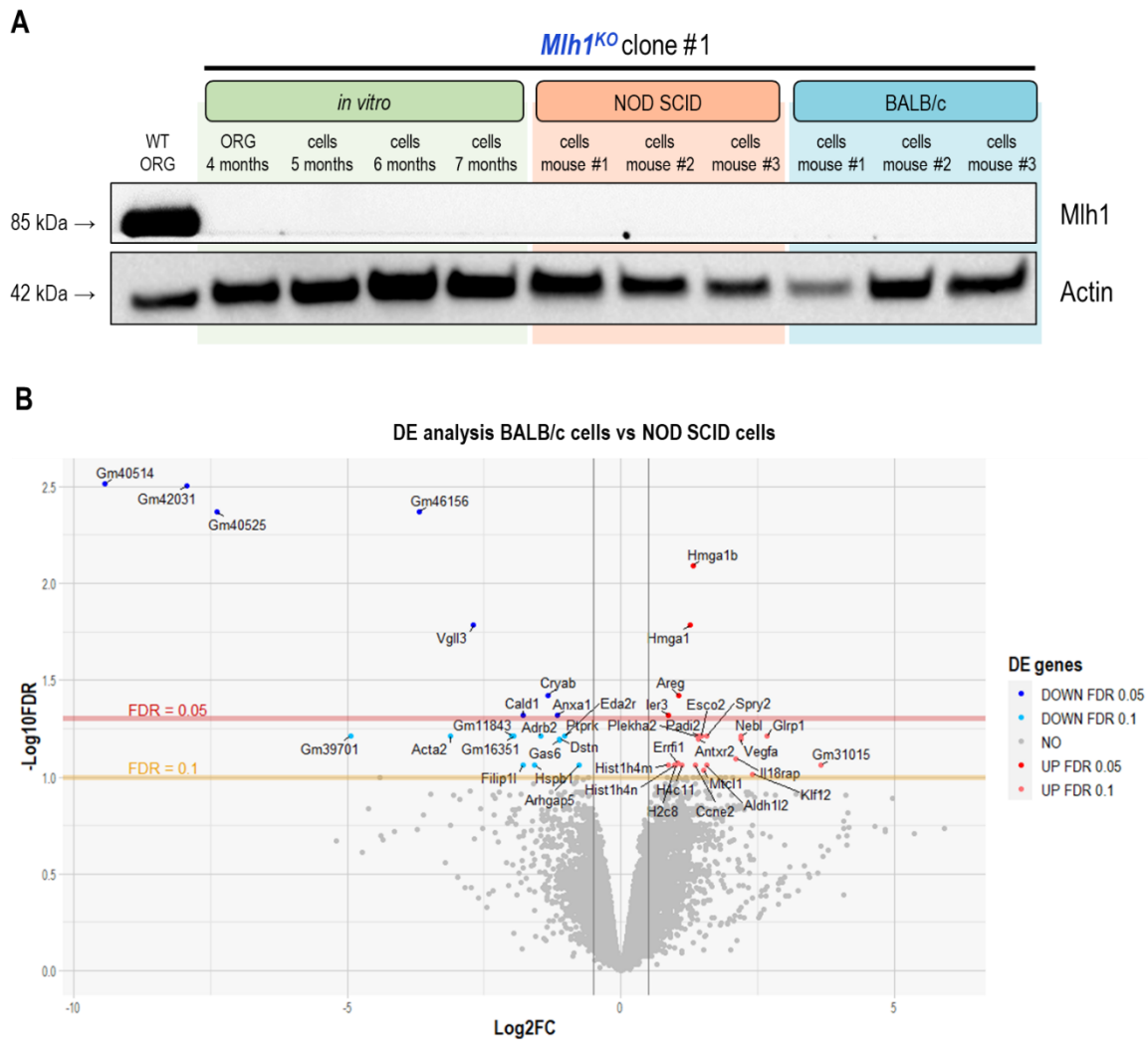


*Figure 30. **Characterisation of cells retrieved from tumour masses derived from Cas9-free Mlh1 KO clone #1 (part 1). A.** Western blot analysis of Mlh1 protein in Mlh1 KO clone #1 at several stages of culture and in the related cells retrieved from the tumours grown up in NOD SCID and BALB/c mice. Actin was used as loading control. **B.** Volcano plot representing the results from the differential gene expression analysis executed comparing Mlh1 KO clone #1 cells retrieved from BALB/c versus NOD SCID mice. DE = differentially expressed; FDR = false discovery rate; FC = fold change; ORG = organoids.*

As done for bulk models, we searched WES data for alterations in the TCGA MSI gene panel. Cells derived from *Mlh1* KO clone #1 *in vivo* growth presented mutations in 10 out of 35 mouse orthologs (Figure 31A). Interestingly, cells derived from 5 out of 6 mice were mutated in *Kras* (Figure 31B). When we looked specifically at *Kras* alterations in Mlh1 KO clone #1 cells, we found that the hotspot G12D *Kras* mutation was already present *in vitro* (at both pre-injection and post-injection time points) and that all cells retrieved from tumours maintained it (cells from NOD SCID mouse #1 presented indeed *Kras* G12D, but below the 0.2 allele frequency threshold considered for the previous analysis) (Figure 31C). Taking advantage of *ConVarT* tool (https://convart.org/), we confirmed the correspondence of mouse Kras G12D with the mutation on the human *KRAS* gene (Figure 31D).

# Figure 31.

**A**

### TCGA MSI genes

| N | Human gene | Mouse ortholog gene | Mutation |
|---|---|---|---|
| 1 | IWS1 | Iws1 | |
| 2 | ZBTB20 | Zbtb20 | |
| 3 | IMPG2 | Impg2 | ■ |
| 4 | KIF13A | Kif13a | ■ |
| 5 | LMAN1 | Lman1 | |
| 6 | ALPK2 | Alpk2 | |
| 7 | CUL1 | Cul1 | |
| 8 | PTEN | Pten | |
| 9 | BCORL1 | Bcorl1 | ■ |
| 10 | FBXW7 | Fbxw7 | ■ |
| 11 | IGF2BP3 | Igf2bp3 | |
| 12 | LARP4B | Larp4b | |
| 13 | KRAS | Kras | ■ |
| 14 | CHRD | Chrd | |
| 15 | IRF2 | Irf2 | |
| 16 | NF1 | Nf1 | ■ |
| 17 | HDAC4 | Hdac4 | |
| 18 | TBL1XR1 | Tbl1xr1 | ■ |
| 19 | B2M | B2m | |
| 20 | IL2RG | Gm20489 | |
| | | Il2rg | |
| 21 | TMEM63A | Tmem63a | |
| 22 | FRMD4A | Frmd4a | |
| 23 | PTPN23 | Ptpn23 | |
| 24 | ERBB3 | Erbb3 | |
| 25 | EP300 | Ep300 | ■ |
| 26 | RBM28 | Rbm28 | |
| 27 | PIK3CA | Pik3ca | |
| 28 | VPS13A | Vps13a | |
| 29 | ARID1A | Arid1a | |
| 30 | CIC | Cic | ■ |
| 31 | NAA25 | Naa25 | |
| 32 | PAX6 | Pax6 | |
| 33 | RNF43 | Rnf43 | |
| 34 | TP53 | Trp53 | |
| 35 | HLA-B | H2-K1 | ■ |
| | | H2-K2 | |
| 36 | MYEOV | *none* | |
| 37 | GPR124 | *none* | |

**Mutation in cells from tumour**

■ Present
□ Absent

**B**



Mlh1 KO clone #1 cells from tumours

**C**

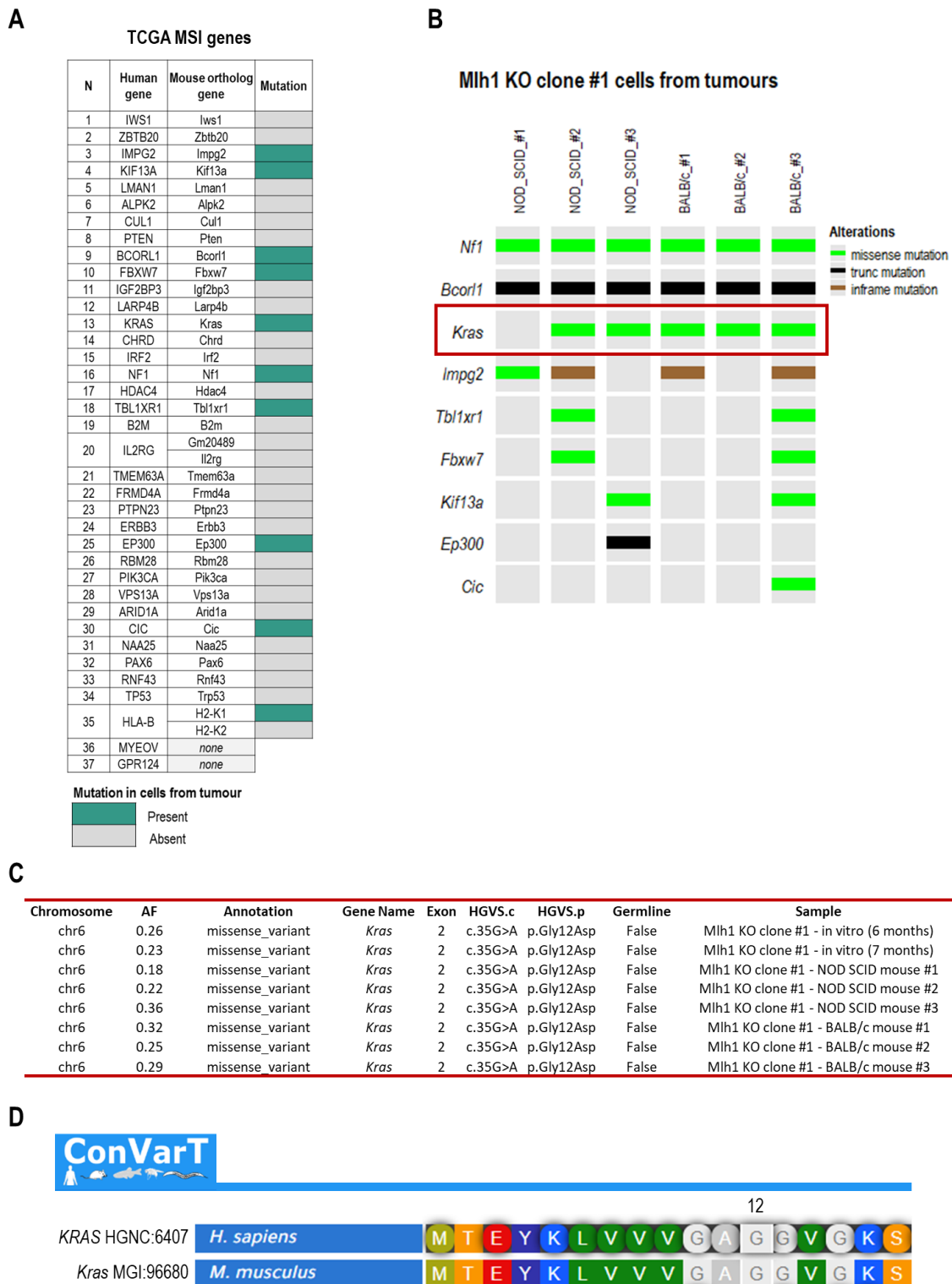| Chromosome | AF | Annotation | Gene Name | Exon | HGVS.c | HGVS.p | Germline | Sample |
|---|---|---|---|---|---|---|---|---|
| chr6 | 0.26 | missense_variant | *Kras* | 2 | c.35G>A | p.Gly12Asp | False | Mlh1 KO clone #1 - in vitro (6 months) |
| chr6 | 0.23 | missense_variant | *Kras* | 2 | c.35G>A | p.Gly12Asp | False | Mlh1 KO clone #1 - in vitro (7 months) |
| chr6 | 0.18 | missense_variant | *Kras* | 2 | c.35G>A | p.Gly12Asp | False | Mlh1 KO clone #1 - NOD SCID mouse #1 |
| chr6 | 0.22 | missense_variant | *Kras* | 2 | c.35G>A | p.Gly12Asp | False | Mlh1 KO clone #1 - NOD SCID mouse #2 |
| chr6 | 0.36 | missense_variant | *Kras* | 2 | c.35G>A | p.Gly12Asp | False | Mlh1 KO clone #1 - NOD SCID mouse #3 |
| chr6 | 0.32 | missense_variant | *Kras* | 2 | c.35G>A | p.Gly12Asp | False | Mlh1 KO clone #1 - BALB/c mouse #1 |
| chr6 | 0.25 | missense_variant | *Kras* | 2 | c.35G>A | p.Gly12Asp | False | Mlh1 KO clone #1 - BALB/c mouse #2 |
| chr6 | 0.29 | missense_variant | *Kras* | 2 | c.35G>A | p.Gly12Asp | False | Mlh1 KO clone #1 - BALB/c mouse #3 |

**D**



*Figure 31. **Characterisation of cells retrieved from tumour masses derived from Cas9-free Mlh1 KO clone #1 (part 2). A**. Table indicating the presence/absence of mutations in the genes significantly altered in MSI GC. **B**. Oncoprint visualisation of alterations in TCGA MSI gene panel in Mlh1 KO clone #1 cells retrieved from tumours. **C.** Table showing details about the G12D Kras mutation found in all sequenced cell cultures from Mlh1 KO clone*

**WRN dependency in syngeneic MSI gastric cancer models.**

Less than 5 years ago, CRISPR/Cas9-mediated knockout whole genome screens led to the emergence of Werner (WRN) RECQL helicase as a synthetic lethality in the specific context of microsatellite unstable cancers (123). Since then, several reports have shown that WRN is a promising drug target in MSI tumours, including cases that are refractory to targeted therapies, chemotherapy and immunotherapy (126). We wondered whether we were able to also recapitulate this feature of MSI tumours in our model. In collaboration with Dr Gabriele Picco, we tested Wrn dependency in BALB/c MMRd clones. CT26, an MSS mouse colon cancer cell line derived from BALB/c strain, was used as negative control. We tested Wrn dependency using RNA interference on clones grown in 2D culture conditions at 6 months of overall culture since the KO event. Interestingly, the *Msh2* KO clone showed a higher sensitivity to Wrn knockdown compared to the *Mlh1* KO clone, even if in the latter the siRNA transfection procedure was less effective (with almost 50% average viability upon transfection anti-Plk1 siRNA). Figure 32A shows the average of three independent experiments; data were normalized to non-targeting control siRNA. We confirmed via Western Blot Wrn downregulation in transfected samples. As Wrn inhibition in sensitive cells is usually associated with the accumulation of double-strand breaks, we also checked the phosphorylation of H2A.X, a marker of DNA damage response. Both MMRd clones showed a basal degree of H2A.X phosphorylation, but it increased upon Wrn silencing only in the *Msh2* KO clone (Figure 32B). We validated RNA interference results evaluating Wrn dependency via CRISPR/Cas9 genome editing. CT26 cells and MMRd clones were transduced to obtain Cas9-expressing cells and then transduced again to introduce sgRNAs targeting Wrn and, as controls,

a non-essential gene (*Cyp4f40*) and an essential gene (*Plk1*). Figure 32C shows crystal violet staining on cells fixed 7 days after transduction with sgRNA lentiviruses. Consistently with previous results, the growth of the *Msh2* KO clone, but not the *Mlh1* KO clone, was affected by Wrn genetic knockdown.

Further experiments are required to evaluate Wrn dependency in a greater variety of clones. However, these preliminary data suggest that mimicking and potentially studying this molecular feature in our mouse models could be feasible.

**Figure 32.**
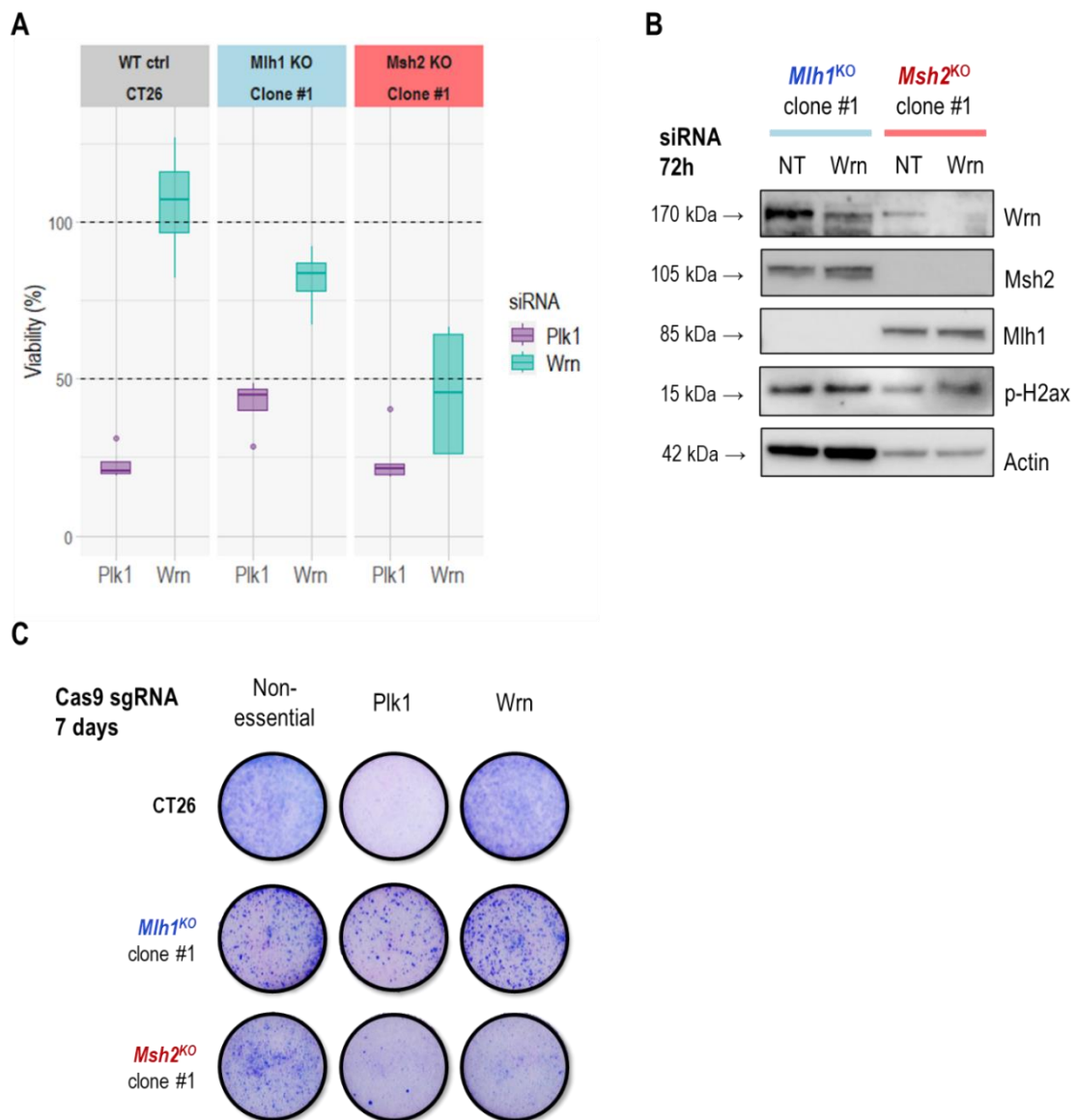
*Figure 32.* ***Evaluation of Wrn dependency in 2D cultures derived from MMRd Cas9-free clones.*** *A. Box plots showing sensitivity to Wrn silencing via RNA interference in cells from Mlh1 KO and Msh2 KO clones. Data were normalized to non-targeting control siRNA. CT26 colon carcinoma cell line was used as negative MSS control. Dashed lines indicate 50% and 100% viabilities to help the visualisation.* ***B.*** *Western blot analysis of Wrn, Msh2, Mlh1 and p-H2ax proteins in cells from Mlh1 KO and Msh2 KO clones at 72 hours since the transfection with non-targeting control and anti-Wrn siRNAs. Actin was used as loading control.* ***C.*** *Crystal violet staining on Cas9-pretransduced cells from Mlh1 KO and Msh2 KO clones at 7 days since the transduction with the virus for the expression of anti-Wrn sgRNAs. sgRNAs targeting a mouse non-essential gene (Cyp4f40) and mouse Plk1 were used as negative and positive controls, respectively. CT26 cell line was used as negative MSS control.*

**DISCUSSION**

In recent years, gastric cancer with microsatellite instability emerged as a well-defined entity endowed with a high mutational load and a good prognosis. MSI GC has been also associated with a negative response to postoperative chemotherapy and a positive response to ICIs in every treatment line. However, the significant degree of clinical heterogeneity observed in GC cases poses a critical challenge for accurate patient stratification and treatment decisions. Immunocompetent MSI GC mouse models could be a valuable tool to get more insights into the molecular complexity of the disease, allowing the study of tumour development/progression and responses to treatments in the presence of a fully functional immune system.

In the frame of my PhD project, starting from non-transformed BALB/c gastric epithelial cells, we successfully generated syngeneic *Mlh1* KO and *Msh2* KO mouse cultures. The obtained MMR-deficient models, but not the WT counterparts, developed microsatellite instability and increased their mutation rate over time. Results from *in vivo* experiments performed by injecting bulk lines provide proof-of-concept of the tumorigenic potential of MMR impairment. When stably grown in stringent conditions, MMRd but not WT cells were indeed able to generate tumour masses upon subcutaneous injection in immunodeficient NOD SCID mice. Importantly, we also optimised the gene editing protocol to obtain Cas9-non-expressing clones, suitable for injection in BALB/c immunocompetent mice.

The model we have developed could stand out as a one-of-a-kind addition in the landscape of murine GC models, as we induced neoplastic transformation affecting MMR system function without simultaneously genetically altering any known oncogene or tumour suppressor gene, thus allowing the natural emergence of driver mutations. The only alternative immunocompetent MSI GC mouse model published to date was indeed generated via targeted

ablation of *Msh2* gene in a *Tpr53* KO background (139). Moreover, similar strategies have been adopted to generate mouse models mimicking sporadic MMR impairment in other tissue types. A recently published article describes autochthonous C57BL/6 lung cancer and colon cancer models, in which MMR deficiency and the subsequent tumorigenesis were induced through a conditional knockout of an MMR gene, together with the inactivation of a tumour suppressor gene (*Trp53* for lung cancer and *Apc* for colon cancer) (173). Other authors have generated syngeneic MSI tumour models inactivating a key MMR gene *in vitro* in the context of microsatellite stable cancer cell lines, such as CT26 mouse colon carcinoma and B16F10 mouse melanoma, to generate novel MMR-deficient derivatives (174,175).

In order to obtain a good representation of MSI GC cases, we generated two different MMRd genotypes, ablating either *Mlh1* or *Msh2* genes in BALB/c gastric organoids, thus affecting the function of MutL and MutS complexes, respectively. MMRd organoids, but not the WT control, resulted in the acquisition of microsatellite instability in 3-6 months, in line with findings from prior studies in which authors induced MMR deficiency in mouse MSS cancer cell lines (174,175). Furthermore, *Mlh1* KO organoids acquired MSI earlier than *Msh2* KO organoids, while *Msh2* inactivation favoured a greater accumulation of mutations at 10 months of culture since the knockout event. This data is in line with a study performed on 1057 MSI-H solid tumours in which TMB was examined and related to the IHC staining of the main MMR proteins. In the analysed cohort, the loss of MSH2/MSH6 heterodimer was less common than the loss of MLH1/PMS2, but it was associated with a higher mean TMB (46.83 vs 25.03 mutations/Mb) (176).

Even if MMRd organoid cultures displayed MSI and a high TMB, they were not able to generate tumours upon injection in immunocompromised NOD SCID mice. However, importantly, when we grew them as 2D cultures without any scaffold matrix and in a commercial medium deprived of all the specific growth factors present in the organoid medium,

MMRd models, but not WT controls, formed tumour masses in the tumorigenesis experiments upon injection in mice. Given the pathogenetic role of MMR system alterations in hereditary cancer syndromes and the presence of MSI in pre-cancerous lesions (50,164–166), it is evident that the MMR system plays a crucial anti-tumour role and that MMR impairment *per se* is predisposing cells to a higher risk of neoplastic transformation. Nevertheless, additional genetic and epigenetic scars and/or wide cell reprogramming may be necessary for the acquisition of a fully malignant phenotype. Cancer is indeed considered the result of a multistep process guided by a dynamic interplay between the initiating driver genetic and epigenetic alterations and the environment. Consistently with this theory, tumour development usually includes a long latency period (even decades in some cases) between the initiating oncogenic insult and the appearance of a clinically detectable tumour (177). Some alterations, even if highly penetrant, need pressure to become effective and may confer a selective advantage only in the appropriate cellular/environmental context. The susceptibility to malignant transformation is influenced by cell plasticity and differentiation stage (170). A high level of cellular differentiation typically serves as a protective barrier against tumorigenesis and the microenvironment is believed to play a role in cellular reprogramming during the initial stages of tumorigenesis, facilitating the emergence of cellular states that are more prone to malignant transformation (178). Taking these considerations into account, we tried to change the culture conditions as the setting in which we were growing non-transformed organoids may not imply any major selective bottleneck able to force the cells towards a complete neoplastic transformation in a time frame compatible with experimental requirements. We are aware that this is a crucial point in the development of our MSI GC models and we have not clarified yet the mechanisms guiding the acquisition of a malignant phenotype following the change in culture conditions. When we passed from 3D to 2D culture more than a single variable changed and both the bioscaffold removal and the change in medium composition could potentially have had an impact. Further

experiments are required to identify the key environmental factors promoting tumorigenesis in our models.

We managed to obtain tumour masses in NOD SCID mice from both the MMRd genotypes, although they exhibited differences in engraftment rates and growth dynamics. All *Mlh1* KO 2D cultures were able to form tumours with very high engraftment rates (80-100%), while *Msh2* KO cells derived from non-irradiated organoids (cell series 3) showed a relatively limited tumorigenic potential (25-30% engraftment rate). Despite that, when comparing cells which originated in the same experimental conditions and displayed similar engraftment rates (such as the cells derived from irradiated organoids from series 2 or those from series 3), *Msh2* KO models exhibited more rapid growth dynamics compared to their *Mlh1* KO counterparts. Given the limited number of conducted experiments, we cannot assert definitive conclusions about the different tumorigenic potentials associated with the loss of Mlh1 or Msh2. However, in our specific experimental context, while the ablation of Mlh1 caused tumours in nearly all mice, *Msh2* KO tumours tended to exhibit more aggressive behaviour. In addition to a faster growth rate, it is worth noting that only in the case of the *Msh2* KO genotype we also observed alterations in cell morphology, leading to the acquisition of a mesenchymal phenotype (*Msh2* KO cells from series 1). Nonetheless, it is still possible that these observations are the result of the stochastic nature of cancer evolution, which occurred independently in each cellular model. It is plausible that these differences are due not only to the initial event that caused MMR deficiency but perhaps more prominently to the subsequent specific driver lesions that emerged within the context of the genetic instability.

Another factor that has had a significant impact on the results from *in vivo* tumorigenesis experiments is certainly ionizing radiation. Although irradiation is not a crucial step for the acquisition of a cancer phenotype in our models (as we also obtained tumour masses by injecting cells that had never been irradiated), X-rays facilitated the neoplastic transformation,

as expected. Irradiated MMRd cells formed tumours in a larger proportion of NOD SCID mice compared to non-irradiated cells. Importantly, they were also the only bulk models that managed to form relatively large tumour masses ($>500$ mm$^3$) upon injection in immunocompetent BALB/c mice. At the employed dosage (0.5 Gy), X-rays did not exhibit any immediate evident impact on cell viability, but they may have induced DNA damage, potentially prompting the acquisition of additional genetic scars.

The stark contrast in tumorigenesis outcomes between 3D and 2D MMRd gastric cultures is not attributable to differences in the MSI degree or the mutational load. Differential gene expression analysis uncovered the substantial transcriptional reprogramming induced by the change in culture conditions, resulting in over 3000 significantly differentially expressed genes. According to GSEA, tumorigenic MMRd cells and cells retrieved from tumour masses showed an increase in the activity of mitogenic signalling pathways (E2F and MYC targets, cell cycle, G2M checkpoint and mitotic spindle genes), but also an unexpected metabolic reprogramming, apparently implying the downregulations of genes involved in glycolysis and gluconeogenesis. Notably, the aldolase C enzyme (*Aldoc*) was strongly downregulated in 2D cultures compared to organoids. Several studies explored the role of aldolase family members in tumorigenesis and cancer progression, but the role of ALDOC is quite controversial. According to many reports, ALDOC overexpression promotes tumorigenesis in several tissues, including brain, kidney and lung, and it is closely associated with poor outcome in breast cancer (179). However, some investigators found *ALDOC* mRNA expression significantly reduced in high-grade glioblastoma, compared to low-grade glioma and normal brain tissue. Furthermore, in glioblastoma, ALDOC downregulation was also associated with a poor outcome (180). A recently published article described ALDOC overexpression in GC cells and tissues compared to normal tissues and associated ALDOC high levels with a poor prognosis. However, a meticulous examination of the study revealed that this overexpression emerges at protein, but

not at mRNA level. Since ALDOC expression was also positively correlated with immune infiltration, the authors proposed ALDOC as a potential biomarker to predict the response to anti-PD-1 ICIs (179). Even though ALDOC is presumed to play a role in tumour progression, some other data from the literature suggest that, in our specific experimental setting, its regulation may be caused by the change in culture modalities rather than being directly linked to tumour progression. Some studies indeed associated overexpression of ALDOC and other glycolytic enzymes with 3D-culture conditions (181,182).

We also conducted mutational profiling to better characterise MMRd cells retrieved from tumour masses. We demonstrated that different 2D derivations gave origin to models sharing a relatively small subset of mutations and thus diverging in their genetic evolution. We also observed that MMRd cells were able to recapitulate at least in part the human MSI GC mutational landscape. Genes mutated in our MMRd models include indeed genes commonly associated with the MSI subgroup, such as *Kras, Arid1a, Erbb3 and Tpr53*. In Cas9-free *Mlh1* KO clone #1, we were able to find a hotspot *Kras* mutation (G12D). In line with the mutational profile, this Cas9-free clone exhibited an aggressive phenotype in the *in vivo* tumorigenesis experiments, demonstrating remarkably rapid growth dynamics (tumour masses reached volumes over 1500 mm$^3$ in 15 days from injection).

These findings demonstrate that our mouse MMRd cultures have the potential to effectively model MSI GCs, presenting key molecular features, like microsatellite instability and a high tumour mutational burden, and capturing some of the alterations commonly observed in human tumours. Importantly, the heterogeneity observed in the models generated so far, though limited in number, suggests that with multiple clonal populations we will be able to accurately reconstruct the GC MSI molecular universe. However, we are aware of the limitations of the model, as the inactivation of *Mlh1* and *Msh2* genes potentially recapitulates a good portion of MSI cases, but not all of them. The chosen genotypes are unable to mimic the rarer cases in

which the MMR deficiency is due to other members of the system. An IHC analysis of 585 MMRd tumours revealed that over 15% of cases can be classified as unusual MMRd tumours as they harboured isolated loss of PMS2 and/or MSH6 proteins or retained the staining of the four main MMR proteins (183). Some critical issues are also related to the intrinsic differences between human and mouse genomes. For example, in a recent study, a notable prevalence of subclonal variants in *Msh6* and *Msh3* genes was underscored in the context of MSI CRCs. These mutations primarily cluster in two specific hotspot regions. These regions consist of repetitive homopolymer sequences which, in the context of the genetic instability induced by the loss of Mlh1, become particularly susceptible to frameshift alterations. Importantly, subclonal secondary MMR alterations fuel intratumour heterogeneity affecting tumour immunogenicity (121). We are aware that our model is not able to recapitulate secondary hotspot alterations in *Msh6* and *Msh3* due to the lack of homopolymeric tracts in the mouse genes.

Our models possess also significant advantages, particularly in their ability to grow in immunocompetent BALB/c mice. Conducting a direct comparison between tumour masses arisen in immunocompetent and immunodeficient mice may serve as a potent strategy for investigating immune evasion mechanisms. Through the comparative analysis conducted on cells retrieved from tumours originating from *Mlh1* KO clone #1, some differentially expressed genes emerged. One of them *Vgll3*, significantly downregulated in cells retrieved from BALB/c mice, has been previously correlated with immune cell infiltration in GC (184).

Another point in favour of the efficacy of our models lies in their ability to recapitulate another pivotal feature of MSI tumours. WRN dependency has emerged as a promising specific vulnerability, with the potential to significantly improve the therapeutic landscape of this molecular subtype. WRN has indeed been described as a promising drug target also in MSI cases recurring after targeted therapies, chemotherapy and immunotherapy (126). Notably,

among the MMRd clones tested for Wrn dependency, we were able to identify an *Msh2* KO

clone whose viability was affected by Wrn knockdown.

**FUTURE PERSPECTIVES**

We successfully generated MMRd tumorigenic cells and characterized them from a molecular perspective, including transcriptional profiling and analysis of somatic alterations. However, our mutational analysis only focused on single-base substitutions and small indels, given their primary association with MSI. We believe that an intriguing opportunity for future research could lie in exploring additional types of genomic alterations (such as copy number variations, structural variants, and epigenetic events) that may potentially occur during MSI GC tumorigenesis. To achieve this goal, we could expand the characterization of our models by means of whole genome sequencing and/or epigenomic assays (such as ChIP-Seq, ATAC-Seq, Hi-C, DNA methylation analysis, chromatin accessibility assays, histone modification analysis).

From a clinical point of view, MSI subgroup is usually associated with a good prognosis. However, some reports showed the existence of a subpopulation of MSI GC patients displaying a worse outcome (117,118). The analysis of transcriptional profiles to potentially identify these two MSI subgroups in our models could serve as a valuable benchmark, along with the mutational analysis, for assessing the representativeness of our cohort.

Our models could contribute to assessing the mechanisms underlying the clinical heterogeneity of MSI GC, as the molecular characterisation of the most invasive/aggressive clones could lead to the identification of putative prognostic markers useful for patient stratification. Although relatively few MSI cases develop metastatic disease (2-5%) (26), it would be important to identify them early based on their molecular features.

Future efforts will be also directed towards a further improvement of the model to partially overcome its limitations. One possibility is the expansion of the considered genotypes, also

including the inactivation of *Pms2* and *Msh6*, to mimic rarer MSI GCs. Furthermore, in order to replicate some facets of the intratumoral molecular heterogeneity, we are currently planning the introduction of secondary alterations in the MutS complex (*Msh2, Msh6, Msh3* genes) in the context of a complete Mlh1 loss. We are also generating proper control clones, transduced with the empty sgRNA vector.

To fully exploit the potential of the model, it will be crucial to evaluate the growth patterns of several clones in the presence and absence of the immune system. Furthermore, testing immunotherapy in immunocompetent BALB/c mice will be of paramount importance. Our model provides an optimal experimental setting for examining the interplay of ICIs with alternative therapeutic strategies (e.g. WRN inhibitors). It could also serve as a platform to pinpoint potential mechanisms of primary and secondary resistance to immunotherapy regimens currently approved in the clinical practice.

# BIBLIOGRAPHY

1.  Sung H, Ferlay J, Siegel RL, Laversanne M, Soerjomataram I, Jemal A, et al. Global Cancer Statistics 2020: GLOBOCAN Estimates of Incidence and Mortality Worldwide for 36 Cancers in 185 Countries. CA Cancer J Clin. 2021;71:209–49.

2.  Thrift AP, El-Serag HB. Burden of Gastric Cancer. Clin Gastroenterol Hepatol. Elsevier; 2020;18:534–42.

3.  Guilford P, Hopkins J, Harraway J, McLeod M, McLeod N, Harawira P, et al. E-cadherin germline mutations in familial gastric cancer. Nature. Nature Publishing Group; 1998;392:402–5.

4.  Majewski IJ, Kluijt I, Cats A, Scerri TS, de Jong D, Kluin RJ, et al. An α-E-catenin (CTNNA1) mutation in hereditary diffuse gastric cancer. J Pathol. 2013;229:621–9.

5.  Masciari S, Dewanwala A, Stoffel EM, Lauwers GY, Zheng H, Achatz MI, et al. Gastric cancer in individuals with Li-Fraumeni syndrome. Genet Med Off J Am Coll Med Genet. 2011;13:651–7.

6.  van Lier MGF, Wagner A, Mathus-Vliegen EMH, Kuipers EJ, Steyerberg EW, van Leerdam ME. High cancer risk in Peutz-Jeghers syndrome: a systematic review and surveillance recommendations. Am J Gastroenterol. 2010;105:1258–64; author reply 1265.

7.  Buckley KH, Niccum BA, Maxwell KN, Katona BW. Gastric Cancer Risk and Pathogenesis in BRCA1 and BRCA2 Carriers. Cancers. 2022;14:5953.

8.  Plummer M, Franceschi S, Vignat J, Forman D, de Martel C. Global burden of gastric cancer attributable to Helicobacter pylori. Int J Cancer. 2015;136:487–90.

9.  Li Y, Choi H, Leung K, Jiang F, Graham DY, Leung WK. Global prevalence of Helicobacter pylori infection between 1980 and 2022: a systematic review and meta-analysis. Lancet Gastroenterol Hepatol. Elsevier; 2023;8:553–64.

10. Guan W-L, He Y, Xu R-H. Gastric cancer treatment: recent progress and future perspectives. J Hematol OncolJ Hematol Oncol. 2023;16:57.

11. Stomach Cancer Survival Rates and Statistics - NCI [Internet]. 2023 [cited 2023 Sep 24]. Available from: https://www.cancer.gov/types/stomach/survival

12. Stomach (Gastric) Cancer Survival Rates [Internet]. [cited 2023 Sep 24]. Available from: https://www.cancer.org/cancer/types/stomach-cancer/detection-diagnosis-staging/survival-rates.html

13. Cunningham D, Allum WH, Stenning SP, Thompson JN, Van de Velde CJH, Nicolson M, et al. Perioperative chemotherapy versus surgery alone for resectable gastroesophageal cancer. N Engl J Med. 2006;355:11–20.

14. Lordick F, Carneiro F, Cascinu S, Fleitas T, Haustermans K, Piessen G, et al. Gastric cancer: ESMO Clinical Practice Guideline for diagnosis, treatment and follow-up. Ann Oncol Off J Eur Soc Med Oncol. 2022;33:1005–20.

15. Al-Batran S-E, Homann N, Pauligk C, Goetze TO, Meiler J, Kasper S, et al. Perioperative chemotherapy with fluorouracil plus leucovorin, oxaliplatin, and docetaxel versus fluorouracil or capecitabine plus cisplatin and epirubicin for locally advanced, resectable gastric or gastro-oesophageal junction adenocarcinoma (FLOT4): a randomised, phase 2/3 trial. Lancet Lond Engl. 2019;393:1948–57.

16. Sasako M, Sakuramoto S, Katai H, Kinoshita T, Furukawa H, Yamaguchi T, et al. Five-year outcomes of a randomized phase III trial comparing adjuvant chemotherapy with S-1 versus surgery alone in stage II or III gastric cancer. J Clin Oncol Off J Am Soc Clin Oncol. 2011;29:4387–93.

17. Yoshida K, Kodera Y, Kochi M, Ichikawa W, Kakeji Y, Sano T, et al. Addition of Docetaxel to Oral Fluoropyrimidine Improves Efficacy in Patients With Stage III Gastric Cancer: Interim Analysis of JACCRO GC-07, a Randomized Controlled Trial. J Clin Oncol Off J Am Soc Clin Oncol. 2019;37:1296–304.

18. Zhang X, Liang H, Li Z, Xue Y, Wang Y, Zhou Z, et al. Perioperative or postoperative adjuvant oxaliplatin with S-1 versus adjuvant oxaliplatin with capecitabine in patients with locally advanced gastric or gastro-oesophageal junction adenocarcinoma undergoing D2 gastrectomy (RESOLVE): an open-label, superiority and non-inferiority, phase 3 randomised controlled trial. Lancet Oncol. 2021;22:1081–92.

19. Bang Y-J, Van Cutsem E, Feyereislova A, Chung HC, Shen L, Sawaki A, et al. Trastuzumab in combination with chemotherapy versus chemotherapy alone for treatment of HER2-positive advanced gastric or gastro-oesophageal junction cancer (ToGA): a phase 3, open-label, randomised controlled trial. Lancet Lond Engl. 2010;376:687–97.

20. Barok M, Joensuu H, Isola J. Trastuzumab emtansine: mechanisms of action and drug resistance. Breast Cancer Res. 2014;16:209.

21. Ogitani Y, Aida T, Hagihara K, Yamaguchi J, Ishii C, Harada N, et al. DS-8201a, A Novel HER2-Targeting ADC with a Novel DNA Topoisomerase I Inhibitor, Demonstrates a Promising Antitumor Efficacy with Differentiation from T-DM1. Clin Cancer Res. 2016;22:5097–108.

22. Shitara K, Bang Y-J, Iwasa S, Sugimoto N, Ryu M-H, Sakai D, et al. Trastuzumab Deruxtecan in Previously Treated HER2-Positive Gastric Cancer. N Engl J Med. 2020;382:2419–30.

23. Cutsem EV, Bartolomeo M di, Smyth E, Chau I, Park H, Siena S, et al. Trastuzumab deruxtecan in patients in the USA and Europe with HER2-positive advanced gastric or gastroesophageal junction cancer with disease progression on or after a trastuzumab-containing regimen (DESTINY-Gastric02): primary and updated analyses from a single-arm, phase 2 study. Lancet Oncol. Elsevier; 2023;24:744–56.

24. Fuchs CS, Tomasek J, Yong CJ, Dumitru F, Passalacqua R, Goswami C, et al. Ramucirumab monotherapy for previously treated advanced gastric or gastro-oesophageal junction adenocarcinoma (REGARD): an international, randomised, multicentre, placebo-controlled, phase 3 trial. Lancet Lond Engl. 2014;383:31–9.

25. Wilke H, Muro K, Van Cutsem E, Oh S-C, Bodoky G, Shimada Y, et al. Ramucirumab plus paclitaxel versus placebo plus paclitaxel in patients with previously treated advanced gastric or gastro-oesophageal junction adenocarcinoma (RAINBOW): a double-blind, randomised phase 3 trial. Lancet Oncol. 2014;15:1224–35.

26. Fuchs CS, Doi T, Jang RW, Muro K, Satoh T, Machado M, et al. Safety and Efficacy of Pembrolizumab Monotherapy in Patients With Previously Treated Advanced Gastric and

Gastroesophageal Junction Cancer: Phase 2 Clinical KEYNOTE-059 Trial. JAMA Oncol. 2018;4:e180013.

27. Janjigian YY, Kawazoe A, Yañez P, Li N, Lonardi S, Kolesnik O, et al. The KEYNOTE-811 trial of dual PD-1 and HER2 blockade in HER2-positive gastric cancer. Nature. 2021;600:727–30.

28. EMA. Keytruda: Pending EC decision [Internet]. Eur. Med. Agency. 2023 [cited 2023 Sep 24]. Available from: https://www.ema.europa.eu/en/medicines/human/summaries-opinion/keytruda

29. Janjigian YY, Shitara K, Moehler M, Garrido M, Salman P, Shen L, et al. First-line nivolumab plus chemotherapy versus chemotherapy alone for advanced gastric, gastro-oesophageal junction, and oesophageal adenocarcinoma (CheckMate 649): a randomised, open-label, phase 3 trial. Lancet Lond Engl. 2021;398:27–40.

30. Nagini S. Carcinoma of the stomach: A review of epidemiology, pathogenesis, molecular genetics and chemoprevention. World J Gastrointest Oncol. 2012;4:156–69.

31. Lauren P. THE TWO HISTOLOGICAL MAIN TYPES OF GASTRIC CARCINOMA: DIFFUSE AND SO-CALLED INTESTINAL-TYPE CARCINOMA. AN ATTEMPT AT A HISTO-CLINICAL CLASSIFICATION. Acta Pathol Microbiol Scand. 1965;64:31–49.

32. Fléjou J-F. [WHO Classification of digestive tumors: the fourth edition]. Ann Pathol. 2011;31:S27-31.

33. Guglielmi A, de Manzoni G, Tomezzoli A, Ricci F, Pelosi G, Laterza E, et al. [Prognostic value of histologic classifications of advanced stomach cancer: comparative study of Lauren's and Goseki's classifications]. Chir Ital. 1997;49:45–9.

34. Qiu M, Cai M, Zhang D, Wang Z, Wang D, Li Y, et al. Clinicopathological characteristics and prognostic analysis of Lauren classification in gastric adenocarcinoma in China. J Transl Med. 2013;11:58.

35. Garnier P, Vielh P, Asselain B, Durand JC, Girodet J, Pilleron JP, et al. [Prognostic value of the Lauren and Ming classifications in gastric adenocarcinoma. Multidimensional analysis]. Gastroenterol Clin Biol. 1988;12:553–8.

36. Calli Demirkan N, Tunçyürek M, Ugur Ertan E, Bülent Alkanat M, Içöz G. [Correlation of histological classifications of gastric carcinomas with location and prognosis]. Gastroenterol Clin Biol. 2002;26:610–5.

37. Mönig S, Baldus SE, Collet PH, Zirbes TK, Bollschweiler E, Thiele J, et al. Histological grading in gastric cancer by Goseki classification: correlation with histopathological subtypes and prognosis. Anticancer Res. 2001;21:617–20.

38. Ribeiro MM, Sarmento JA, Sobrinho Simões MA, Bastos J. Prognostic significance of Lauren and Ming classifications and other pathologic parameters in gastric carcinoma. Cancer. 1981;47:780–4.

39. Zheng H, Zheng Y, Xia P, Xu X, Xing Y, Takahashi H, et al. The pathobiological behaviors and prognosis associated with Japanese gastric adenocarcinomas of pure WHO histological subtypes. Histol Histopathol. 2010;25:445–52.

40. Hass HG, Smith U, Jäger C, Schäffer M, Wellhäuber U, Hehr T, et al. Signet ring cell carcinoma of the stomach is significantly associated with poor prognosis and diffuse gastric cancer (Lauren's): single-center experience of 160 cases. Onkologie. 2011;34:682–6.

41. Taghavi S, Jayarajan SN, Davey A, Willis AI. Prognostic significance of signet ring gastric cancer. J Clin Oncol Off J Am Soc Clin Oncol. 2012;30:3493–8.

42. Corso S, Giordano S. How Can Gastric Cancer Molecular Profiling Guide Future Therapies? Trends Mol Med. 2016;22:534–44.

43. Bass AJ, Thorsson V, Shmulevich I, Reynolds SM, Miller M, Bernard B, et al. Comprehensive molecular characterization of gastric adenocarcinoma. Nature. Nature Publishing Group; 2014;513:202–9.

44. Cristescu R, Lee J, Nebozhyn M, Kim K-M, Ting JC, Wong SS, et al. Molecular analysis of gastric cancer identifies subtypes associated with distinct clinical outcomes. Nat Med. Nature Publishing Group; 2015;21:449–56.

45. Liu X, Meltzer SJ. Gastric Cancer in the Era of Precision Medicine. Cell Mol Gastroenterol Hepatol. 2017;3:348–58.

46. Poh AR, O'Donoghue RJJ, Ernst M, Putoczki TL. Mouse models for gastric cancer: Matching models to biological questions. J Gastroenterol Hepatol. 2016;31:1257–72.

47. Baretti M, Le DT. DNA mismatch repair in cancer. Pharmacol Ther. 2018;189:45–62.

48. Liu D, Keijzers G, Rasmussen LJ. DNA mismatch repair and its many roles in eukaryotic cells. Mutat Res Rev Mutat Res. 2017;773:174–87.

49. Pećina-Šlaus N, Kafka A, Salamon I, Bukovac A. Mismatch Repair Pathway, Genome Stability and Cancer. Front Mol Biosci. 2020;7:122.

50. Biller LH, Syngal S, Yurgelun MB. Recent advances in Lynch syndrome. Fam Cancer. 2019;18:211–9.

51. Gallon R, Phelps R, Hayes C, Brugieres L, Guerrini-Rousseau L, Colas C, et al. Constitutional Microsatellite Instability, Genotype, and Phenotype Correlations in Constitutional Mismatch Repair Deficiency. Gastroenterology. 2023;164:579-592.e8.

52. Abedalthagafi M. Constitutional mismatch repair-deficiency: current problems and emerging therapeutic strategies. Oncotarget. 2018;9:35458–69.

53. Edwards P, Monahan KJ. Diagnosis and management of Lynch syndrome. Frontline Gastroenterol. British Medical Journal Publishing Group; 2022;13:e80–7.

54. Tabori U, Hansford JR, Achatz MI, Kratz CP, Plon SE, Frebourg T, et al. Clinical Management and Tumor Surveillance Recommendations of Inherited Mismatch Repair Deficiency in Childhood. Clin Cancer Res. 2017;23:e32–7.

55. Kumar S, Farha N, Burke CA, Katona BW. Upper Gastrointestinal Cancer Surveillance in Lynch Syndrome. Cancers. 2022;14:1000.

56. Weiss JM, Gupta S, Burke CA, Axell L, Chen L-M, Chung DC, et al. NCCN Guidelines® Insights: Genetic/Familial High-Risk Assessment: Colorectal, Version 1.2021. J Natl Compr Cancer Netw JNCCN. 2021;19:1122–32.

57. Monahan KJ, Bradshaw N, Dolwani S, Desouza B, Dunlop MG, East JE, et al. Guidelines for the management of hereditary colorectal cancer from the British Society of

Gastroenterology (BSG)/Association of Coloproctology of Great Britain and Ireland (ACPGBI)/United Kingdom Cancer Genetics Group (UKCGG). Gut. 2020;69:411–44.

58. Seppälä TT, Latchford A, Negoi I, Sampaio Soares A, Jimenez-Rodriguez R, Sánchez-Guillén L, et al. European guidelines from the EHTG and ESCP for Lynch syndrome: an updated third edition of the Mallorca guidelines based on gene and gender. Br J Surg. 2021;108:484–98.

59. Guastadisegni C, Colafranceschi M, Ottini L, Dogliotti E. Microsatellite instability as a marker of prognosis and response to therapy: a meta-analysis of colorectal cancer survival data. Eur J Cancer Oxf Engl 1990. 2010;46:2788–98.

60. Amato M, Franco R, Facchini G, Addeo R, Ciardiello F, Berretta M, et al. Microsatellite Instability: From the Implementation of the Detection to a Prognostic and Predictive Role in Cancers. Int J Mol Sci. 2022;23:8726.

61. Bonneville R, Krook MA, Kautto EA, Miya J, Wing MR, Chen H-Z, et al. Landscape of Microsatellite Instability Across 39 Cancer Types. JCO Precis Oncol. 2017;2017:PO.17.00073.

62. Suraweera N, Duval A, Reperant M, Vaury C, Furlan D, Leroy K, et al. Evaluation of tumor microsatellite instability using five quasimonomorphic mononucleotide repeats and pentaplex PCR. Gastroenterology. 2002;123:1804–11.

63. Campanella NC, Berardinelli GN, Scapulatempo-Neto C, Viana D, Palmero EI, Pereira R, et al. Optimization of a pentaplex panel for MSI analysis without control DNA in a Brazilian population: correlation with ancestry markers. Eur J Hum Genet EJHG. 2014;22:875–80.

64. Murphy KM, Zhang S, Geiger T, Hafez MJ, Bacher J, Berg KD, et al. Comparison of the microsatellite instability analysis system and the Bethesda panel for the determination of microsatellite instability in colorectal cancers. J Mol Diagn JMD. 2006;8:305–11.

65. Umar A, Risinger JI, Hawk ET, Barrett JC. Testing guidelines for hereditary non-polyposis colorectal cancer. Nat Rev Cancer. 2004;4:153–8.

66. Hempelmann JA, Scroggins SM, Pritchard CC, Salipante SJ. MSIplus for Integrated Colorectal Cancer Molecular Testing by Next-Generation Sequencing. J Mol Diagn JMD. 2015;17:705–14.

67. Pritchard CC, Smith C, Salipante SJ, Lee MK, Thornton AM, Nord AS, et al. ColoSeq Provides Comprehensive Lynch and Polyposis Syndrome Mutational Analysis Using Massively Parallel Sequencing. J Mol Diagn JMD. 2012;14:357–66.

68. Salipante SJ, Scroggins SM, Hampel HL, Turner EH, Pritchard CC. Microsatellite instability detection by next generation sequencing. Clin Chem. 2014;60:1192–9.

69. Middha S, Zhang L, Nafa K, Jayakumaran G, Wong D, Kim HR, et al. Reliable Pan-Cancer Microsatellite Instability Assessment by Using Targeted Next-Generation Sequencing Data. JCO Precis Oncol. 2017;2017:PO.17.00084.

70. Hause RJ, Pritchard CC, Shendure J, Salipante SJ. Classification and characterization of microsatellite instability across 18 cancer types. Nat Med. 2016;22:1342–50.

71. Kautto EA, Bonneville R, Miya J, Yu L, Krook MA, Reeser JW, et al. Performance evaluation for rapid detection of pan-cancer microsatellite instability with MANTIS. Oncotarget. 2017;8:7452–63.

72. Aaltonen LA, Abascal F, Abeshouse A, Aburatani H, Adams DJ, Agrawal N, et al. Pan-cancer analysis of whole genomes. Nature. Nature Publishing Group; 2020;578:82–93.

73. COSMIC | Mutational Signatures [Internet]. [cited 2023 Dec 28]. Available from: https://cancer.sanger.ac.uk/signatures/

74. Klingbiel D, Saridaki Z, Roth AD, Bosman FT, Delorenzi M, Tejpar S. Prognosis of stage II and III colon cancer treated with adjuvant 5-fluorouracil or FOLFIRI in relation to microsatellite status: results of the PETACC-3 trial. Ann Oncol Off J Eur Soc Med Oncol. 2015;26:126–32.

75. Koncina E, Haan S, Rauh S, Letellier E. Prognostic and Predictive Molecular Biomarkers for Colorectal Cancer: Updates and Challenges. Cancers. 2020;12:319.

76. Dutta S, Ganguly A, Chatterjee K, Spada S, Mukherjee S. Targets of Immune Escape Mechanisms in Cancer: Basis for Development and Evolution of Cancer Immune

Checkpoint Inhibitors. Biology. Multidisciplinary Digital Publishing Institute; 2023;12:218.

77. Hodi FS, O'Day SJ, McDermott DF, Weber RW, Sosman JA, Haanen JB, et al. Improved Survival with Ipilimumab in Patients with Metastatic Melanoma. N Engl J Med. Massachusetts Medical Society; 2010;363:711–23.

78. Schadendorf D, Hodi FS, Robert C, Weber JS, Margolin K, Hamid O, et al. Pooled Analysis of Long-Term Survival Data From Phase II and Phase III Trials of Ipilimumab in Unresectable or Metastatic Melanoma. J Clin Oncol Off J Am Soc Clin Oncol. 2015;33:1889–94.

79. Garon EB, Rizvi NA, Hui R, Leighl N, Balmanoukian AS, Eder JP, et al. Pembrolizumab for the Treatment of Non–Small-Cell Lung Cancer. N Engl J Med. Massachusetts Medical Society; 2015;372:2018–28.

80. Borghaei H, Paz-Ares L, Horn L, Spigel DR, Steins M, Ready NE, et al. Nivolumab versus Docetaxel in Advanced Nonsquamous Non-Small-Cell Lung Cancer. N Engl J Med. 2015;373:1627–39.

81. Rizvi NA, Hellmann MD, Snyder A, Kvistborg P, Makarov V, Havel JJ, et al. Cancer immunology. Mutational landscape determines sensitivity to PD-1 blockade in non-small cell lung cancer. Science. 2015;348:124–8.

82. Topalian SL, Hodi FS, Brahmer JR, Gettinger SN, Smith DC, McDermott DF, et al. Safety, Activity, and Immune Correlates of Anti–PD-1 Antibody in Cancer. N Engl J Med. Massachusetts Medical Society; 2012;366:2443–54.

83. Le DT, Durham JN, Smith KN, Wang H, Bartlett BR, Aulakh LK, et al. Mismatch repair deficiency predicts response of solid tumors to PD-1 blockade. Science. 2017;357:409–13.

84. Overman MJ, McDermott R, Leach JL, Lonardi S, Lenz H-J, Morse MA, et al. Nivolumab in patients with metastatic DNA mismatch repair-deficient or microsatellite instability-high colorectal cancer (CheckMate 142): an open-label, multicentre, phase 2 study. Lancet Oncol. 2017;18:1182–91.

85. Shan J, Han D, Shen C, Lei Q, Zhang Y. Mechanism and strategies of immunotherapy resistance in colorectal cancer. Front Immunol. 2022;13:1016646.

86. Sahin IH, Zhang J, Saridogan T, Gorantla V, Rhree J, Malhotra M, et al. Neoadjuvant Immune Checkpoint Inhibitor Therapy for Patients With Microsatellite Instability-High Colorectal Cancer: Shedding Light on the Future. JCO Oncol Pract. 2023;19:251–9.

87. Shimozaki K, Nakayama I, Hirota T, Yamaguchi K. Current Strategy to Treat Immunogenic Gastrointestinal Cancers: Perspectives for a New Era. Cells. Multidisciplinary Digital Publishing Institute; 2023;12:1049.

88. Fattahi S, Amjadi-Moheb F, Tabaripour R, Ashrafi GH, Akhavan-Niaki H. PI3K/AKT/mTOR signaling in gastric cancer: Epigenetics and beyond. Life Sci. 2020;262:118513.

89. Barbi S, Cataldo I, De Manzoni G, Bersani S, Lamba S, Mattuzzi S, et al. The analysis of PIK3CA mutations in gastric carcinoma and metanalysis of literature suggest that exon-selectivity is a signature of cancer type. J Exp Clin Cancer Res CR. 2010;29:32.

90. Polom K, Marrelli D, Roviello G, Pascale V, Voglino C, Vindigni C, et al. PIK3CA mutation in gastric cancer and the role of microsatellite instability status in mutations of exons 9 and 20 of the PIK3CA gene. Adv Clin Exp Med Off Organ Wroclaw Med Univ. 2018;27:963–9.

91. Polom K, Das K, Marrelli D, Roviello G, Pascale V, Voglino C, et al. KRAS Mutation in Gastric Cancer and Prognostication Associated with Microsatellite Instability Status. Pathol Oncol Res POR. 2019;25:333–40.

92. van Grieken NCT, Aoyama T, Chambers PA, Bottomley D, Ward LC, Inam I, et al. KRAS and BRAF mutations are rare and related to DNA mismatch repair deficiency in gastric cancer from the East and the West: results from a large international multicentre study. Br J Cancer. 2013;108:1495–501.

93. Wang K, Kan J, Yuen ST, Shi ST, Chu KM, Law S, et al. Exome sequencing identifies frequent mutation of ARID1A in molecular subtypes of gastric cancer. Nat Genet. 2011;43:1219–23.

94. Zang ZJ, Cutcutache I, Poon SL, Zhang SL, McPherson JR, Tao J, et al. Exome sequencing of gastric adenocarcinoma identifies recurrent somatic mutations in cell adhesion and chromatin remodeling genes. Nat Genet. Nature Publishing Group; 2012;44:570–4.

95. Muzny DM, Bainbridge MN, Chang K, Dinh HH, Drummond JA, Fowler G, et al. Comprehensive molecular characterization of human colon and rectal cancer. Nature. Nature Publishing Group; 2012;487:330–7.

96. Yu P, Wang Y, Yu Y, Wang A, Huang L, Zhang Y, et al. Deep Targeted Sequencing and Its Potential Implication for Cancer Therapy in Chinese Patients with Gastric Adenocarcinoma. The Oncologist. 2021;26:e756–68.

97. Kim Y-S, Jeong H, Choi J-W, Oh HE, Lee J-H. Unique characteristics of ARID1A mutation and protein level in gastric and colorectal cancer: A meta-analysis. Saudi J Gastroenterol Off J Saudi Gastroenterol Assoc. 2017;23:268–74.

98. Ashizawa M, Saito M, Min AKT, Ujiie D, Saito K, Sato T, et al. Prognostic role of ARID1A negative expression in gastric cancer. Sci Rep. Nature Publishing Group; 2019;9:6769.

99. Bernal M, Ruiz-Cabello F, Concha A, Paschen A, Garrido F. Implication of the β2-microglobulin gene in the generation of tumor escape phenotypes. Cancer Immunol Immunother CII. 2012;61:1359–71.

100. Leone P, Shin E-C, Perosa F, Vacca A, Dammacco F, Racanelli V. MHC class I antigen processing and presenting machinery: organization, function, and defects in tumor cells. J Natl Cancer Inst. 2013;105:1172–87.

101. Polom K, Marano L, Marrelli D, De Luca R, Roviello G, Savelli V, et al. Meta-analysis of microsatellite instability in relation to clinicopathological characteristics and overall survival in gastric cancer. Br J Surg. 2018;105:159–67.

102. Miceli R, An J, Di Bartolomeo M, Morano F, Kim ST, Park SH, et al. Prognostic Impact of Microsatellite Instability in Asian Gastric Cancer Patients Enrolled in the ARTIST Trial. Oncology. 2019;97:38–43.

103. Di Bartolomeo M, Morano F, Raimondi A, Miceli R, Corallo S, Tamborini E, et al. Prognostic and Predictive Value of Microsatellite Instability, Inflammatory Reaction and PD-L1 in Gastric Cancer Patients Treated with Either Adjuvant 5-FU/LV or Sequential FOLFIRI Followed by Cisplatin and Docetaxel: A Translational Analysis from the ITACA-S Trial. The Oncologist. 2020;25:e460–8.

104. Choi YY, Kim H, Shin S-J, Kim HY, Lee J, Yang H-K, et al. Microsatellite Instability and Programmed Cell Death-Ligand 1 Expression in Stage II/III Gastric Cancer: Post Hoc Analysis of the CLASSIC Randomized Controlled study. Ann Surg. 2019;270:309–16.

105. An JY, Kim H, Cheong J-H, Hyung WJ, Kim H, Noh SH. Microsatellite instability in sporadic gastric cancer: its prognostic role and guidance for 5-FU based chemotherapy after R0 resection. Int J Cancer. 2012;131:505–11.

106. Kim SY, Choi YY, An JY, Shin HB, Jo A, Choi H, et al. The benefit of microsatellite instability is attenuated by chemotherapy in stage II and stage III gastric cancer: Results from a large cohort with subgroup analyses. Int J Cancer. 2015;137:819–25.

107. Smyth EC, Wotherspoon A, Peckitt C, Gonzalez D, Hulkki-Wilson S, Eltahir Z, et al. Mismatch Repair Deficiency, Microsatellite Instability, and Survival: An Exploratory Analysis of the Medical Research Council Adjuvant Gastric Infusional Chemotherapy (MAGIC) Trial. JAMA Oncol. 2017;3:1197–203.

108. Pietrantonio F, Raimondi A, Choi YY, Kang W, Langley RE, Kim YW, et al. MSI-GC-01: Individual patient data (IPD) meta-analysis of microsatellite instability (MSI) and gastric cancer (GC) from four randomized clinical trials (RCTs). J Clin Oncol. Wolters Kluwer; 2019;37:66–66.

109. Puliga E, Corso S, Pietrantonio F, Giordano S. Microsatellite instability in Gastric Cancer: Between lights and shadows. Cancer Treat Rev. 2021;95:102175.

110. Liu Y, Hu P, Xu L, Zhang X, Li Z, Li Y, et al. Current Progress on Predictive Biomarkers for Response to Immune Checkpoint Inhibitors in Gastric Cancer: How to Maximize the Immunotherapeutic Benefit? Cancers. 2023;15:2273.

111. Kwak Y, Seo AN, Lee HE, Lee HS. Tumor immune response and immunotherapy in gastric cancer. J Pathol Transl Med. 2020;54:20–33.

112. Janjigian YY, Bendell J, Calvo E, Kim JW, Ascierto PA, Sharma P, et al. CheckMate-032 Study: Efficacy and Safety of Nivolumab and Nivolumab Plus Ipilimumab in Patients With Metastatic Esophagogastric Cancer. J Clin Oncol Off J Am Soc Clin Oncol. 2018;36:2836–44.

113. Pietrantonio F, Randon G, Di Bartolomeo M, Luciani A, Chao J, Smyth EC, et al. Predictive role of microsatellite instability for PD-1 blockade in patients with advanced gastric cancer: a meta-analysis of randomized clinical trials. ESMO Open. 2021;6:100036.

114. ESMO. EMA Recommends Extension of Indications for Pembrolizumab to MSI-H or dMMR Cancers and to Metastatic Cervical Cancer with PD-L1 CPS ≥1 [Internet]. [cited 2023 Sep 27]. Available from: https://www.esmo.org/oncology-news/ema-recommends-extension-of-indications-for-pembrolizumab-to-msi-h-or-dmmr-cancers-and-to-metastatic-cervical-cancer-with-pd-l1-cps-1

115. Samstein RM, Lee C-H, Shoushtari AN, Hellmann MD, Shen R, Janjigian YY, et al. Tumor mutational load predicts survival after immunotherapy across multiple cancer types. Nat Genet. 2019;51:202–6.

116. Shitara K, Özgüroğlu M, Bang Y-J, Di Bartolomeo M, Mandalà M, Ryu M, et al. The association of tissue tumor mutational burden (tTMB) using the Foundation Medicine genomic platform with efficacy of pembrolizumab versus paclitaxel in patients (pts) with gastric cancer (GC) from KEYNOTE-061. J Clin Oncol. Wolters Kluwer; 2020;38:4537–4537.

117. Corso S, Isella C, Bellomo SE, Apicella M, Durando S, Migliore C, et al. A Comprehensive PDX Gastric Cancer Collection Captures Cancer Cell-Intrinsic Transcriptional MSI Traits. Cancer Res. 2019;79:5884–96.

118. Yang Y, Shi Z, Bai R, Hu W. Heterogeneity of MSI-H gastric cancer identifies a subtype with worse survival. J Med Genet. BMJ Publishing Group Ltd; 2021;58:12–9.

119. Chao J, Fuchs CS, Shitara K, Tabernero J, Muro K, Van Cutsem E, et al. Pembrolizumab (pembro) in microsatellite instability-high (MSI-H) advanced gastric/gastroesophageal junction (G/GEJ) cancer by line of therapy. J Clin Oncol. Wolters Kluwer; 2020;38:430–430.

120.    Kwon M, An M, Klempner SJ, Lee H, Kim K-M, Sa JK, et al. Determinants of Response and Intrinsic Resistance to PD-1 Blockade in Microsatellite Instability–High Gastric Cancer. Cancer Discov. 2021;11:2168–85.

121.    Kayhanian H, Barmpoutis P, Lakatos E, Cross W, Caravagna G, Zapata L, et al. Mutation Rate Evolution Drives Immune Escape In Mismatch Repair-Deficient Cancer [Internet]. bioRxiv; 2022 [cited 2023 Sep 27]. page 2022.03.06.482973. Available from: https://www.biorxiv.org/content/10.1101/2022.03.06.482973v1

122.    Behan FM, Iorio F, Picco G, Gonçalves E, Beaver CM, Migliardi G, et al. Prioritization of cancer therapeutic targets using CRISPR–Cas9 screens. Nature. Nature Publishing Group; 2019;568:511–6.

123.    Chan EM, Shibue T, McFarland JM, Gaeta B, Ghandi M, Dumont N, et al. WRN helicase is a synthetic lethal target in microsatellite unstable cancers. Nature. Nature Publishing Group; 2019;568:551–6.

124.    Lieb S, Blaha-Ostermann S, Kamper E, Rippka J, Schwarz C, Ehrenhöfer-Wölfer K, et al. Werner syndrome helicase is a selective vulnerability of microsatellite instability-high tumor cells. eLife. 2019;8:e43333.

125.    Kategaya L, Perumal SK, Hager JH, Belmont LD. Werner Syndrome Helicase Is Required for the Survival of Cancer Cells with Microsatellite Instability. iScience. 2019;13:488–97.

126.    Picco G, Cattaneo CM, van Vliet EJ, Crisafulli G, Rospo G, Consonni S, et al. Werner Helicase Is a Synthetic-Lethal Vulnerability in Mismatch Repair-Deficient Colorectal Cancer Refractory to Targeted Therapies, Chemotherapy, and Immunotherapy. Cancer Discov. 2021;11:1923–37.

127.    Rao Y, Srivatsan A, Liimatta M, Munoz D, Quirit J, Shi J, et al. Abstract 1628: A small-molecule inhibitor of WRN selectively kills MSI-H cancer cells and phenocopies WRN genetic defects. Cancer Res. 2023;83:1628.

128.    Overwijk WW, Restifo NP. B16 as a mouse model for human melanoma. Curr Protoc Immunol. 2001;Chapter 20:Unit 20.1.

129.    Coligan JE. Current Protocols in Immunology. J. Wiley & Sons; 1991.

130.    Hanahan D, Weinberg RA. Hallmarks of cancer: the next generation. Cell. 2011;144:646–74.

131.    Qian SS, Gao J, Wang JX, Liu Y, Dong HY. [Establishment of a mouse forestomach carcinoma cell line (MFC) with spontaneous hematogenous metastasis and preliminary study of its biological characteristics]. Zhonghua Zhong Liu Za Zhi. 1987;9:261–4.

132.    Yamamoto M, Nomura S, Hosoi A, Nagaoka K, Iino T, Yasuda T, et al. Established gastric cancer cell lines transplantable into C57BL/6 mice show fibroblast growth factor receptor 4 promotion of tumor growth. Cancer Sci. 2018;109:1480–92.

133.    Wang TC, Dangler CA, Chen D, Goldenring JR, Koh T, Raychowdhury R, et al. Synergistic interaction between hypergastrinemia and Helicobacter infection in a mouse model of gastric cancer. Gastroenterology. 2000;118:36–47.

134.    Oshima H, Matsunaga A, Fujimura T, Tsukamoto T, Taketo MM, Oshima M. Carcinogenesis in mouse stomach by simultaneous activation of the Wnt signaling and prostaglandin E2 pathway. Gastroenterology. 2006;131:1086–95.

135.    Kim H, Jeong H, Cho Y, Lee J, Nam KT, Lee H-W. Disruption of the Tff1 gene in mice using CRISPR/Cas9 promotes body weight reduction and gastric tumorigenesis. Lab Anim Res. 2018;34:257–63.

136.    Tebbutt NC, Giraud AS, Inglese M, Jenkins B, Waring P, Clay FJ, et al. Reciprocal regulation of gastrointestinal homeostasis by SHP2 and STAT-mediated trefoil gene activation in gp130 mutant mice. Nat Med. 2002;8:1089–97.

137.    Park JW, Jang SH, Park DM, Lim NJ, Deng C, Kim DY, et al. Cooperativity of E-cadherin and Smad4 loss to promote diffuse-type gastric adenocarcinoma and metastasis. Mol Cancer Res MCR. 2014;12:1088–99.

138.    Seidlitz T, Chen Y-T, Uhlemann H, Schölch S, Kochall S, Merker SR, et al. Mouse Models of Human Gastric Cancer Subtypes With Stomach-Specific CreERT2-Mediated Pathway Alterations. Gastroenterology. Elsevier; 2019;157:1599-1614.e2.

139.    Leibold J, Amor C, Tsanov KM, Ho Y-J, Sánchez-Rivera FJ, Feucht J, et al. Somatic mouse models of gastric cancer reveal genotype-specific features of metastatic disease [Internet]. bioRxiv; 2022 [cited 2023 Sep 28]. page 2022.06.15.494941. Available from: https://www.biorxiv.org/content/10.1101/2022.06.15.494941v1

140.    Mahe MM, Aihara E, Schumacher MA, Zavros Y, Montrose MH, Helmrath MA, et al. Establishment of Gastrointestinal Epithelial Organoids. Curr Protoc Mouse Biol. 2013;3:217–40.

141.    Miyoshi H, Stappenbeck TS. In vitro expansion and genetic modification of gastrointestinal stem cells in spheroid culture. Nat Protoc. 2013;8:2471–82.

142.    Gu Z. Complex heatmap visualization. iMeta. 2022;1:e43.

143.    Ferrer-Bonsoms JA, Jareno L, Rubio A. Rediscover: an R package to identify mutually exclusive mutations. Bioinforma Oxf Engl. 2022;38:844–5.

144.    Team R. A language and environment for statistical computing. Computing. 2006;1.

145.    Wickham H. ggplot2 [Internet]. Cham: Springer International Publishing; 2016 [cited 2023 Sep 28]. Available from: http://link.springer.com/10.1007/978-3-319-24277-4

146.    Woerner SM, Tosti E, Yuan YP, Kloor M, Bork P, Edelmann W, et al. Detection of coding microsatellite frameshift mutations in DNA mismatch repair-deficient mouse intestinal tumors. Mol Carcinog. 2015;54:1376–86.

147.    Durinck S, Spellman PT, Birney E, Huber W. Mapping identifiers for the integration of genomic datasets with the R/Bioconductor package biomaRt. Nat Protoc. Nature Publishing Group; 2009;4:1184–91.

148.    Robinson MD, McCarthy DJ, Smyth GK. edgeR: a Bioconductor package for differential expression analysis of digital gene expression data. Bioinforma Oxf Engl. 2010;26:139–40.

149.    Warnes G, Bolker B, Bonebakker L, Gentleman R, Liaw W, Lumley T, et al. gplots: Various R Programming Tools for Plotting Data. 2015 [cited 2023 Sep 28]. Available from: https://www.semanticscholar.org/paper/gplots%3A-Various-R-Programming-Tools-for-Plotting-Warnes-Bolker/8917b76eacbd57ff9640214c3931d7057f111834

150. Ritchie ME, Phipson B, Wu D, Hu Y, Law CW, Shi W, et al. limma powers differential expression analyses for RNA-sequencing and microarray studies. Nucleic Acids Res. 2015;43:e47.

151. Law CW, Chen Y, Shi W, Smyth GK. voom: precision weights unlock linear model analysis tools for RNA-seq read counts. Genome Biol. 2014;15:R29.

152. Slowikowski K, Schep A, Hughes S, Dang TK, Lukauskas S, Irisson J-O, et al. ggrepel: Automatically Position Non-Overlapping Text Labels with "ggplot2" [Internet]. 2023 [cited 2023 Sep 28]. Available from: https://cran.r-project.org/web/packages/ggrepel/index.html

153. Korotkevich G, Sukhov V, Budin N, Shpak B, Artyomov MN, Sergushichev A. Fast gene set enrichment analysis [Internet]. bioRxiv; 2021 [cited 2023 Sep 28]. page 060012. Available from: https://www.biorxiv.org/content/10.1101/060012v3

154. Dolgalev I. msigdbr: MSigDB Gene Sets for Multiple Organisms in a Tidy Data Format [Internet]. 2022 [cited 2023 Sep 28]. Available from: https://cran.r-project.org/web/packages/msigdbr/index.html

155. Area-Proportional Euler and Venn Diagrams with Ellipses [Internet]. [cited 2023 Oct 18]. Available from: https://jolars.github.io/eulerr/

156. Bartfeld S, Bayram T, van de Wetering M, Huch M, Begthel H, Kujala P, et al. In vitro expansion of human gastric epithelial stem cells and their responses to bacterial infection. Gastroenterology. 2015;148:126-136.e6.

157. Han S, Fink J, Jörg DJ, Lee E, Yum MK, Chatzeli L, et al. Defining the Identity and Dynamics of Adult Gastric Isthmus Stem Cells. Cell Stem Cell. 2019;25:342-356.e7.

158. Barker N, Huch M, Kujala P, van de Wetering M, Snippert HJ, van Es JH, et al. Lgr5(+ve) stem cells drive self-renewal in the stomach and build long-lived gastric units in vitro. Cell Stem Cell. 2010;6:25–36.

159. Qiao XT, Ziel JW, McKimpson W, Madison BB, Todisco A, Merchant JL, et al. Prospective identification of a multilineage progenitor in murine stomach epithelium. Gastroenterology. 2007;133:1989–98.

160. Arnold K, Sarkar A, Yram MA, Polo JM, Bronson R, Sengupta S, et al. Sox2(+) adult stem and progenitor cells are important for tissue regeneration and survival of mice. Cell Stem Cell. 2011;9:317–29.

161. Mills JC, Andersson N, Hong CV, Stappenbeck TS, Gordon JI. Molecular characterization of mouse gastric epithelial progenitor cells. Proc Natl Acad Sci U S A. 2002;99:14819–24.

162. Stange DE, Koo B-K, Huch M, Sibbel G, Basak O, Lyubimova A, et al. Differentiated Troy+ chief cells act as reserve stem cells to generate all lineages of the stomach epithelium. Cell. 2013;155:357–68.

163. Li X-B, Yang G, Zhu L, Tang Y-L, Zhang C, Ju Z, et al. Gastric Lgr5(+) stem cells are the cellular origin of invasive intestinal-type gastric cancer in mice. Cell Res. 2016;26:838–49.

164. de Maat MFG, Narita N, Benard A, Yoshimura T, Kuo C, Tollenaar RAEM, et al. Development of sporadic microsatellite instability in colorectal tumors involves hypermethylation at methylated-in-tumor loci in adenoma. Am J Pathol. 2010;177:2347–56.

165. Esteller M, Catasus L, Matias-Guiu X, Mutter GL, Prat J, Baylin SB, et al. hMLH1 promoter hypermethylation is an early event in human endometrial tumorigenesis. Am J Pathol. 1999;155:1767–72.

166. Liu P, Zhang X-Y, Shao Y, Zhang D-F. Microsatellite instability in gastric cancer and pre-cancerous lesions. World J Gastroenterol WJG. 2005;11:4904–7.

167. Sha D, Jin Z, Budczies J, Kluck K, Stenzinger A, Sinicrope FA. Tumor Mutational Burden as a Predictive Biomarker in Solid Tumors. Cancer Discov. 2020;10:1808–25.

168. Zhao H, Thienpont B, Yesilyurt BT, Moisse M, Reumers J, Coenegrachts L, et al. Mismatch repair deficiency endows tumors with a unique mutation signature and sensitivity to DNA double-strand breaks. eLife. 2014;3:e02725.

169.    Repullés J, Anglada T, Soler D, Ramírez JC, Genescà A, Terradas M. Radiation-Induced Malignant Transformation of Preneoplastic and Normal Breast Primary Epithelial Cells. Mol Cancer Res. 2019;17:937–48.

170.    Hanahan D. Hallmarks of Cancer: New Dimensions. Cancer Discov. 2022;12:31–46.

171.    Mortensen R, Nissen TN, Blauenfeldt T, Christensen JP, Andersen P, Dietrich J. Adaptive Immunity against Streptococcus pyogenes in Adults Involves Increased IFN-γ and IgG3 Responses Compared with Children. J Immunol Baltim Md 1950. 2015;195:1657–64.

172.    Ajina R, Zamalin D, Zuo A, Moussa M, Catalfamo M, Jablonski SA, et al. SpCas9-expression by tumor cells can cause T cell-dependent tumor rejection in immunocompetent mice. Oncoimmunology. 2019;8:e1577127.

173.    Westcott PMK, Muyas F, Hauck H, Smith OC, Sacks NJ, Ely ZA, et al. Mismatch repair deficiency is not sufficient to elicit tumor immunogenicity. Nat Genet. Nature Publishing Group; 2023;1–10.

174.    Germano G, Lamba S, Rospo G, Barault L, Magrì A, Maione F, et al. Inactivation of DNA repair triggers neoantigen generation and impairs tumour growth. Nature. Nature Publishing Group; 2017;552:116–20.

175.    Mandal R, Samstein RM, Lee K-W, Havel JJ, Wang H, Krishna C, et al. Genetic diversity of tumors with mismatch repair deficiency influences anti–PD-1 immunotherapy response. Science. 2019;364:485–91.

176.    Salem ME, Bodor JN, Puccini A, Xiu J, Goldberg RM, Grothey A, et al. Relationship between MLH1, PMS2, MSH2 and MSH6 gene-specific alterations and tumor mutational burden in 1057 microsatellite instability-high solid tumors. Int J Cancer. 2020;147:2948–56.

177.    Armitage P, Doll R. The age distribution of cancer and a multi-stage theory of carcinogenesis. Br J Cancer. Nature Publishing Group; 2004;91:1983–9.

178.    Puisieux A, Pommier RM, Morel A-P, Lavial F. Cellular Pliancy and the Multistep Process of Tumorigenesis. Cancer Cell. 2018;33:164–72.

179. Chen L, Zeng Y, Ren B, Wang X, Zhao F, Du J, et al. ALDOC regulated the biological function and immune infiltration of gastric cancer cells. Int J Biochem Cell Biol. 2023;158:106407.

180. Chang Y-C, Tsai H-F, Huang S-P, Chen C-L, Hsiao M, Tsai W-C. Enrichment of Aldolase C Correlates with Low Non-Mutated IDH1 Expression and Predicts a Favorable Prognosis in Glioblastomas. Cancers. 2019;11:1238.

181. De Vitis C, Battaglia AM, Pallocca M, Santamaria G, Mimmi MC, Sacco A, et al. ALDOC- and ENO2- driven glucose metabolism sustains 3D tumor spheroids growth regardless of nutrient environmental conditions: a multi-omics analysis. J Exp Clin Cancer Res. 2023;42:69.

182. Lin H-C, Ho A-S, Huang H-H, Yang B-L, Shih B-B, Lin H-C, et al. STAT3-mediated gene expression in colorectal cancer cells-derived cancer stem-like tumorspheres. Adv Dig Med. 2021;8:224–33.

183. Jaffrelot M, Farés N, Brunac AC, Laurenty AP, Danjoux M, Grand D, et al. An unusual phenotype occurs in 15% of mismatch repair-deficient tumors and is associated with non-colorectal cancers and genetic syndromes. Mod Pathol Off J U S Can Acad Pathol Inc. 2022;35:427–37.

184. Zhang L, Li L, Mao Y, Hua D. VGLL3 is a prognostic biomarker and correlated with clinical pathologic features and immune infiltrates in stomach adenocarcinoma. Sci Rep. Nature Publishing Group; 2020;10:1355.

**EGFR PROJECT**

In the frame of my PhD, I have also been actively involved in another project, nearing publication, aimed at identifying predictive biomarkers of response to the blockade of epidermal growth factor receptor (EGFR) in gastroesophageal carcinoma.

**A Composite Biomarker Identifies a Subset of Gastroesophageal Cancer Patients Responsive to EGFR Targeting.**

**Daniela Conticelli**, Marco Volante, Filippo Pietrantonio, Claudia Orrù, Martina Olivero, Russell Petty, Simona Corso, Silvia Giordano* and Cristina Migliore*.
*co-last authors

The development of EGFR-targeting drugs for gastroesophageal cancer (GEC) treatment has been hampered by negative results from phase III clinical trials testing EGFR inhibitors combined with chemotherapy in molecularly unselected patients. We have previously demonstrated that GEC patients with EGFR amplification benefit from EGFR blockade, promising a reassessment of EGFR as a therapeutic target within the context of a precise patient selection.

In the current study, results from xenotrials and *in vitro* viability assays we performed on patient-derived models from our proprietary GEC platform highlighted the existence of a subset of cases sensitive to anti-EGFR drugs and lacking EGFR genetic and quantitative alterations. Through the molecular characterization of tumours and primary cells, we identified putative predictors of response to EGFR inhibition: sensitive models displayed overexpression of EREG and AREG (two EGFR ligands), HER3 (a tyrosine kinase receptor belonging to EGFR family), and BIM (a proapoptotic protein); they also showed low levels of PTPRJ (an EGFR-targeting phosphatase).

We thus defined a predictive paradigm potentially useful in the clinical practice to discriminate

a subset of GEC patients which could benefit from EGFR targeting.

## PREVIOUS PUBLICATIONS

Annalisa Petrelli, Sabrina Rizzolio, Filippo Pietrantonio, Sara E. Bellomo, Matteo Benelli, Loris De Cecco, Dario Romagnoli, Enrico Berrino, Claudia Orrù, Salvatore Ribisi, Daniel Moya-Rull, Cristina Migliore, **Daniela Conticelli**, Irene M. Maina, Elisabetta Puliga, Violeta Serra, Benedetta Pellegrino, Alba Llop-Guevara, Antonino Musolino, Salvatore Siena, Andrea Sartore-Bianchi, Michele Prisciandaro, Federica Morano, Maria Antista, Uberto Fumagalli, Giovanni De Manzoni, Maurizio Degiuli, Gian Luca Baiocchi, Marco F. Amisano, Alessandro Ferrero, Caterina Marchio, Simona Corso and Silvia Giordano. **BRCA2 Germline Mutations Identify Gastric Cancers Responsive to PARP Inhibitors.** Cancer Res 2023;83:1699–710. DOI: 10.1158/0008-5472.CAN-22-2620.

Simona Corso, Filippo Pietrantonio, Maria Apicella, Cristina Migliore, **Daniela Conticelli**, Annalisa Petrelli, Laura D'Errico, Stefania Durando, Daniel Moya-Rull, Sara E. Bellomo, Stefano Ughetto, Maurizio Degiuli, Rossella Reddavid, Uberto Fumagalli, Stefano De Pascale, Giovanni Sgroi, Emanuele Rausa, Gian Luca Baiocchi, Sarah Molfino, Giovanni De Manzoni, Maria Bencivenga, Salvatore Siena, Andrea Sartore-Bianchi, Federica Morano, Salvatore Corallo, Michele Prisciandaro, Maria Di Bartolomeo, Annunziata Gloghini, Silvia Marsoni, Antonino Sottile, Anna Sapino, Caterina Marchiò, Asa Dahle-Smith, Zosia Miedzybrodzka, Jessica Lee, Siraj M. Ali, Jeffrey S. Ross, Brian M. Alexander, Vincent A. Miller, Russell Petty, Alexa B. Schrock and Silvia Giordano. **Optimized EGFR Blockade Strategies in EGFR Addicted Gastroesophageal Adenocarcinomas**. Clin Cancer Res. 2021 Jun 1;27(11):3126-3140 DOI: 10.1158/1078-0432.CCR-20-0121.

Simona Corso, Claudio Isella, Sara E. Bellomo, Maria Apicella, Stefania Durando, Cristina Migliore, Stefano Ughetto, Laura D'Errico, Silvia Menegon, Daniel Moya-Rull, Marilisa Cargnelutti, Tânia Capelôa, **Daniela Conticelli**, Jessica Giordano, Tiziana Venesio, Antonella Balsamo, Caterina Marchiò, Maurizio Degiuli, Rossella Reddavid, Uberto Fumagalli, Stefano De Pascale, Giovanni Sgroi, Emanuele Rausa, Gian Luca Baiocchi, Sarah Molfino, Filippo Pietrantonio, Federica Morano, Salvatore Siena, Andrea Sartore-Bianchi, Maria Bencivenga, Valentina Mengardo, Riccardo Rosati, Daniele Marrelli, Paolo Morgagni, Stefano Rausei, Giovanni Pallabazzer, Michele De Simone, Dario Ribero, Silvia Marsoni, Antonino Sottile, Enzo Medico, Paola Cassoni, Anna Sapino, Eirini Pectasides, Aaron R. Thorner, Anwesha Nag, Samantha D. Drinan, Bruce M. Wollison, Adam J. Bass and Silvia Giordano. **A**

**Comprehensive PDX Gastric Cancer Collection Captures Cancer Cell Intrinsic Transcriptional MSI Traits**. Cancer Res. 2019 Nov 15;79(22):5884-5896. DOI: 10.1158/0008-5472.CAN-19-1166.

## ACKNOWLEDGEMENTS